Additive Friction Stir Deposition of Aerospace Al-Zn-Mg-Cu-Zr Alloys: Leveraging Processing and Metallurgical Science for Structural Repair.

Greg D. Hahn

Dissertation Submitted to the faculty of the Virginia Polytechnic Institute and State University in partial fulfillment of the requirements for the degree of

Doctor in Philosophy

In

Materials Science and Engineering

Hang Z. Yu, Chair

Wenjun Cai

William T. Reynolds

Roop Mahajan

December 8, 2023

Blacksburg, VA

Keywords: Additive Friction Stir Deposition, AA7050, dispersoid, corrosion, fatigue

Additive Friction Stir Deposition of Aerospace Al-Zn-Mg-Cu-Zr Alloys: Leveraging Processing and Metallurgical Science for Structural Repair.

Greg D. Hahn

ABSTRACT

Additive Friction Stir Deposition is an emerging solid-state additive manufacturing process that leverages severe plastic deformation to deposit fully dense metallic parts. This is of particular interest for the high-strength aluminum alloys in which the addition of copper to the alloy chemistry makes them susceptible to hot-cracking. This plagues traditional 3D printing of metals which is based on melt and solidification. This work looks at a particular high-strength aluminum alloy AA7050, one of the most widely utilized alloys for complex aerostructures. One of the key traits that allow for its widespread use is its low quench sensitivity, allowing for it to be formed into thick sections and still achieve adequate strength. This work studies the feasibility of printing AA7050 and achieving full strength in thin cross sections as well as the influence of the zirconium dispersoid particle on quench sensitivity when applied to thicker sections. It was found that AA7050 after AFSD has significantly more quench sensitivity than traditionally processed material and through STEM, it was determined that this was due to the Al_3Zr dispersoid particles providing heterogeneous precipitation sites. It was demonstrated that removing the Zr alleviates the quench sensitivity in the case of printing with a featureless tool, but the breakup of constituent particles with a protrusion tool allows adequate sites to induce quench sensitivity. This work shows that AFSD of AA7050 is inherently flawed, the dynamic recrystallization necessary to deposit material is detrimental to the fundamental performance of the alloy. A separate study is shown in which AFSD was utilized to successfully repair analogous corroded fastener holes in AA7050 commonly observed in service. After repairing with AFSD, the AA7050 outperformed the baseline material in R=0.1 and R=-1 fatigue, even outperforming pristine material in the R=0.1 case. This was determined to be due to the breakup of Fe-rich constituent particles serving as fatigue crack initiation sites.

Additive Friction Stir Deposition of Aerospace Al-Zn-Mg-Cu-Zr Alloys: Leveraging Processing and Metallurgical Science for Structural Repair.

Greg D. Hahn

GENERAL AUDIENCE ABSTRACT

Additive Friction Stir Deposition (AFSD) is an emerging additive manufacturing technique that utilizes severe plastic deformation instead of melting to 3D print metals. This work focuses on one of the most prominent aluminum alloys used in aerostructures (AA7050) and its performance after printing. It was found that AA7050 is not inherently suitable for the high strain nature of AFSD and that modifying the alloy chemistry can alleviate losses in strength. The understanding of AA7050 and AFSD was utilized for a specific application, the repair of corroded fastener holes on the coupon level. It was found that repairing the simulated corroded hole improved the fatigue performance of the coupon indicating a successful means for repairing components.

DEDICATION

This work is dedicated to my grandparents, who's love and support of me has been unconditional.

ACKNOWLEDGMENTS

I would like to thank my advisor Dr. Hang Yu, associate professor of Materials Science and Engineering at Virginia Tech, for giving me the opportunity to explore my passion in Materials Science. I appreciate all the support and freedom that I was given and your ability to rein me in when I am too far down a rabbit hole.

I would like to thank my parents, Carol and David Hahn. Thank you for supporting me in whatever passion is guiding me.

I would like to thank my colleague Kendall Knight, for his ever-present friendship and willingness to debate any topic. Countless hours were spent discussing the minutiae of both our theses.

I would like to thank the current and former members of the Yu Group at Virginia Tech. Graduated members welcomed me with open arms and taught me how to function in graduate school. To the members that I leave behind, thank you for continuing to push my work forward and for all your help.

I would like to thank Dr. Beth Jaklic and Dr. Jesse Lee, for their unwavering support throughout my entire life.

I would like to thank all the coaches that mentored me throughout my youth, you all taught me the true meaning of hard work and that understanding led me to where I am.

Table of Contents

Author Attributions

Manuscript 1: ***Additive Friction Stir Deposition of AA7050 Achieving Forging-Like Tensile Properties***

Author Contributions:

Greg D. Hahn wrote the original draft and performed the relevant experiments.

Kendall P. Knight assisted in experiments.

Nikhil Gotawala assisted in microscopy.

Hang Z. Yu edited the manuscript.

Manuscript 2: ***Influence of Zirconium Dispersoid Particles on Processing and Quench Sensitivity of Additive Friction Stir Deposition High Strength Al-Zn-Mg-Cu***

Author Contributions:

Greg D. Hahn wrote the original draft, performed the experiments, and conducted analysis.

Kendall P. Knight assisted in experiments.

R. Joey Griffiths assisted in texture analysis.

Hang Z. Yu edited the manuscript.

Manuscript 3: ***Solid-State Structural Repair of Al-Zn-Mg-Cu with Corroded Thru-Hole***

Author Contributions:

Greg D. Hahn wrote the original draft, performed experiments, and performed data analysis.

Kendall P. Knight assisted in experiments and edited the manuscript.

R. Joey Griffiths assisted in initial experimentation.

David Garcia assisted in initial experiments.

Anand Karuppiah performed finite element analysis.

Nam D. Pham provided experimental guidance.

Jim Lua provided finite element support and guidance.

Hang Z. Yu edited the manuscript.

Chapter 1: Introduction

1.1 7xxx Series Aluminum Physical Metallurgy

1.1.1 Background and Introduction

Aluminum has had a role in aircraft since their earliest inception, originally used in engine components aboard the Wright brother's original airplane; the need for light components led to the decision of using wood for the airframe [1]. For the first 25 years of aviation, airframes remained mostly made of wood, but upon discovery of precipitation hardening aluminums the structural components transitioned to aluminum [1]. With the increased understanding of precipitation hardened aluminum alloys, two main alloy systems were adopted into aerostructures: the 2xxx Al-Cu alloys and the 7xxx Al-Zn-Mg alloys [1], [2]. This work will focus on the 7xxxaluminum series, specifically Al-Zn-Mg-Cu alloys. This alloy system comprises most of the structural components utilized in aerospace applications.

1.1.2 Particle Types

There are several particles present within the aluminum matrix that govern its strength, texture, corrosion resistance and fatigue properties. The first, most important type of particle is the strengthening precipitate; in the 7xxx series system this is the $MgZn_2$ η-phase. The precipitation sequence for these particles will be discussed in more detail later in this work, but the size, volume fraction, and spacing determine the yield strength of 7xxx series Al alloys. Strengthening precipitates range in size from 1-10 nm depending on the level of heat treatment. The second type of particle is the dispersoid particle, these particles typically consist of the minor alloy elements (i.e., chromium, zirconium, manganese) and typically range from 10-200 nm [1], [3]. These particles are responsible for stabilizing the grain structure, inducing texture, and are governed by their coherency with the matrix. The last type of particle is the constituent particles; these intermetallic particles consist of impurities from the melting process, typically containing Fe and Si and ranging from 1-30 μm [1]. The constituent particles often form with other alloying elements in a liquid-solid eutectic reaction upon cooling from the molten state [4], [5]. The common constituent particles in the 7xxx series family are the Al_7Cu_2Fe particle or the Mg_2Si particle.

1.1.3 Particle Coherency

When discussing particles present within a hierarchical microstructure, especially those present within a precipitation hardened regime; it is paramount to understand and discuss the role of coherency. Coherency is a function of the lattice mismatch between a particle and the surrounding matrix lattice. Low lattice mismatch allows for the matrix lattice to elastically strain and accommodate the particle up to a critical particle size [6]. A coherent interface is inherently low energy, the lattice and particle have very little strain needed to fully accommodate the particle [7]. Coherency is also a function of size and morphology; as a particle becomes larger and has more interfacial area, the matrix must shift more to accommodate it. For this reason, coherent particles will often initially form in spheres as that shape maximizes the volume relative

to surface area. Once the total interfacial area of the particle grows beyond a critical size the lattice will utilize a dislocation at the particle-matrix interface to accommodate the now plastic deformation caused by the lattice mismatch. This is considered a semi-coherent interface [7]. Lastly, an interface that has experienced a dislocation looping event or a recrystallization front moving through it can lose all its orientation with the matrix. This is considered an incoherent interface and is the highest energy interface. The interface types in terms of interfacial energy are as follows: coherent interface < semi-coherent interface < incoherent interface.

The influence of particle coherency plays several roles within aluminum physical metallurgy. While not exhaustive in terms of the role of interfacial coherency, two of the major roles that will be discussed in this work are 1. Precipitation kinetics and 2. Grain boundary pinning. The precipitation sequence of the hardening phase of 7xxx series aluminums will be discussed in greater detail, but in general the presence of many incoherent interfaces is detrimental to the strength of the material [8], [9]. Incoherent interfaces are high energy and provide a site for heterogenous nucleation of strengthening precipitates during quenching. This phenomenon creates precipitate free zones, regions with lower than anticipated solute that lack the strengthening precipitate phase. These precipitate free zones lead to lower strength in the bulk material.

Particle coherency also plays a large role in pinning grain boundaries, in the 7xxx series aluminum matrix this is often the role of the dispersoid particle [1], [10]. The effect of particles on grain boundary pinning force is generally accepted to be governed by the Zener Equation (Equation 1) [11].

$$F_s = \pi r \gamma \tag{1}$$

Where F_s is the pinning force exerted by an incoherent spherical particle, r is the radius of the particle, and γ is the interfacial energy of the boundary. This force is applied across a geometric factor related to the volume fraction and radius of the particle (Equation 2) [11]–[13].

$$N_s = \frac{3F_v}{2\pi r^2} \tag{2}$$

Where N_s is the number of particles intersecting a unit area of a boundary, F_v is the volume fraction, and r is the radius of the particle. Then the total Zener pinning pressure (P_z) is given by Equation 3.

$$P_z = N_s F_s \tag{3}$$

It has been reported that coherent particles exert twice the force of an incoherent particle [11], [14]. Essentially making F_s=2F_s for the case of a coherent particle. This means that coherent particles are much more effective for pinning grain boundaries compared to an incoherent counterpart.

1.1.4 Precipitation Sequence and Kinetics

The 7xxx series aluminum alloys are dependent on the principal of precipitation hardening, in other words, the precipitation of small particles from a state of super saturated solid solution (S.S.S.S.) [3]. This work will focus on the Al-Zn-Mg-Cu system which has a precipitation evolution that is shown below [3].

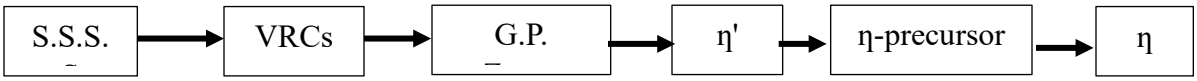

Where VRCs are "vacancy rich clusters" referring to the atomic organization of solute that can occurs near instantaneously during quenching [3], [15]. G.P refers to Guinier Preston zones, coherent layers of Zn, Mg, and Al [2], [3], [16]. G.P. Zones are broken up into G.P. I and G.P. II, where G.P. I zones form on the Al {100} and G.P. II forms on the Al {111} plane. G.P. I serve as a precipitation precursor for η' whereas G.P II transform directly into η' [3]. η' is the metastable phase of the $MgZn_2$ η-phase. It forms in a platelet morphology as a hexagonal close-packed (HCP) crystal structure with the (0001) of the HCP crystal oriented with the {111} of the Al matrix [3]. In the peak strength of the 7xxx series alloys, η' is the main precipitate responsible for peak strength in the T6 heat treatment condition, with an approximate size of 3-4 nm in thickness and 5-10 nm in width [1], [3]. η-precursor is an intermediate phase between η' and η only thought to be found in copper containing alloys [3], [15], [17], this phase will not be of significant discussion in this work. Finally, the equilibrium phase η consists of $MgZn_2$ in an HCP crystal structure, it is incoherent with the Al matrix and typically forms in a cigar shape [2], [3]. A comprehensive explanation of the precipitation sequence can be found in Chapter 2 of "Friction Stir Welding of High-Strength 7xxx Aluminum Alloys" [3]. In general, to achieve desired performance of the alloy; adequately fast quenching must be induced to lock solute in solution to be later precipitated out as strengthening precipitates. Heterogenous precipitation is when particles are formed on higher energy interfaces such as particle-matrix boundaries or grain boundaries. The reduced energy required for nucleation allows for increased kinetic rates and drives solute from the surrounding matrix onto the particle reducing the super saturation of the bulk. Any heterogenous precipitation on particles or grain boundaries has a deleterious effect on the precipitation of adequate amounts of the strengthening phase.

The addition of copper to the Al-Zn-Mg system plays a profound role in altering the precipitation kinetics of the system. It has been found to both increase the rate and extent of hardenability in the Al-Zn-Mg system. [3], [17], [18]. This rate increase is thought to be because of the relatively sluggish diffusion of copper and its interactions with dislocations and other solute causing rapid formation of VRCs [3], [15]. These VRCs serve as the locations for subsequent G.P. zones to form, and the solubility of Cu in the η' and η phase aid its transformation from G.P. zones [3]. The addition of copper also prolongs the transformation from η' to η, essentially extending the window in which peak-strength can be achieved. The addition of copper to the Al-Zn-Mg system is not without potential pitfalls, above a certain threshold excess copper can form into Al_2CuMg S-phase, a potentially harmful high temperature stable phase [3].

1.1.5 Traditional Processing of 7xxx Series Aluminum

Traditional processing of the high strength 7xxx series alloys is based upon the idea of thermomechanical processing. Typically, the creation of parts made from these alloys follows the following steps: large billets are cast then homogenized (a prolonged high temperature hold near the solutionizing temperature) to disperse solute and precipitate dispersoids; the billet is thermomechanically processed into rough shape, typically by means of forging or hot rolling. This thermomechanical step is then followed by rough machining. The rough component is heat treated (solutionize-quench-age) then undergoes final machining. After final machining, corrosion inhibiting coatings are often applied to impede surface corrosion. There are a few large advancements utilized in modern aluminum alloys to improve reliability and performance. The first advancement was improving the quality of feed stock; impurity elements such as iron and silicon are detrimental to the fatigue crack initiation as well as the corrosion behavior of the high-performance components [1], [5], [19]. Over the years the ability to reduce the concentration of impurity elements has progressed, resulting in commercially available AA7050 having impurity content more analogous to AA7150. Secondly, the homogenization of the billet plays a large role in its final performance [20]. While distributing solute, the homogenization also allows sluggish solute to precipitate out into the dispersoid particles. As mentioned previously, these dispersoid particles are often formed out of zirconium, chromium, or manganese and play the role of stabilizing the grain structure. During thermomechanical processing, the hindering of recrystallization can induce texture; this has been utilized in wrought products extensively to shape the product such that the load direction is in line with the forged direction [1]. Optimized homogenization treatments have been developed to modify the dispersoid size and spacing, allowing further anisotropy to be achieved. Finally, the advancement of heat treatments has been substantial. The use of CALPHAD style software allows for improved prediction and optimization of the final heat treatment.

1.1.6 Dispersoid Particle Fundamentals

As previously discussed, the dispersoid particles play a crucial role in the ability of thermomechanical processing to induce advantageous anisotropy in a component. It was also discussed that homogenization plays a large role in the precipitation of these particles. Dispersoid particles are a relatively niche aspect of the 7xxx series aluminum alloys, their principal alloying elements (chromium and zirconium) comprise much less than 1 wt.% of the entire alloy, but they play a crucial role in the alloy's performance. Early 7xxx series alloys utilized chromium rich dispersoids; the $Al_{18}Mg_3Cr_2$ intermetallic forms in relatively large incoherent particles lending themselves to rampant heterogenous nucleation and quench sensitivity [8], [9]. It was discovered that switching to a zirconium based dispersoid particle reduced the quench sensitivity of 7xxx series alloys, this is due to the zirconium forming a metastable L_12 Al_3Zr particle with coherent interfaces with the matrix [1], [3], [8]. The coherent interface makes it more potent in terms of grain stabilization and less prone to heterogenous nucleation upon quenching. It has been widely cited that the Al_3Zr particle retains its original orientation when confronted with a recrystallization front, meaning that it becomes an incoherent interface after recrystallization [10], [20]–[22]. For this reason, modern thermomechanical processing of Zr containing alloys focuses on avoiding recrystallization to ensure low quench sensitivity. For processes that fundamentally require recrystallization such as friction stir

welding, it has been found that the loss of particle coherency can exacerbate grain instability induced from dynamic recrystallization [23]–[25] This work will focus in part on the effect of the dispersoid particle during Additive Friction Stir Deposition.

1.2 3D Printing 7xxx Series Aluminum

There has been very limited success in the ability to 3D print high-strength aluminum alloys [26]–[29]. This is due to a phenomenon called "hot cracking" driven from the addition of copper to the alloy [3], [30]. As explained previously, copper is utilized to enhance the rate and extent of the precipitation hardening achieved in the alloy. All copper containing aluminum alloys are considered "non-weldable" due to copper segregating at the solidification front and causing porosity. This has caused traditional melt and solidification-based metal 3D printing (i.e., selective laser melting, powder bed fusion, wire arc additive manufacturing, directed energy deposition) to be unsuccessful. This has been a major setback for the additive manufacturing community and precludes these processes from being utilized in the aerostructures market. With recent advances led by the groundbreaking work by Martin et al., ceramic nanoparticles were added to AA7075 feedstock to provide heterogeneous nucleation sites in the melt pool [31]. This style of feedstock preparation has proven successful across a multitude of alloy systems, and has even seen commercialization into high-strength aluminum feedstock [29], [32]–[34]. While these advancements are promising for the ability to additively manufacture components, the melt and solidification-based processing is inherently flawed as it doesn't reflect the intended processing of these alloys. Furthermore, the high energy inputs typically observed in traditional AM processes can vaporize the more volatile alloying elements, leaving a matrix diminished of the intended strengthening phase [27], [28]. This vaporization is difficult to reliably control, leading to variable properties throughout a part. In this work a novel method of additive manufacturing is discussed which more closely mirrors the wrought processing method intended for the high-strength aluminum alloys.

1.3 Additive Friction Stir Deposition

Additive Friction Stir Deposition (AFSD) is a novel solid-state additive manufacturing technique that utilizes the friction stir principle and severe plastic deformation to deposit material [35]–[37]. AFSD uses a rotating hollow tool and feed material is forced out of the tool. The process leverages similar fundamental physics as friction stir welding (FSW). In the same vein, many of the principles developed for FSW apply to AFSD such as the pseudo-heat index [25], [38]. The process parameters of FSW (rotation rate and traverse rate) are compounded in complexity by those concerned with additive manufacturing (feed rate and layer height). Significant work has been undertaken to both understand and model the fundamental process physics [39]–[42]. Unlike melt-solidification based additive processes, AFSD has been proven effective for depositing high-strength aluminum by leveraging its fully solid state nature [40], [41], [43]–[45] as well as retaining the ability to heat treat the material back to forging-like properties [46].

During the AFSD process, material is forced out of the feed channel and experiences an incredibly high strain rate event [42]. This event causes extensive subgrain rotation of the feed material and the flow stress dictates the final subgrain size [47]. This work will work to understand whether processes such as FSW and AFSD are fundamentally incompatible with the high-strength aluminum alloys that are traditionally processed with the intent to prevent recrystallization.

1.4 Dissertation Overview

The aim of this dissertation is to shed light on the processability of AA7050, both understanding the effect of dispersoid particles as well as post-deposition heat treatment. With these understandings, an application driven use of AFSD for AA7050 is given.

Chapter 2 includes a submitted manuscript (1) that demonstrates the ability to print AA7050 via AFSD and then heat treat back to forging-like properties. This work compares the as printed to the fully heat-treated state, both in the microstructure and in the mechanical response. It was observed that the solutionizing heat treatment induced an abnormal grain growth event leaving a bimodal distribution in grain size within the deposited material.

Chapter 3 (Manuscript 2) studied the effect of tool type, and the effect of a modified AA7050 alloy on quench sensitivity. Thorough investigation utilized EBSD and HR-TEM to determine the effect of the Al_3Zr dispersoid particle on AFSD of Al-Zn-Mg-Cu alloys. It was found that removal of the minor alloying elements reduces the effect of quench sensitivity, giving rise to a possible modified alloy more suitable for high-strain processing such as AFSD.

Chapter 4 (Manuscript 3) examines the use of AFSD to repair corroded fastener holes in AA7050-T7451 rolled plate. It was found that the solid-state repair could improve the fatigue life compared to the baseline in the R=-1 loading case, and outperformed new material in the R=0.1 loading condition. The repair was divided into relevant regions and thoroughly investigated to understand the microstructural influence on the fatigue performance. Fundamental mechanisms for improving fatigue life and plans for further improvement are discussed.

Chapter 5 summarizes and draws conclusions from Chapters 2-4. Future work to understand the extent of AA7050 quench sensitivity and future alloy design is discussed.

Chapter 1 References

[1] E. A. Starke and J. T. Staley, "Application of modern aluminium alloys to aircraft," in *Fundamentals of Aluminium Metallurgy: Production, Processing and Applications*, Elsevier Ltd., 2010, pp. 747–783. doi: 10.1533/9780857090256.3.747.

[2] K. K. Sankaran and R. S. Mishra, "Aluminum Alloys," in *Metallurgy and Design of Alloys with Hierarchical Microstructures*, Elsevier, 2017, pp. 57–176. doi: 10.1016/B978-0-12-812068-2.00004-7.

[3] R. S. Mishra and M. Komarasamy, "Physical Metallurgy of 7XXX Alloys," in *Friction Stir Welding of High Strength 7XXX Aluminum Alloys*, Elsevier, 2016, pp. 5–14. doi: 10.1016/b978-0-12-809465-5.00002-7.

[4] H. Z. Yu and G. D. Hahn, "Potential and challenges for large-scale near-net-shaping of 7xxx aerospace grade aluminum via additive friction stir deposition," *Materials Letters: X*, vol. 19, Sep. 2023, doi: 10.1016/j.mlblux.2023.100217.

[5] Y. Zhu, K. Sun, and G. S. Frankel, "Intermetallic Phases in Aluminum Alloys and Their Roles in Localized Corrosion," *J Electrochem Soc*, vol. 165, no. 11, pp. C807–C820, 2018, doi: 10.1149/2.0931811jes.

[6] R. E. Smallman and A. H. W. Ngan, *Modern Physical Metallurgy*, Eighth. Elsevier, 2014.

[7] R. E. Smallman and A. H. W. Ngan, "Modern Physical Metallurgy Eighth Edition," 2014. [Online]. Available: http://elsevier.com/locate/permissions,

[8] Y. Zhang, "Quench Sensitivity of 7xxx Series Aluminium Alloys," 2014.

[9] J. K. Yoder, "Origins of Embrittlement of an Al-Zn-Mg-Cu Alloy Post Additive Friction Stir Deposition," Virginia Tech, Blacksburg, 2022.

[10] Y. Sun, X. Bai, D. Klenosky, K. Trumble, and D. Johnson, "A Study on Peripheral Grain Structure Evolution of an AA7050 Aluminum Alloy with a Laboratory-Scale Extrusion Setup," *J Mater Eng Perform*, vol. 28, no. 8, pp. 5156–5164, Aug. 2019, doi: 10.1007/s11665-019-04208-7.

[11] P. A. Manohar and F. Chandra, "Review Five Decades of the Zener Equation," 1998.

[12] F. J. Humphreys, "A UNIFIED THEORY OF RECOVERY, RECRYSTALLIZATION AND GRAIN GROWTH, BASED ON THE STABILITY AND GROWTH OF CELLULAR MICROSTRUCTURES-II. THE EFFECT OF SECOND-PHASE PARTICLES," Acta Metallurgica Inc, 1997.

[13] F. J. Humphreys and M. Hatherly, "RECRYSTALLIZATION AND RELATED ANNEALING PHENOMENA," 2004. [Online]. Available: http://www.elsevier.com

[14] F. J. Humphreys and M. Hatherly, *Recrystallization and Related Annealing Phenomena*, 2nd ed. Oxford: Elsevier, 2004.

[15] A. Deschamps, Y. Bréchet, and F. Livet, “Influence of copper addition on precipitation kinetics and hardening in Al-Zn-Mg alloy,” *Materials Science and Technology*, vol. 15, no. 9, pp. 993–1000, 1999, doi: 10.1179/026708399101506832.

[16] G. W. Zheng, H. Li, C. Lei, J. Fu, T. J. Bian, and J. C. Yang, “Natural aging behaviors and mechanisms of 7050 and 5A90 Al alloys: A comparative study,” *Materials Science and Engineering: A*, vol. 718, pp. 157–164, Mar. 2018, doi: 10.1016/j.msea.2018.01.119.

[17] J. Z. Liu *et al.*, “Revisiting the precipitation sequence in Al-Zn-Mg-based alloys by high-resolution transmission electron microscopy,” *Scr Mater*, vol. 63, no. 11, pp. 1061–1064, Nov. 2010, doi: 10.1016/j.scriptamat.2010.08.001.

[18] A. Dupasquier, R. Ferragut, M. M. Iglesias, and F. Quasso, “Vacancy-solute association in coherent nanostructures formed in a commercial Al-Zn-Mg-Cu alloy,” in *Physica Status Solidi (C) Current Topics in Solid State Physics*, 2007, pp. 3526–3529. doi: 10.1002/pssc.200675772.

[19] C. Vargel, *Corrosion of Aluminum*. Elsevier, 2004.

[20] B. L. Ou, J. G. Yang, and M. Y. Wei, “Effect of homogenization and aging treatment on mechanical properties and stress-corrosion cracking of 7050 alloys,” *Metall Mater Trans A Phys Metall Mater Sci*, vol. 38, no. 8, pp. 1760–1773, Aug. 2007, doi: 10.1007/s11661-007-9200-z.

[21] H. E. Hu, L. Zhen, B. Y. Zhang, L. Yang, and J. Z. Chen, “Microstructure characterization of 7050 aluminum alloy during dynamic recrystallization and dynamic recovery,” *Mater Charact*, vol. 59, no. 9, pp. 1185–1189, Sep. 2008, doi: 10.1016/j.matchar.2007.09.010.

[22] M. Schöbel, P. Pongratz, and H. P. Degischer, “Coherency loss of Al 3(Sc,Zr) precipitates by deformation of an Al-Zn-Mg alloy,” *Acta Mater*, vol. 60, no. 10, pp. 4247–4254, Jun. 2012, doi: 10.1016/j.actamat.2012.04.011.

[23] M. B. Lezaack and A. Simar, “Avoiding abnormal grain growth in thick 7XXX aluminium alloy friction stir welds during T6 post heat treatments,” *Materials Science and Engineering A*, vol. 807, Mar. 2021, doi: 10.1016/j.msea.2021.140901.

[24] K. A. A. Hassan, A. F. Norman, D. A. Price, and P. B. Prangnell, “Stability of nugget zone grain structures in high strength Al-alloy friction stir welds during solution treatment,” *Acta Mater*, vol. 51, no. 7, pp. 1923–1936, Apr. 2003, doi: 10.1016/S1359-6454(02)00598-0.

[25] I. Charit and R. S. Mishra, “Abnormal grain growth in friction stir processed alloys,” *Scr Mater*, vol. 58, no. 5, pp. 367–371, Mar. 2008, doi: 10.1016/j.scriptamat.2007.09.052.

[26] N. T. Aboulkhair, M. Simonelli, L. Parry, I. Ashcroft, C. Tuck, and R. Hague, “3D printing of Aluminium alloys: Additive Manufacturing of Aluminium alloys using selective laser melting,” *Progress in Materials Science*, vol. 106. Elsevier Ltd, Dec. 01, 2019. doi: 10.1016/j.pmatsci.2019.100578.

[27] S. C. Altıparmak, V. A. Yardley, Z. Shi, and J. Lin, “Challenges in additive manufacturing of high-strength aluminium alloys and current developments in hybrid additive manufacturing,”

International Journal of Lightweight Materials and Manufacture, vol. 4, no. 2. KeAi Publishing Communications Ltd., pp. 246–261, Jun. 01, 2021. doi: 10.1016/j.ijlmm.2020.12.004.

[28] T. D. Ngo, A. Kashani, G. Imbalzano, K. T. Q. Nguyen, and D. Hui, "Additive manufacturing (3D printing): A review of materials, methods, applications and challenges," *Composites Part B: Engineering*, vol. 143. Elsevier Ltd, pp. 172–196, Jun. 15, 2018. doi: 10.1016/j.compositesb.2018.02.012.

[29] A. Wang, H. Wang, Y. Wu, and H. Wang, "3D printing of aluminum alloys using laser powder deposition: a review", doi: 10.1007/s00170-021-07440-5/Published.

[30] R. S. Mishra and H. Sidhar, "Physical Metallurgy of 2XXX Aluminum Alloys," in *Friction Stir Welding of 2XXX Aluminum Alloys Including Al-Li Alloys*, Elsevier, 2017, pp. 15–36. doi: 10.1016/b978-0-12-805368-3.00002-9.

[31] J. H. Martin, B. D. Yahata, J. M. Hundley, J. A. Mayer, T. A. Schaedler, and T. M. Pollock, "3D printing of high-strength aluminium alloys," *Nature*, vol. 549, no. 7672, pp. 365–369, Sep. 2017, doi: 10.1038/nature23894.

[32] L. Zhou *et al.*, "Microstructure and tensile property of a novel AlZnMgScZr alloy additively manufactured by gas atomization and laser powder bed fusion," *Scr Mater*, vol. 158, pp. 24–28, Jan. 2019, doi: 10.1016/j.scriptamat.2018.08.025.

[33] M. Sokoluk, C. Cao, S. Pan, and X. Li, "Nanoparticle-enabled phase control for arc welding of unweldable aluminum alloy 7075," *Nat Commun*, vol. 10, no. 1, Dec. 2019, doi: 10.1038/s41467-018-07989-y.

[34] "A7050-RAM2 A7050-RAM2 (High-Strength and Corrosion Resistant)." Erie, 2021. Accessed: Aug. 30, 2023. [Online]. Available: https://www.elementum3d.com/wp-content/uploads/2021/11/A7050-RAM2-Data-Sheets-2021-04-15.pdf

[35] H. Z. Yu *et al.*, "Non-beam-based metal additive manufacturing enabled by additive friction stir deposition," *Scr Mater*, vol. 153, pp. 122–130, Aug. 2018, doi: 10.1016/j.scriptamat.2018.03.025.

[36] H. Z. Yu, "Introduction," in *Additive Friction Stir Deposition*, Elsevier, 2022, pp. 1–19. doi: 10.1016/B978-0-12-824374-9.00004-6.

[37] H. Z. Yu and R. S. Mishra, "Additive friction stir deposition: a deformation processing route to metal additive manufacturing," *Mater Res Lett*, vol. 9, no. 2, pp. 71–83, Feb. 2021, doi: 10.1080/21663831.2020.1847211.

[38] D. Garcia *et al.*, "In situ investigation into temperature evolution and heat generation during additive friction stir deposition: A comparative study of Cu and Al-Mg-Si," *Addit Manuf*, vol. 34, Aug. 2020, doi: 10.1016/j.addma.2020.101386.

[39] N. Gotawala and H. Z. Yu, "Material flow path and extreme thermomechanical processing history during additive friction stir deposition," *J Manuf Process*, vol. 101, pp. 114–127, Sep. 2023, doi: 10.1016/J.JMAPRO.2023.05.095.

[40] C. J. T. Mason *et al.*, “Process-structure-property relations for as-deposited solid-state additively manufactured high-strength aluminum alloy,” *Addit Manuf*, vol. 40, Apr. 2021, doi: 10.1016/j.addma.2021.101879.

[41] D. Z. Avery *et al.*, “Influence of Grain Refinement and Microstructure on Fatigue Behavior for Solid-State Additively Manufactured Al-Zn-Mg-Cu Alloy,” *Metall Mater Trans A Phys Metall Mater Sci*, vol. 51, no. 6, pp. 2778–2795, Jun. 2020, doi: 10.1007/s11661-020-05746-9.

[42] M. E. J. Perry *et al.*, “Tracing plastic deformation path and concurrent grain refinement during additive friction stir deposition,” *Materialia (Oxf)*, vol. 18, Aug. 2021, doi: 10.1016/j.mtla.2021.101159.

[43] M. C. Wells, “Mechanical and Physical Properties of Additive Friction Stir Deposited Aluminum,” Virginia Tech, Blacksburg, 2022.

[44] G. G. Stubblefield *et al.*, “Ballistic Evaluation of Aluminum Alloy (AA) 7075 Plate Repaired by Additive Friction Stir Deposition Using AA7075 Feedstock,” *Journal of Dynamic Behavior of Materials*, vol. 9, no. 1, pp. 79–89, Mar. 2023, doi: 10.1007/s40870-022-00363-6.

[45] D. Z. Avery *et al.*, “Evaluation of Microstructure and Mechanical Properties of Al-Zn-Mg-Cu Alloy Repaired via Additive Friction Stir Deposition,” *J Eng Mater Technol*, vol. 144, no. 3, Jul. 2022, doi: 10.1115/1.4052816.

[46] J. K. Yoder, R. J. Griffiths, and H. Z. Yu, “Deformation-based additive manufacturing of 7075 aluminum with wrought-like mechanical properties,” *Mater Des*, vol. 198, Jan. 2021, doi: 10.1016/j.matdes.2020.109288.

[47] R. J. Griffiths *et al.*, “Solid-state additive manufacturing of aluminum and copper using additive friction stir deposition: Process-microstructure linkages,” *Materialia (Oxf)*, vol. 15, Mar. 2021, doi: 10.1016/j.mtla.2020.100967.

Chapter 2: Heat Treating Deposited AA7050

2.1 Manuscript 1: Additive Friction Stir Deposition of AA7050 Achieving Forging-Like Tensile Properties

Greg D. Hahn[1], Kendall P. Knight[1], Nikhil Gotawala[1], Hang Z. Yu[1,*]

[1] Department of Materials Science and Engineering, Virginia Tech, Blacksburg, VA 24061, USA.

[*] Corresponding Author: hangyu@vt.edu

Abstract

Owing to hot cracking, printing aerospace grade AA7050 is challenging via fusion-based additive manufacturing. Using a deformation-based additive process, here we show that forging-like tensile properties are achieved in additively manufactured AA7050 without chemical modification for the first time — YS: 430 MPa; UTS: 491 MPa; elongation: 11.2% (T74 temper).

Keywords

Additive manufacturing; additive friction stir deposition; aerospace aluminum; AA7050; forging-like properties; abnormal grain growth.

Introduction

Additive manufacturing has experienced significant growth over the last decade and is now widely exploited for rapidly prototyping components and creating complex geometries unavailable

through traditional manufacturing methods [1]. Despite its rapid growth, a sub-field within additive manufacturing has been largely left behind – structural aerospace and space components – especially those made of high-strength, precipitation-hardened 7xxx and 2xxx Al alloys [2]–[4]. AA7050, an Al-Zn-Mg-Cu alloy, represents a modern example in this category, with improved fracture toughness, corrosion resistance, and quench sensitivity from its predecessor AA7075 [5]–[7]. Traditional manufacturing of AA7050 is based on wrought processing routes like rolling, extrusion, and forging; the resulting components play a crucial role in aerostructures requiring significant load-bearing capabilities. For instance, forged AA7050 (with T74 temper) is commonly used to manufacture aircraft fuselages and wing frames [5].

AA7050 is known as a "non-weldable" alloy and undergoes hot cracking during rapid solidification in mainstream beam-based metal additive manufacturing, such as selective laser melting and wire arc additive manufacturing [3], [4], [8]–[10]. Innovative strategies, such as introducing high melting temperature nanoparticles, have been taken to induce heterogeneous nucleation inside the molten pool [4], [9], [11]. This can avoid columnar grain formation and lead to desired tensile properties after proper aging. For example, by adding 2% ceramics into the feedstock, Elementum 3D has developed a proprietary composition for beam-based additive manufacturing of AA7050, which can achieve an ultimate tensile strength (UTS) of 504 MPa and a yield strength (YS) of 469 MPa with an elongation of 6 $\pm$1.5% after hot isostatic pressing and T74 temper [12].

Modifying the alloy composition for processing viability fundamentally leads to a different alloy than the well-established AA7050, which is designed for excellent performance along with low quench sensitivity. This alteration results in possible unforeseen consequences. Moreover, the high energy input during beam-based additive manufacturing can vaporize elements like Zn and Mg, leading to the loss of strengthening precipitates necessary for post-deposition aging [8]. Vaporization is challenging to control consistently, potentially causing property uncertainties in large-scale components. We argue the need for an additive manufacturing approach for printing AA7050 that mirrors traditional wrought processing methods [13], [14]. Such an approach will allow us to leverage the intended processing path to achieve superior mechanical performance in the printed AA7050. Here, we show that additive friction stir deposition (AFSD) [15], [16] , a deformation-based additive process [17]–[19], can render fully-dense AA7050 in the as-printed state [17], [20]; after T74 temper, the printed AA7050 exhibits forging-like tensile properties with

a measured YS of 430 MPa, UTS of 491 MPa, and elongation of 11.2%. For the first time, this work shows that forging-like tensile properties can be achieved in additively manufactured AA7050.

Materials and Methods

AFSD was carried out using a MELD R2 system (MELD Manufacturing, USA). 6.35 mm thick rolled AA7050-T7451 plates were used for substrates. Feed material was cut along the rolling direction from 9.5 mm thick AA7050-T7451 rolled plate to give a 9.5 mm × 9.5 mm × 152.4 mm rod. Graphite lubricant was applied to the feed-rod surface to avoid jamming during deposition. The deposition process had two stages: (i) initially, the print head was spun at 350 RPM with a feeding rate of 0.21 mm/s; (ii) after the material is fully plasticized, steady-state deposition began at a 1.27 mm/s traverse rate and a 1.27 mm/s feeding rate. Single wall tracks were built 140 mm long, 30 mm wide, and four layers tall, giving a final build height of approximately 11 mm. ASTM E8 subsize tensile specimens [21] were fabricated along the longitudinal direction. Heat treatment was applied to the as-printed AA7050 in accordance with ASM Handbook for T74 temper: solutionizing at 475 °C for 1 hour, quenched in water, followed by a two-stage aging treatment — 107 °C for 6 hours, and then 177 °C for 6 hours. For comparison, the same heat treatment procedure was also applied to the feed material.

Tensile testing was conducted on an Instron 4468 machine at a strain rate of 10^{-3}/s; engineering strain was measured using an extensometer. Vickers microhardness testing was conducted on a Struers Duramin-40 (Cleveland, USA) automatic hardness tester with a 100-gram load and 10 second dwell time. Microstructural specimens, measuring 6.35 mm × 12.7 mm, were cut parallel to the printing direction, followed by mechanical polishing using 1000 grit sandpaper. Electropolishing was carried out with a liquid nitrogen-cooled electrolyte (70% methanol and 30% nitric acid) at 30 V for ten-second intervals. Optical microscopy was conducted using a Keyence VHX-7000 microscope (Osaka, Japan). Electron backscatter diffraction (EBSD) analysis was performed using a Zeiss LEO 1550 field-emission SEM (Wetzlar, Germany) equipped with an Oxford Nordlys detector. Transmission electron microscopy (TEM) characterization was performed on a FEI Titan (Waltham, USA).

Results and Discussion

Figure 1 shows a schematic of AFSD with inverse pole figure (IPF) maps comparing the feed material and the as-printed AA7050 wall (top layer). The rolled feed material consists of elongated

grains. The effect of dynamic recrystallization during AFSD is apparent: a more equiaxed grain structure with fine subgrain networks is seen in the as-printed AA7050. The area-averaged grain size in the top layer is 12.2 µm; this larger than typical grain size is due to the use of a featureless tool, which results in less severe plastic flow behavior than a tool with protrusions. Likewise, the as-printed material shows incomplete dynamic recrystallization and a substantial presence of low angle grain boundaries.

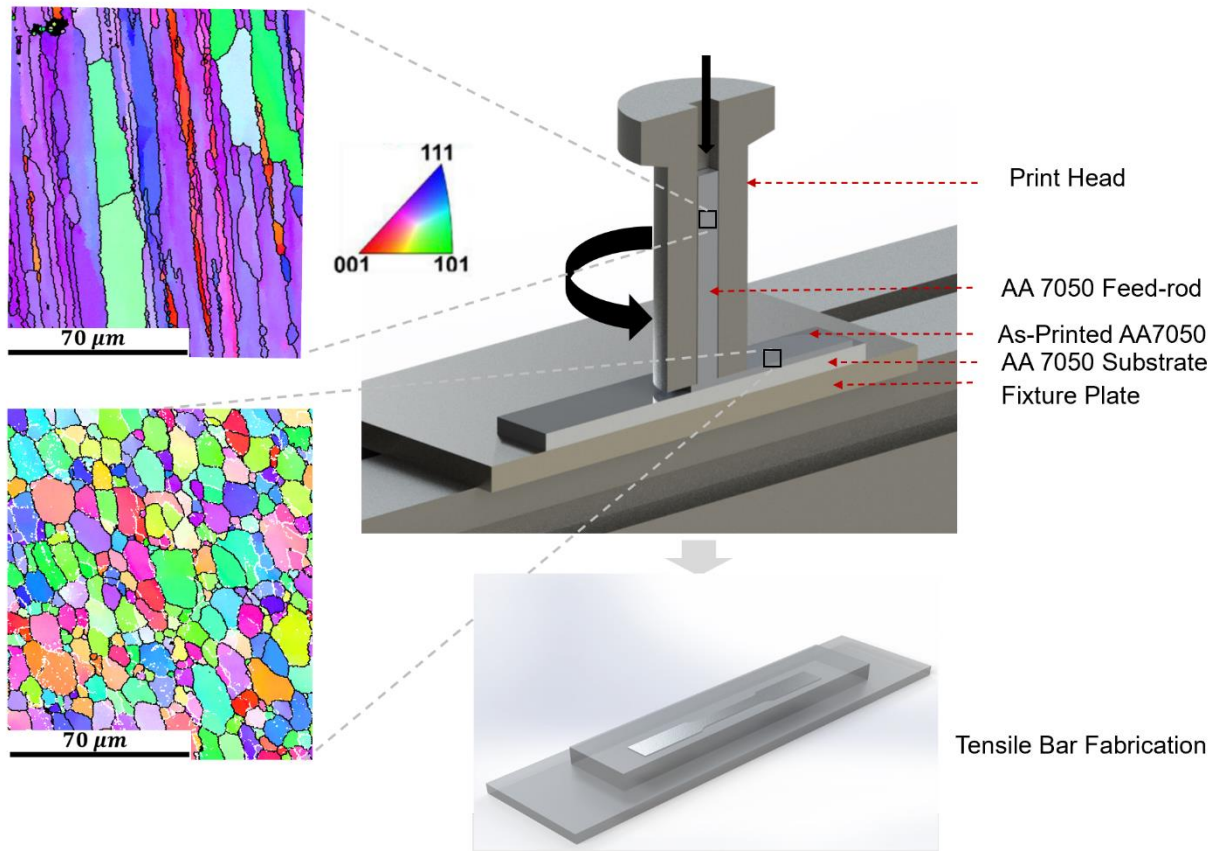

Manuscript 1 Figure 1. Schematic of the AFSD process showing elongated grain structure in the feed-rod and equiaxed grains in the as-printed AA7050.

The grain structure in the as-printed AA7050 wall is non-uniform along the build direction; finer grains are seen near the layer interfaces (denoted by arrows in Figure 2). Figure 2A illustrates this phenomenon in the interfacial region between the second and third layer, where the average grain size measures 4.2 µm. This is significantly smaller than those found in the top of the as-printed wall in Figure 1. The grain average misorientation (GAM) map in Figure 2B suggests more complete dynamic recrystallization with less intragranular misorientation at the layer-to-layer interface. This microstructure variation likely originates from the mixing and shear localization

between the bottom of the newly deposited layer and the top of the previous layer, accumulating more plastic strain at the interface. Finer grains at layer interfaces have also been observed in other AFSD studies using flat tools [22].

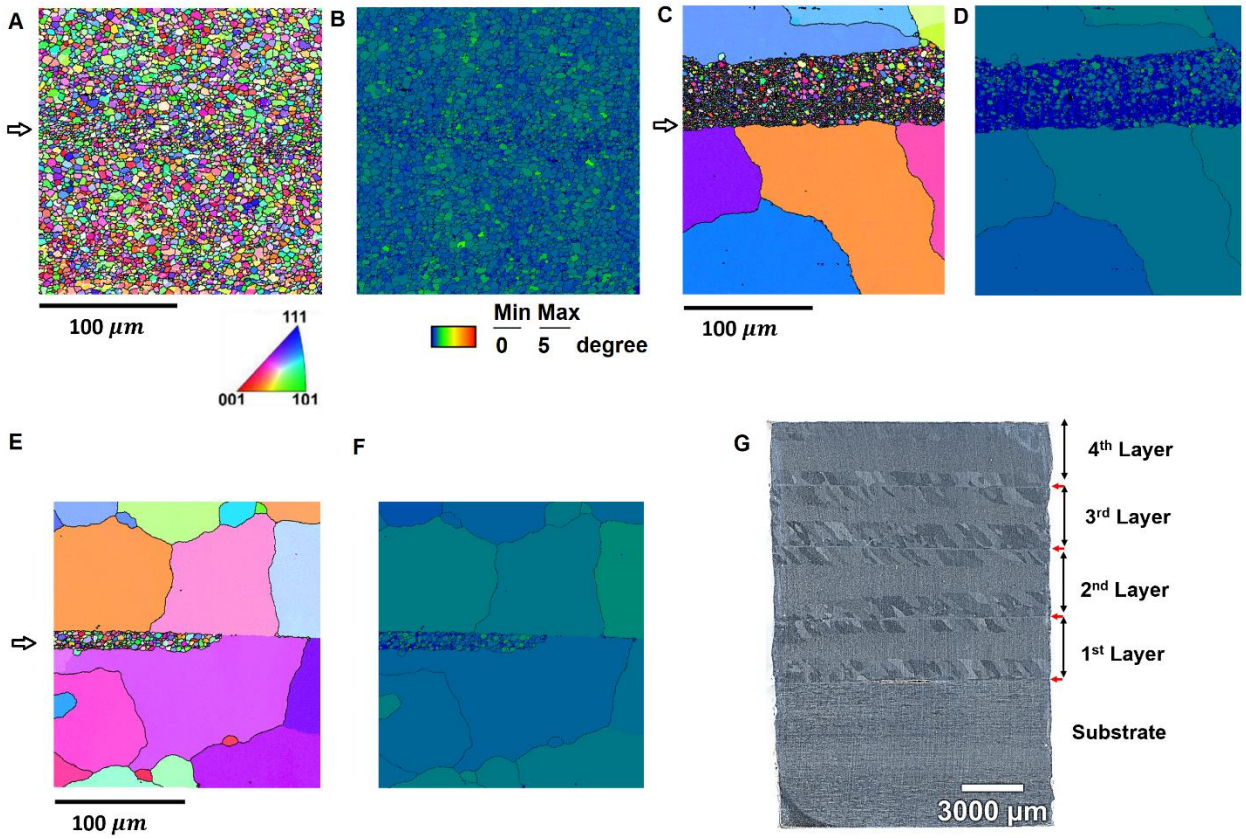

Manuscript 1 Figure 2. Microstructure of the printed AA7050. (A) IPF and (B) GAM of the 2nd-3rd interfacial region. (C) IPF and (D) GAM of the region after solution treatment. (E) IPF and (F) GAM of the region after T74 temper. (G) Stitched optical image of the entire build after heat treatment.

After solution treatment and quenching, a representative grain structure of these interfacial regions is presented in Figure 2C, showing some retained fine grains between abnormally large grains of several hundred microns in size. After aging, a similar grain structure is found in the interfacial region but with less fine grains (Figure 2E). In contrast, the grain structure does not change in the top layer during solution treatment or aging. Figure 2G shows a stitched optical image illustrating a cross-section of a four-layer build wall after undergoing heat treatment, which shows four bands with abnormally large grains: the bottom of 1st layer, 1st-2nd layer interface, 2nd-3rd layer interface, and 3rd-4th layer interface. This observation suggests that during heat treatment, abnormal grain growth (AGG) occurs in the regions adjacent to the interfaces between layers. The

GAM maps in Figures 2D and 2F show that the abnormally large grains are associated with low intragranular misorientations. This is expected because of the migration of high-angle grain boundaries.

Heat treatment-induced AGG has been reported in 7xxx Al alloys after friction stir welding or processing as well as in AFSD-printed AA6061 [7], [23], [24]. As suggested by Charit and Mishra, the AGG observed in friction stir-related processes is mostly likely due to deformation and microstructural heterogeneity [25]. In this work, the shear localization in interfacial regions creates finer grains via dynamic recrystallization, possibly impacting grain growth by size distribution and reducing local pinning forces by promoting incoherent interfaces between dispersoid particles (Al_3Zr) and matrix. Since there is no strong texture in the as-printed AA7050, anisotropy of grain boundary mobility is unlikely to be the main AGG factor. Unraveling the exact origins and mechanisms of AGG, however, will require in-depth investigations in future work.

The tensile testing results are presented in Figure 3A for the printed AA7050 followed by T74 aging, the received rolled AA7050 plate followed by T74 aging (measured along the rolling direction), and the as-printed AA7050. The printed/aged AA7050 and the received/aged AA7050 plate perform similarly with a YS of 430 MPa and 437 MPa, a UTS of 491 MPa and 496 MPa, and an elongation of 11.2% and 11.7%, respectively. We note that these two samples consist of drastically different grain structures: one results from dynamic recrystallization followed by AGG, and the other is elongated along the rolling direction. The similar mechanical behavior suggests that precipitate characteristics dominate the mechanical behavior of AA7050. AGG seems to have minimal impact on the in-plane tension properties but may prove detrimental to out-of-plane properties reliant on grain boundary area such as corrosion, crack initiation, and propagation. To compare, the as-printed AA7050 shows substantially lower YS and UTS values (180 MPa and 330 MPa, respectively). Figure 3B illustrates the Vickers hardness trends with build wall height for as-printed AA7050 and heat-treated samples. The as-printed material exhibits increasing hardness due to thermal exposures in subsequent layer deposition. The two heat-treated samples show consistent hardness values; the solution-treated material has only slightly lower hardness than the T74 aged version, thanks to the natural aging effects in AA7050 [26].

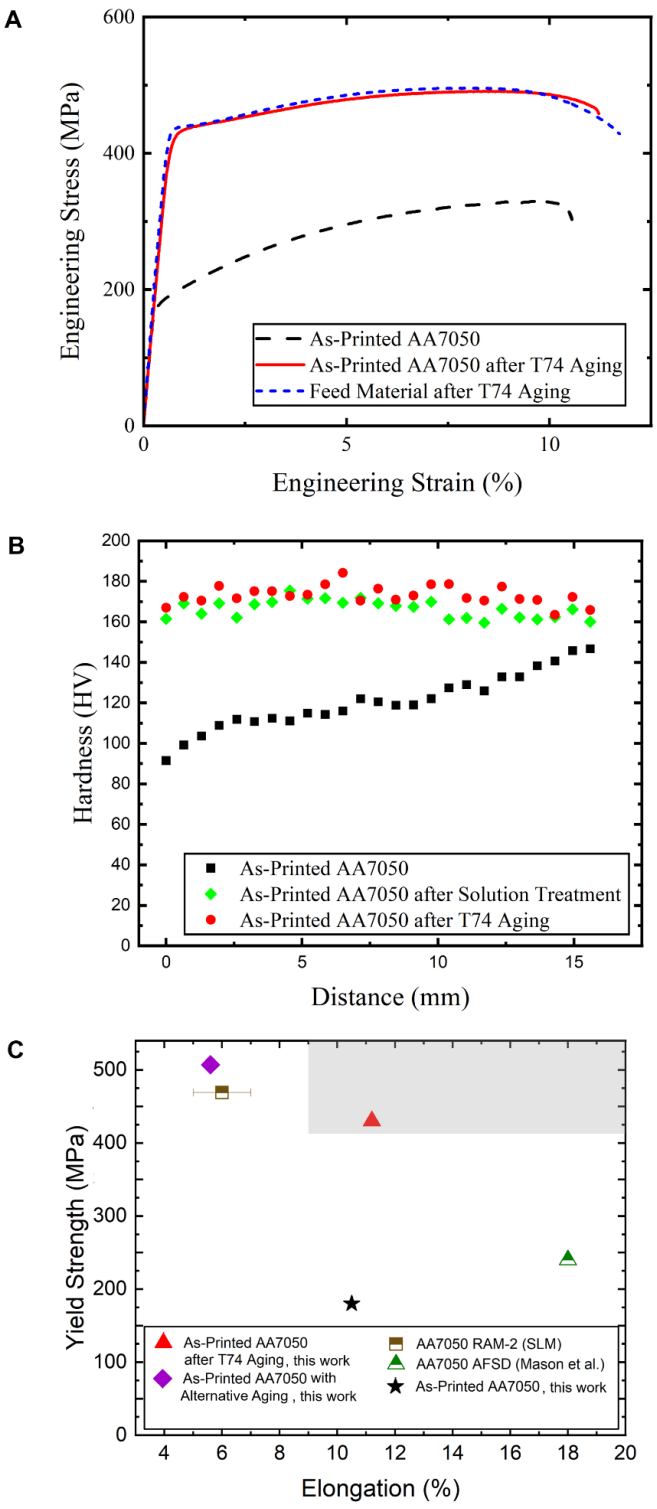

Manuscript 1 Figure 3. Mechanical testing results. (A). Tensile response of as-printed AA7050, printed and heat treated AA7050, and as-received and heat treated AA7050. (B). Vickers microhardness response of printed AA7050 in various states of thermal treatment.

(C). Ashby-style plot of yield strength and elongation at failure, with top right shaded region corresponding to the minimum forging standard according to AMS 4333.

Figure 3C displays an Ashby-style plot comparing the yield strength to elongation at failure for AA7050 produced via additive manufacturing. This includes AA7050 manufactured using selective laser melting with added nanoparticles (AA7050 RAM-2, [12]), as-printed AA7050 through AFSD reported by Mason et al [27], the as-printed AA7050 from our study, and AFSD-printed AA7050 subjected to T74 aging in our study. An alternative aging procedure commonly employed for sheets and plates (two-step aging: an initial 6-hour aging step at 107°C, followed by a subsequent 24-hour aging step at 163°C) has been found to result in higher strength but lower ductility — YS: 507 MPa; UTS: 544 MPa; elongation: 5.6%. We have included the corresponding data point in Figure 3C for reference. The shaded box in the top-right corner corresponds to the minimum forging standard set by AMS 4333 B-basis for die forgings [28]. To the best of our knowledge, this work represents the first reported instance of additively manufactured AA7050 meeting these specifications.

The precipitate attributes are compared in Figure 4 between the as-printed AA7050 and the printed AA7050 followed by T74 temper in this work. In the as-printed AA7050, there are clear groups of overgrown strengthening precipitates (Figures 4A and 4B), evidently visible to be on the order of 100 nm in size. This is an order of magnitude larger than the ~10 nm precipitates commonly found in the T74 condition [6]. From the dark field image (Figure 4B), we conclude that the precipitates are oriented along different planes, which is common for the η-phase in the overaged condition [6]. In the printed AA7050 followed by aging, fine η precipitates are densely dispersed within the grain interior, while there is also evidence of grain boundary precipitation (Figures 4C and 4D). This precipitate characteristic is expected from a T74 temper and is the main reason for the significantly enhanced YS value from the as-printed AA7050 (430 MPa vs. 180 MPa in Figure 3A).

Interestingly, in the as-printed AA7050, complex dislocation networks are seen in the grain interior with evidence of dislocation-precipitate interactions. This suggests a competition between dynamic recovery and precipitation on dislocation walls. With rapid deformation during AFSD, dislocations are created, accumulated, annihilated, and reorganized to form substructures. At the same time, precipitates may form on the dislocation walls via heterogeneous nucleation. These precipitates may grow above a critical size to effectively pin the dislocation wall; during cooling,

they can further grow to the final size via diffusion in the absence of deformation. This could be one origin of the dislocation-precipitate interactions seen in Figure 4A.

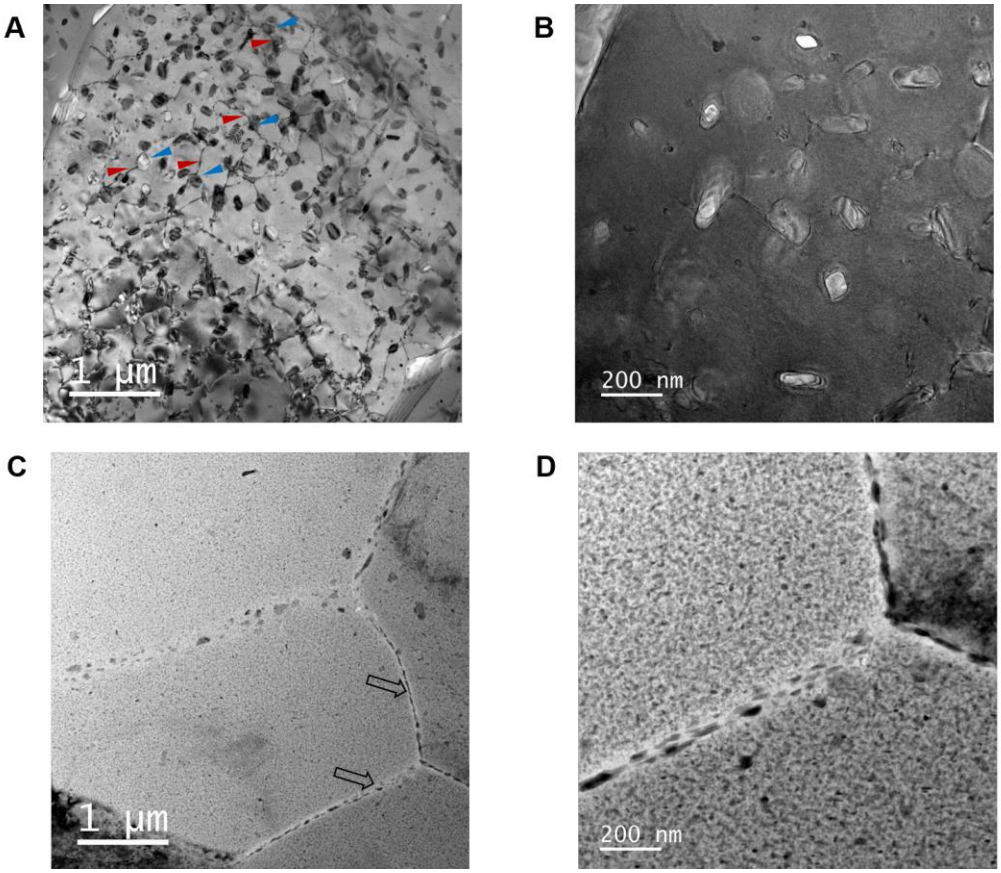

Manuscript 1 Figure 4. TEM micrographs for comparison. Low magnification bright-field images of (A) as-printed AA7050 and (C) printed AA7050 followed by T74 temper. Higher magnification images of (B) as-printed AA7050 in dark field and (D) printed AA7050 followed by T74 temper. Examples showing interactions between precipitates and dislocation walls are highlighted by leftwards and rightwards filled arrows in (A). Grain boundary precipitates are highlighted by open arrows in (C).

Conclusions

In summary, we report forging-like tensile properties (YS: 430 MPa; UTS: 491 MPa; elongation: 11.2%) in AA7050 printed by AFSD. This marks the first demonstration for additively manufactured AA7050. The printed AA7050, initially weak due to overgrown precipitates, gains strength with T74 temper. Heat treatment also induces AGG near layer interfaces, which seems to have minimal effect on the in-plane tensile properties. However, future work should strive to understand its origin and mitigate its development.

Acknowledgement

HZY acknowledges the support by DARPA through the Young Faculty Award Program (Grant number: D22AP00152). The authors would like to thank Dr. Helge Heinrich for the help with TEM imaging and helpful discussions.

Data Availability

The raw/processed data required to reproduce these findings cannot be shared at this time as the data also forms part of an ongoing study.

Manuscript 1 References

[1] T. D. Ngo, A. Kashani, G. Imbalzano, K. T. Q. Nguyen, and D. Hui, "Additive manufacturing (3D printing): A review of materials, methods, applications and challenges," *Composites Part B: Engineering*, vol. 143. Elsevier Ltd, pp. 172–196, Jun. 15, 2018. doi: 10.1016/j.compositesb.2018.02.012.

[2] S. C. Altıparmak, V. A. Yardley, Z. Shi, and J. Lin, "Challenges in additive manufacturing of high-strength aluminium alloys and current developments in hybrid additive manufacturing," *International Journal of Lightweight Materials and Manufacture*, vol. 4, no. 2. KeAi Publishing Communications Ltd., pp. 246–261, Jun. 01, 2021. doi: 10.1016/j.ijlmm.2020.12.004.

[3] N. T. Aboulkhair, M. Simonelli, L. Parry, I. Ashcroft, C. Tuck, and R. Hague, "3D printing of Aluminium alloys: Additive Manufacturing of Aluminium alloys using selective laser melting," *Progress in Materials Science*, vol. 106. Elsevier Ltd, Dec. 01, 2019. doi: 10.1016/j.pmatsci.2019.100578.

[4] J. H. Martin, B. D. Yahata, J. M. Hundley, J. A. Mayer, T. A. Schaedler, and T. M. Pollock, "3D printing of high-strength aluminium alloys," *Nature*, vol. 549, no. 7672, pp. 365–369, Sep. 2017, doi: 10.1038/nature23894.

[5] E. A. Starke and J. T. Staley, "Application of modern aluminium alloys to aircraft," in *Fundamentals of Aluminium Metallurgy: Production, Processing and Applications*, Elsevier Ltd., 2010, pp. 747–783. doi: 10.1533/9780857090256.3.747.

[6] R. S. Mishra and M. Komarasamy, *Physical Metallurgy of 7XXX Alloys*. Elsevier, 2016. doi: 10.1016/b978-0-12-809465-5.00002-7.

[7] H. E. Hu, L. Zhen, B. Y. Zhang, L. Yang, and J. Z. Chen, "Microstructure characterization of 7050 aluminum alloy during dynamic recrystallization and dynamic recovery," *Mater Charact*, vol. 59, no. 9, pp. 1185–1189, Sep. 2008, doi: 10.1016/j.matchar.2007.09.010.

[8] T. Qi, H. Zhu, H. Zhang, J. Yin, L. Ke, and X. Zeng, "Selective laser melting of Al7050 powder: Melting mode transition and comparison of the characteristics between the keyhole and conduction mode," *Mater Des*, vol. 135, pp. 257–266, Dec. 2017, doi: 10.1016/j.matdes.2017.09.014.

[9] M. Sokoluk, C. Cao, S. Pan, and X. Li, "Nanoparticle-enabled phase control for arc welding of unweldable aluminum alloy 7075," *Nat Commun*, vol. 10, no. 1, Dec. 2019, doi: 10.1038/s41467-018-07989-y.

[10] A. Wang, H. Wang, Y. Wu, and H. Wang, "3D printing of aluminum alloys using laser powder deposition: a review", doi: 10.1007/s00170-021-07440-5/Published.

[11] L. Zhou *et al.*, "Microstructure and tensile property of a novel AlZnMgScZr alloy additively manufactured by gas atomization and laser powder bed fusion," *Scr Mater*, vol. 158, pp. 24–28, Jan. 2019, doi: 10.1016/j.scriptamat.2018.08.025.

[12] “A7050-RAM2 A7050-RAM2 (High-Strength and Corrosion Resistant).” Erie, 2021. Accessed: Aug. 30, 2023. [Online]. Available: https://www.elementum3d.com/wp-content/uploads/2021/11/A7050-RAM2-Data-Sheets-2021-04-15.pdf

[13] H. Z. Yu and G. D. Hahn, “Potential and challenges for large-scale near-net-shaping of 7xxx aerospace grade aluminum via additive friction stir deposition,” *Materials Letters: X*, vol. 19, Sep. 2023, doi: 10.1016/j.mlblux.2023.100217.

[14] J. K. Yoder, R. J. Griffiths, and H. Z. Yu, “Deformation-based additive manufacturing of 7075 aluminum with wrought-like mechanical properties,” *Mater Des*, vol. 198, Jan. 2021, doi: 10.1016/j.matdes.2020.109288.

[15] H. Z. Yu and R. S. Mishra, “Additive friction stir deposition: a deformation processing route to metal additive manufacturing,” *Mater Res Lett*, vol. 9, no. 2, pp. 71–83, Feb. 2021, doi: 10.1080/21663831.2020.1847211.

[16] H. Z. Yu *et al.*, “Non-beam-based metal additive manufacturing enabled by additive friction stir deposition,” *Scr Mater*, vol. 153, pp. 122–130, Aug. 2018, doi: 10.1016/j.scriptamat.2018.03.025.

[17] A. Gumaste *et al.*, “A Novel Approach for Enhanced Mechanical Properties in Solid-State Additive Manufacturing by Additive Friction Stir Deposition Using Thermally Stable Al-Ce-Mg Alloy,” *JOM*, Oct. 2023, doi: 10.1007/s11837-023-06044-6.

[18] P. Agrawal *et al.*, “Processing-structure-property correlation in additive friction stir deposited Ti-6Al-4V alloy from recycled metal chips,” *Addit Manuf*, vol. 47, Nov. 2021, doi: 10.1016/j.addma.2021.102259.

[19] J. Kincaid *et al.*, “Process planning for hybrid manufacturing using additive friction stir deposition,” *Manuf Lett*, vol. 37, pp. 26–31, Sep. 2023, doi: 10.1016/j.mfglet.2023.07.001.

[20] D. Z. Avery *et al.*, “Evaluation of Microstructure and Mechanical Properties of Al-Zn-Mg-Cu Alloy Repaired via Additive Friction Stir Deposition,” *J Eng Mater Technol*, vol. 144, no. 3, Jul. 2022, doi: 10.1115/1.4052816.

[21] “Designation: E8/E8M − 21 Standard Test Methods for Tension Testing of Metallic Materials 1”, doi: 10.1520/E0008_E0008M-21.

[22] O. G. Rivera *et al.*, “Microstructures and mechanical behavior of Inconel 625 fabricated by solid-state additive manufacturing,” *Materials Science and Engineering: A*, vol. 694, pp. 1–9, May 2017, doi: 10.1016/j.msea.2017.03.105.

[23] M. B. Lezaack and A. Simar, “Avoiding abnormal grain growth in thick 7XXX aluminium alloy friction stir welds during T6 post heat treatments,” *Materials Science and Engineering A*, vol. 807, Mar. 2021, doi: 10.1016/j.msea.2021.140901.

[24] J. Q. Su, T. W. Nelson, R. Mishra, and M. Mahoney, “Microstructural investigation of friction stir welded 7050-T651 aluminium,” *Acta Mater*, vol. 51, no. 3, pp. 713–729, Feb. 2003, doi: 10.1016/S1359-6454(02)00449-4.

[25] I. Charit and R. S. Mishra, “Abnormal grain growth in friction stir processed alloys,” *Scr Mater*, vol. 58, no. 5, pp. 367–371, Mar. 2008, doi: 10.1016/j.scriptamat.2007.09.052.

[26] G. W. Zheng, H. Li, C. Lei, J. Fu, T. J. Bian, and J. C. Yang, “Natural aging behaviors and mechanisms of 7050 and 5A90 Al alloys: A comparative study,” *Materials Science and Engineering: A*, vol. 718, pp. 157–164, Mar. 2018, doi: 10.1016/j.msea.2018.01.119.

[27] C. J. T. Mason *et al.*, “Process-structure-property relations for as-deposited solid-state additively manufactured high-strength aluminum alloy,” *Addit Manuf*, vol. 40, Apr. 2021, doi: 10.1016/j.addma.2021.101879.

[28] “MMPDS-17 Chapter 3 Aluminum,” 2022.

Chapter 3: Effect of Zirconium on Processibility

3.1. Manuscript 2: Influence of Zirconium Dispersoid Particles Processing and Quench Sensitivity of Additive Friction Stir Deposition High Strength Al-Zn-Mg-Cu

Greg D. Hahn[1], Kendall P. Knight[1], R. Joey Griffiths[2], and Hang Z. Yu[1*]

[1]Department of Materials Science and Engineering, Virginia Tech, Blacksburg, VA 240161, USA.

[2]Lawrence Livermore National Laboratory, Livermore, CA 94550, USA.

[*]Corresponding author: hangyu@vt.edu

Abstract

The AA7050 with and without Zr dispersoid particles were processed via AFSD and the quench sensitivity of the alloys was studied. It was found that the presence of Zr was detrimental to the quench sensitivity of the alloy in post-deposition heat treatment. This was attributed to the loss of coherency of the Al_3Zr dispersoid particles. It was found that the addition of Zr has little effect on the processing of the alloy, texture suggests similar flow behaviors between the alloys. It was found that abnormal grain growth (AGG) occurred in post-deposition solutionizing treatments and for the Zr-free system this AGG was attributed to the lack of secondary pinning particles. Conventional AA7050 processed with a protrusion tool underwent abnormal grain growth which was attributed to high flow stresses leading to an unstable grain structure. Texture analysis comparing featureless and protrusion prints in the as-printed state show significant differences; protrusion tools more homogenously mix material and force lateral flow whereas the featureless tool shows evidence of shear localization at the layer-to-layer interface demonstrated by different directions of the shear plane. This work demonstrates that high-strength aluminums utilizing the $L1_2$ $Al_3(Zr,Sc)$ dispersoid system are not compatible with AFSD; their loss of coherency lends to heterogeneous precipitation and inability to be restored to full strength in thicker sections.

Keywords: Quench Sensitivity, Dispersoid Particle, $L1_2$, Abnormal Grain Growth, Material Flow

Introduction

The 7xxx series aluminum alloys are the most common material system utilized for aerostructures [1], [2]. Given their low density and high strength, the high-strength 7xxx series alloys provide the high strength to weight ratio necessary to facilitate flight. The aerospace aluminum alloys utilize a complex combination of multiple second phase particles, deformation induced texture, and optimized thermal treatments to facilitate appropriate properties [1], [3]. These microstructures are often referred to as “hierarchical” referring to multiple length scales that are designed within the alloy for optimal performance. This work will focus on a specific scale, the dispersoid particle. Dispersoid particles are of utmost performance to the high-strength aluminums; the thermally stable dispersoid particles provide pinning for grain boundaries and allow for anisotropy to be introduced into components via texture [1]–[4]. Early 7xxx series

aluminum alloys utilized chromium and manganese dispersoid particles that formed in the cast billet upon solidification [1], [2], [5]. These incoherent dispersoid particles were discovered to be responsible for reduced mechanical performance in thick sections. The reduced performance is due to heterogeneous precipitation of strengthening phases on the particles which locally depletes solute and weakens the material. After the incoherent boundaries were discovered to be detrimental, zirconium rich dispersoid particles were implemented [1]. The zirconium forms a metastable $L1_2$ particle with fully coherent interfaces with the aluminum matrix [4]–[7]. The Al_3Zr particle has been widely used since the 1980s and significantly reduced the quench sensitivity of the high-strength aluminum alloys [1]. The most significant high-strength aluminum alloy to date is AA7050, it was introduced as a successor to AA7075 with improved quench sensitivity allowing it to be formed into thicker sections [1], [3]. Further advances in aluminum physical metallurgy have created further improvements on the alloy, notably AA7085, AA7136, and AA7150 but AA7050 is typically regarded as the most widely used 7xxx series alloy for aerostructures [1], [4], [8].

The 7xxx series aluminum alloys are based on the Zn-Mg system, but the highest strength alloys utilize the addition of copper [2]. These Zn-Mg-Cu alloys use the $MgZn_2$ η or η' strengthening precipitate [1], [9]–[11]. In depth explanations of the precipitation sequence and kinetics can be found in [2], [3]. In short, the precipitation of the strengthening phase is reliant on the ability to create a super saturated solid solution (S.S.S.S.), from this state, controlled thermal exposure can be utilized to nucleate and grow the strengthening phases. The yield strength of the alloy in the typical "overaged" condition is dependent on the size and volume fraction of the strengthening precipitate. Strength increases with increasing volume fraction and decreases with increasing precipitate size [1]. Typical hindrances to even dense dispersions of η-phase have been mentioned above, specifically heterogeneous precipitation of the strengthening phase on thermally stable second phase particles [1], [2], [5]. These particles are usually separated into dispersoids (previously mentioned) or constituent particles. The constituent particles consist of impurity elements, specifically Fe and Si, which form insoluble intermetallic phases [1], [2]. Heterogeneous precipitation can be avoided by utilizing coherent dispersoid particles and reducing the impurity levels of the initial billet.

Conventional processing of the Al-Zn-Mg-Cu alloys are based on thermomechanical processing, means of forming cast ingots via wrought means into a usable product form. The typical processing of wrought alloys is shown in **Manuscript 2. Figure 1**. The high compressive stresses and temperatures experienced during deformation processing typically assist in closing pores that may form during solidification [1]. This is of particular concern in the Al-Zn-Mg-Cu system, the addition of copper creates solute segregation at solidification fronts and leads to hot-cracking in melt-based processes [2], [12]. For this reason, the high strength 7xxx series alloys are considered "non-weldable". This is particularly detrimental in the realm of additive manufacturing where conventional metal additive manufacturing is based on melting and solidification (i.e., Selective Laser Melting, Laser Powder Bed Fusion, Wire Arc Additive Manufacturing). The pitfalls of additively manufacturing the high strength aluminums are well documented [13]–[16]. Utilizing ceramic nanoparticles to provide heterogeneous nucleation sites for the aluminum matrix was first developed by Martin et al. and was found to alleviate hot-

cracking problems [17]. A secondary problem of processing 7xxx series aluminums via high energy input processes is the vaporization of alloying elements, this problem is not well controlled and still stands as a barrier to more extensive use [13], [16], [18], [19]. This work will focus on solid-state additive manufacturing of AA7050, hoping to avoid the pitfalls of melt and solidification-based processes.

Additive friction stir deposition (AFSD) is an emerging solid state manufacturing technique [20], [21]. Solid bar feedstock is fed through a hollow channel within a spinning tool [22], the frictional heat generated between the feedstock and substrate allows for yielding and severe plastic flow. This process has proven successful in its ability to deposit the high-strength aluminum alloys [23]–[26], and has even been proven as the first additive manufacturing technique capable of restoring AA7075 to full strength after deposition [27], [28]. Further work has been conducted to characterize the material flow behavior and interfacial morphology [29]–[31]. This work will focus specifically on AA7050, previous studies have shown that post-deposition heat-treatment in thin sections can restore forging standard properties. As previously discussed, AA7050 is utilized in thick section wrought products for aerostructures; this work will focus on the viability of producing larger components by understanding quench sensitivity.

Materials and Methods

Materials and Manufacturing

AFSD was carried out on a MELD R2 system (MELD Manufacturing, Christiansburg, USA). 152.4 mm x 50.8 mm substrates were cut from 6.35 mm rolled AA7050-T7451 plate (Tri-Tech Metals, Rancho Cucamonga, USA). As-received AA7050-T7541 feed stock was cut from 9.53 mm thick plate along the rolling direction into 9.53 mm x 9.53 mm x 152.4 mm square feed rods. AA7050 without zirconium was cast into 9.53 mm x 203.2 mm x 152.4 mm plates via sand casting and then waterjet cut into 9.53 mm x 9.53 mm x 152.4 mm feed rods. Feed rods were coated in a graphite lubricant to aid printing.

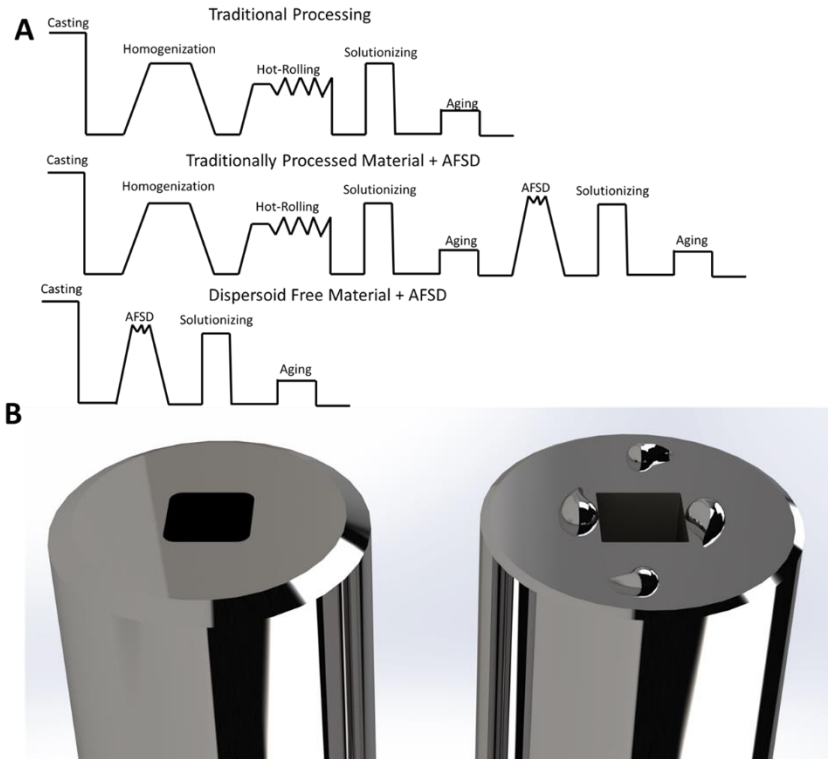

Manuscript 2. Figure 1: (A) Temperature regions experienced by AA7050 during traditional processing, traditionally processed material processed by AFSD, and the proposed cast alloy used in these experiments. (B) The two tool types used in this experiment, on the left a flat or "featureless tool" on the right a protrusion tool.

Build walls were made with two different tool types, a featureless tool, and a tool with 4-2.29mm high tear drop shaped protrusions. The featureless and protrusion tool are shown in **Manuscript 2. Figure 1**B. Stirs were started by inserting a feed rod into the hollow channel of the AFSD tool, then spinning the tool to 350 RPM and lowering to the layer height of 1 mm for the featureless tool and 1.14 mm for the protrusion tool. Material was fed at 2.1 mm/second until the material yielded and filled the region underneath the tool. After the region under the tool was filled, the material feed rate and traverse rate was increased, and the tool was translated 114.3 mm. For the featureless tool, the material feed rate was 1.27 mm/second, and the tool traverse rate was 1.69 mm/second. For the pinned tool, a slightly higher feed rate of 1.31 mm/second was used with the same tool traverse rate of 1.69 mm/second. This process was repeated 9 times to create 9-layer build walls with each layer traversing in the same direction. Four total build walls were created: 1) As-Received AA7050 Featureless. 2) As-Received AA7050 Protrusion. 3) AA7050 no Zr Featureless. 4) AA7050 no Zr Protrusions.

After printing, tensile coupons were cut out along the traversal direction of the build walls. Tensile coupons followed ASTM E8 with a gauge width of 6 mm and thickness of 2 mm [32]. Multiple microscopy samples were cut from each build wall with the viewing direction perpendicular to the traverse direction. Microscopy samples had an approximate thickness of 6 mm. Microscopy samples were mechanically polished with 1200 grit sandpaper then

electropolished with a LN_2-cooled 70 wt.% methanol-30 wt.% HNO_3 electrolyte at 30V for 30 seconds. Thermal treatments were conducted on microscopy samples as well as tensile coupons. Control tensile specimens were cut out of AA7050-T7451 rolled plate along the rolling direction as well as AA7075-T6 along the rolling direction and subjected to the heat treatments and tensile testing.

The various samples described above were subjected to differing thermal treatments. It was previously discovered that AA7050 is highly sensitive to the post-deposition heat treatment, in this work heat treatment was kept consistent. Solutionization was conducted at 470 °C for 1 hr, then either water quenched or allowed to air cool. The air cooling exaggerates the slow cooling rate that would be experienced by AA7050 found in thick components. Afterward cooling via water quench or air, samples were left to naturally age at room temperature for a week. Samples were then subjected to a two-step aging treatment. The samples were first held at 120 °C for 24 hours followed by a 160 °C hold for 30 hours matching the T73 treatment from Ou et al. [5]. The two different heat treatments are shown described in Manuscript 2. Table 1 below. Microscopy samples were held following each step, i.e., as-printed, as-solutionized and quenched, and as-aged, to understand the microstructure evolution at each step. From these microscopy samples TEM samples were taken by cutting 3mm diameter cylinders via electric discharge machining (EDM), the cylinders were then sectioned and polished to 100 µm thickness and twin jet electropolished with a 80 wt.% methanal-20 wt.% HNO_3 electrolyte at -20°C.

Manuscript 2. Table 1: Thermal Treatments

Naming Convention	Thermal Treatment
T73-WQ	470°C/1 h + W.Q. + N.A.(1)/1 wk +120°C/24 h + 160°C/30 h
T73-AC	470°C/1 h + A.C.(2) + N.A./1 wk +120°C/24 h + 160°C/30 h
(1) N.A.: Natural Aging at room temperature (21°C).	
(2) A.C.: Air Cool (cooling under natural convective flow)	

Characterization Methods

Microstructural Characterization

Alloy chemistry was checked via Bruker optical emission spectroscopy (OES) (Billerica, USA). Scanning electron microscopy (SEM) was carried out on a JEOL IT-500HR (Tokyo, Japan) with an Oxford Energy Dispersive Spectroscopy (EDS) (Abingdon, UK). Electron backscatter diffraction was carried out on a Helios 5 SEM (Thermo Fisher, Waltham, USA) equipped with an EDAX detector (Mahwah, USA). Scanning transmission electron microscopy (STEM) was carried out via a Themis TEM (Thermo Fisher, Waltham, USA).

Mechanical Testing

Tensile coupons were cut parallel to the printing direction from the middle of the build wall. Coupons were machined following ASTM E8 with a gauge thickness of 2mm and width of 6mm. Control tensile specimens were retrieved from rolled AA7050-T7451 plate along the rolling direction and AA7075-T6 along the rolling direction. Both sets of control tensile specimens were heat treated with the coupons from the printed material. Tensile testing was conducted on an Instron 4468 machine at room temperature with a strain rate of 10^{-3}/s. Engineering strain was measured using an extensometer.

Results

Chemical Composition

The chemistry of the as-received AA7050 and the AA7050 without zirconium are shown in Manuscript 2. Table 2 below. There are slight differences in the magnesium, copper, and zinc alloying content between the as-received material and the zirconium free material. Both the as-received and cast AA7050 fall within the bounds for the allowable major alloying elements from the Aluminum Association [33].

Manuscript 2. Table 2: Chemistry of As-Received and Dispersoid free AA7050

	Mg (wt.%)	**Cu (wt.%)**	**Zn (wt.%)**	**Zr (wt.%)**	**Fe (wt.%)**	**Si (wt.%)**	**Cr (wt.%)**
AA7050 [33]	1.9-2.6	2.0-2.6	5.7-6.7	0.08-0.15	<0.15	<0.12	<0.04
AA7050 as-received	1.96	2.0	6.10	0.14	0.12	0.06	<0.01
AA7050 Dispersoid Free	2.21	2.19	6.50	<0.01	0.10	0.04	<0.01

Mechanical Testing

Uniaxial tension testing was performed to understand the effect of quench rate on the mechanical performance of material before AFSD as well as material that was printed with a featureless and protrusion tool. The purpose of this work is not to optimize a heat treatment for AA7050, instead to understand the reduction in strength due to reduced cooling rates from the solutionizing temperature. Yield strength will be used as a comparable metric between all the tensile samples. The resulting yield strengths are shown in Manuscript 2. Figure 2 below. Manuscript 2. Figure 2A shows the yield strength for tensile samples retrieved from AA7050 and AA7075 rolled plate. The difference in yield strength between the water quenched and air-cooled samples is much more significant in the AA7075 compared to the AA7050. This yield strength drop off signifies that AA7075 is a more quench sensitive alloy than AA7050. Manuscript 2. Figure 2B shows the yield strengths for the as-received AA7050 and AA7050 without Zr subjected to printing with the featureless tool. The as-received and then printed material has a more significant yield strength drop off compared to the rolled plate material shown in Manuscript 2. Figure 2A. The AA7050 without Zr in Manuscript 2. Figure 2B shows almost no change in yield strength between the water quenched and air-cooled sample. The prints conducted with the protrusion tool are represented in Manuscript 2. Figure 2C. The as-received AA7050 that underwent the printing

process with a protrusion tool has a comparable drop in yield strength to the featureless tool. The cast alloy without Zr shows a drop in yield strength after being processed with the protrusion tool.

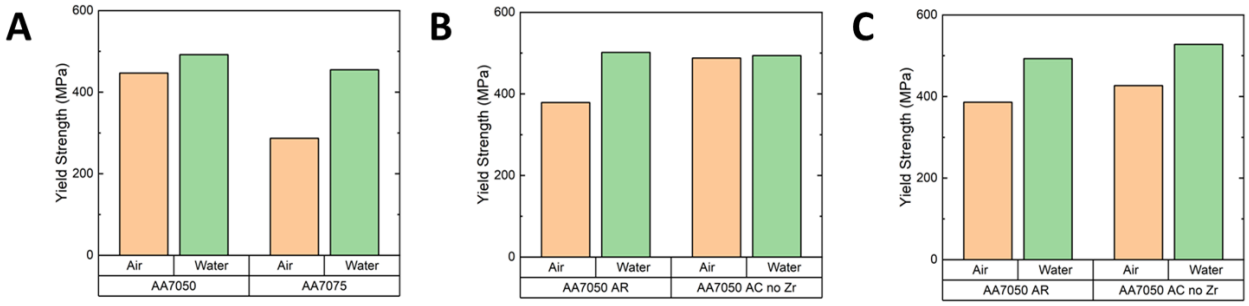

Manuscript 2. Figure 2: Comparison of yield strength for water quenched and air cooled specimens (A) AA7050 and AA7075 retrieved from rolled plate. (B) Samples from AFSD deposition conducted with featureless tool. (C) Sample from AFSD deposition with protrusion tool.

Microstructural Characterization

SEM

Backscatter SEM imaging was used to understand the presence of any large intermetallic particles within samples. For consistency, images and energy-dispersive x-ray spectroscopy was conducted within the bottom deposition layer of the following samples: 1) As-printed. 2) Printed, solutionized water quenched and aged. 3) Printed, solutionized air cooled and aged. This grouping of samples was repeated for each of the print conditions, i.e., AA7050 as-received with the featureless and protrusion tools and AA7050 without Zirconium with a featureless and protrusion tool. Manuscript 2. Figure 3 shows the resulting images and line scans for the as-received AA7050 subjected to printing with the featureless tool. The location of the number denoting the line scan corresponds to the zero distance within the line scan plot. Manuscript 2. Figure 3A-C correspond to the as-printed, solutionized-water quench-age, and solutionized-Air cool-age samples respectively. Line scans of prominent particles were conducted denoted by arrows and corresponding number. In the as-received material, the prominent particles consistently show corresponding peaks with copper and iron, leading to the conclusion that the particles are most likely Al_7Cu_2Fe constituent particles. Manuscript 2. Figure 3B demonstrates that the solutionizing step was successful, the extensive grain boundary precipitates are no longer present and prominent particles correspond to the Al_7Cu_2Fe particle. Allowing the sample to cool from the solutionizing temperature in air provides a stark contrast (Manuscript 2. Figure 3C), grain boundary precipitation has occurred, and substantial overgrown precipitates are present in the matrix. The largest particles are still corresponding to Cu and Fe constituent particles.

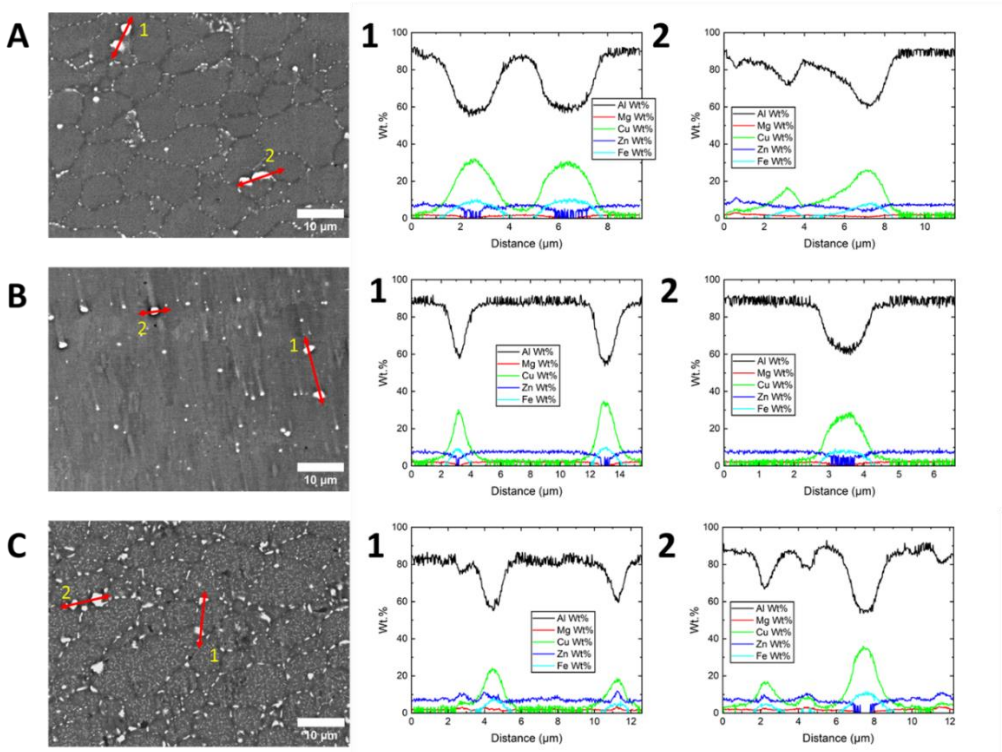

Manuscript 2. Figure 3: Backscatter SEM images and corresponding EDS scans of as-received AA7050 printed with a featureless tool. (A) As-Printed. (B) Printed and T73-WQ. (C) Printed and T73-AC.

Manuscript 2. Figure 4 shows backscatter images for the as-received AA7050 subjected to printing with the protrusion tool. Manuscript 2. Figure 4A-C correspond to the as-printed, solutionized-water quench-age, and solutionized-air cool-age samples respectively. Comparing Manuscript 2. Figure 3A to Manuscript 2. Figure 4A, the extent of grain boundary precipitation appears comparable, but the precipitation within the grain interior appears more extensive. In the as-printed state shown in Manuscript 2. Figure 4A, there are similar large particles corresponding to peaks in Fe and Cu attributable to Fe-rich constituent particles, however in line scan 2 there are a group of particles captured that do not show the presence of Fe and Cu, but instead Mg and Zn. Of particular interest is the first peak at approximately 2 µm showing an increase of copper without a second peak. This may suggest the presence of Al_2Cu θ-phase, this is a high temperature phase typically observed in the 2xxx series Al-Cu alloys; its presence within the 7xxx series would be detrimental as it does not dissolve in typical solutionizing treatments. Manuscript 2. Figure 4B shows a drastic reduction in grain boundary precipitates as expected after a solutionizing heat treatment, but line scan 1 shows a lone copper peak around 3 µm. This again points to the presence of θ-phase and that the particle survives the solutionizing step meant to dissolve secondary phases. Manuscript 2. Figure 4C shows the effect of improper cooling rate; grain boundary precipitation is extensive and overgrown precipitates are visible within the matrix. Line scan 1 and 2 show evidence of overgrown η-phase directly adjacent to constituent particles. Line scan 3 shows several overgrown precipitates along the grain boundary corresponding to Zn-Mg-Cu, most likely overgrown η.

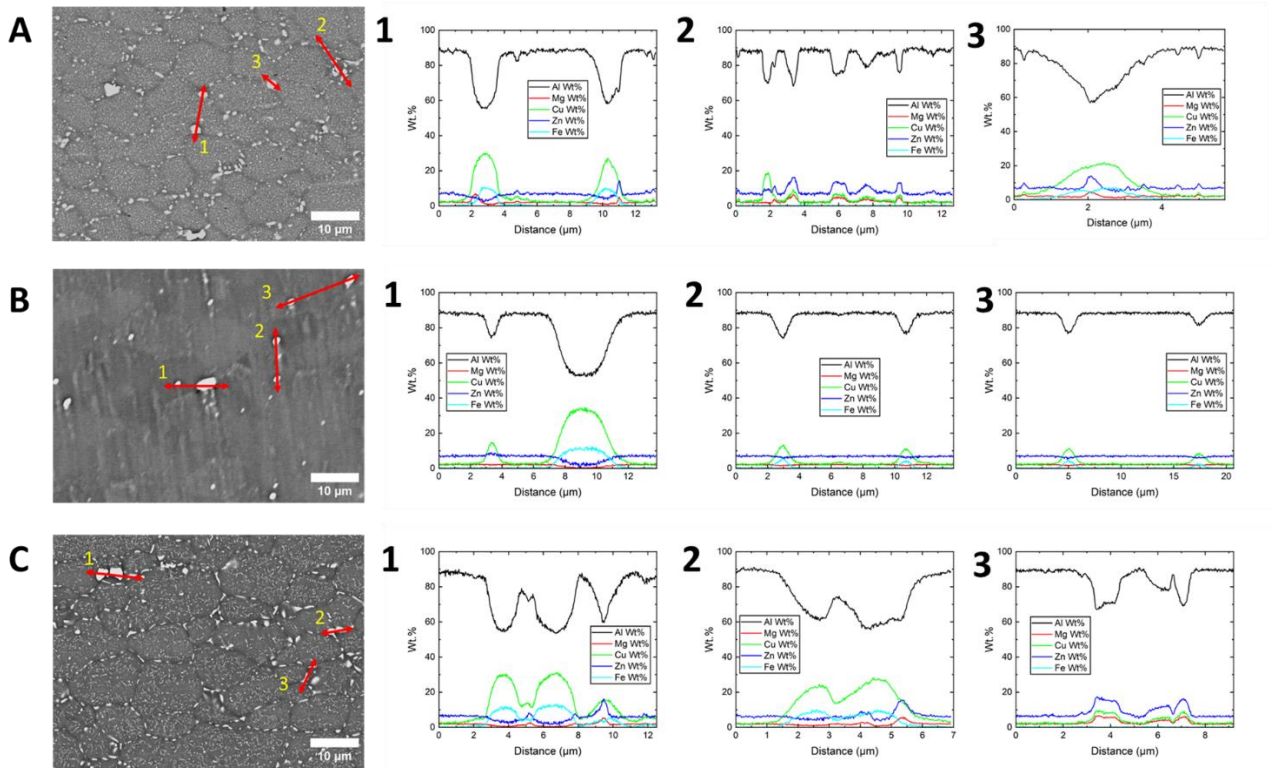

Manuscript 2. Figure 4: BSED images and EDS scans for as-received AA7050 printed with protrusion tool. (A) As-Printed. (B) Printed and T73-WQ. (C) Printed and T73-AC.

The results of the cast AA7050 without Zr subjected to printing with the featureless tool is shown in Manuscript 2. Figure 5. Manuscript 2. Figure 5A-C show the as-printed, solutionized-water quench-age, and solutionized-air cool-age sample respectively. In the as-printed state (Manuscript 2. Figure 5A) there is evidence of extensive grain boundary precipitation with limited grain interior precipitation compared to Manuscript 2. Figure 3A and Manuscript 2. Figure 4A. The resulting line scans of the as-printed material show evidence of a small Fe rich particle in line scan 1 as well as several Zn-Mg-Cu rich particles. Line scan 2 shows evidence of a Cu-Mg rich particle most likely Al_2CuMg S-phase. Line scan 3 shows a similar peak around 7 µm. After solutionizing, there are grouping of several large particles. Line scan 1 shows a very large ~7 µm wide Cu-Mg rich particle most likely S-phase. Line scan 2 shows two small Fe peaks corresponding to ~1 µm wide particles. Line scan 3 shows another Cu-Mg peak, pointing again to the presence of S-phase after solutionizing. The presence of S-phase after heat treatment is detrimental to the performance of the alloy, it provides a site for localized corrosion as well as a site for fatigue crack initiation. Manuscript 2. Figure 5C shows a vast reduction in grain interior precipitation compared to Manuscript 2. Figure 3C and Manuscript 2. Figure 4C, the precipitation appears to have some orientation horizontally across the image; this may be due to the direction of the shear during the printing process. Line scans 1 and 2 correspond to Fe-Cu peaks attributed to constituent particles while line scan 3 shows another Cu-Mg rich particle.

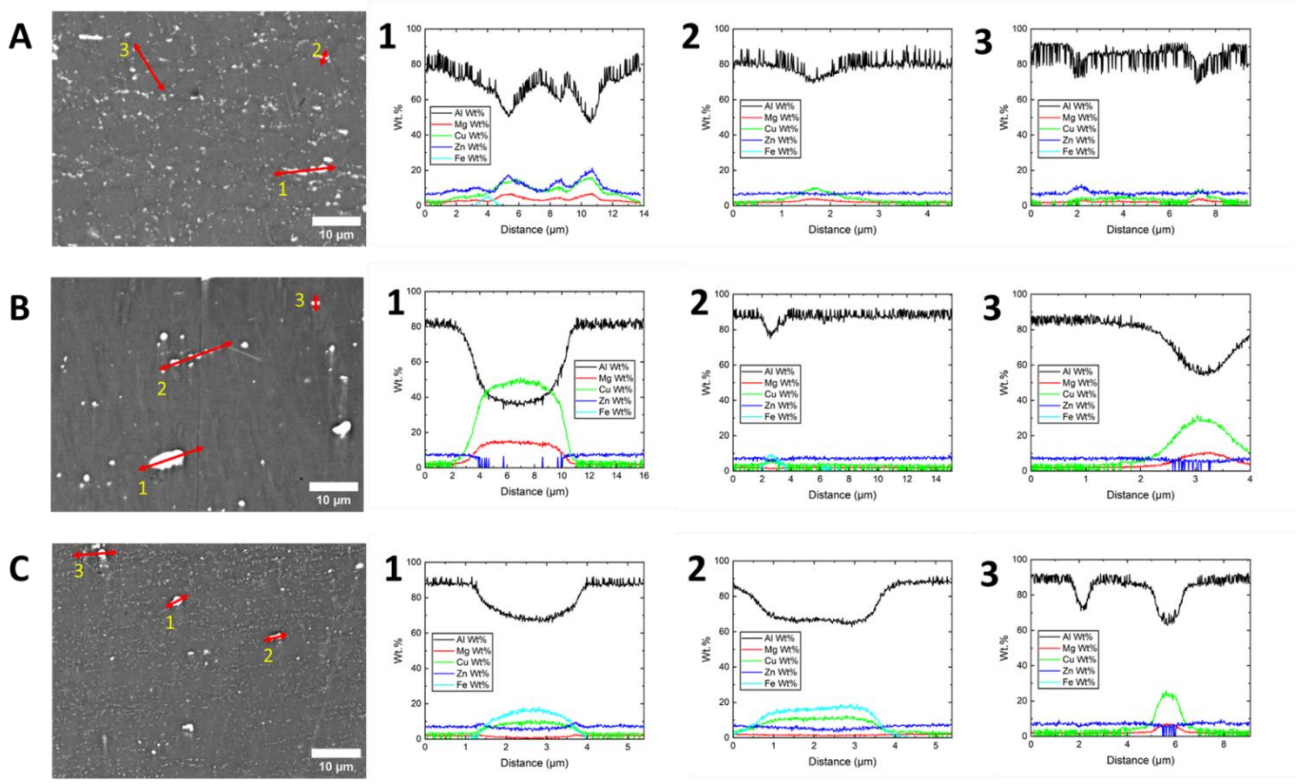

Manuscript 2. Figure 5: BSED images and EDS scans of Zr-free AA7050 printed with featureless tool. (A) As-Printed. (B) Printed and T73-WQ. (C) Printed and T73-AC

The backscatter SEM images of AA7050 printed with a tool with protrusions are shown in Manuscript 2. Figure 6A-C. Manuscript 2. Figure 6A-C correspond to the as-printed, solutionized-water quench-aged, solutionized-air cool-aged samples respectively. Manuscript 2. Figure 6A shows extensive grain boundary precipitation as well as large overgrown precipitates within the grain interiors. Line scan 1 characterizes the second phase particles along a grain boundary, peaks with Zn-Mg-Cu are most likely the presence of η while peaks of just Mg-Cu are most likely S-phase. Line scan 2 captures two Fe-rich constituent particles as well as an overgrown η particle along the grain boundary. Line scan 3 captures another Fe-rich constituent particle. Manuscript 2. Figure 6B shows many dispersed round particles and little grain interior precipitation. The spectra captured in line scan 1 shows two constituent particles, line scan 2 shows an S-phase particle and a Fe-rich constituent, and line scan 3 shows faint spectra of an S-phase particle. The air cooled and aged sample shown in Manuscript 2. Figure 6 shows extensive grain interior precipitation, more so than the as-printed condition. This level of precipitation is detrimental to any mechanical performance of the alloy.

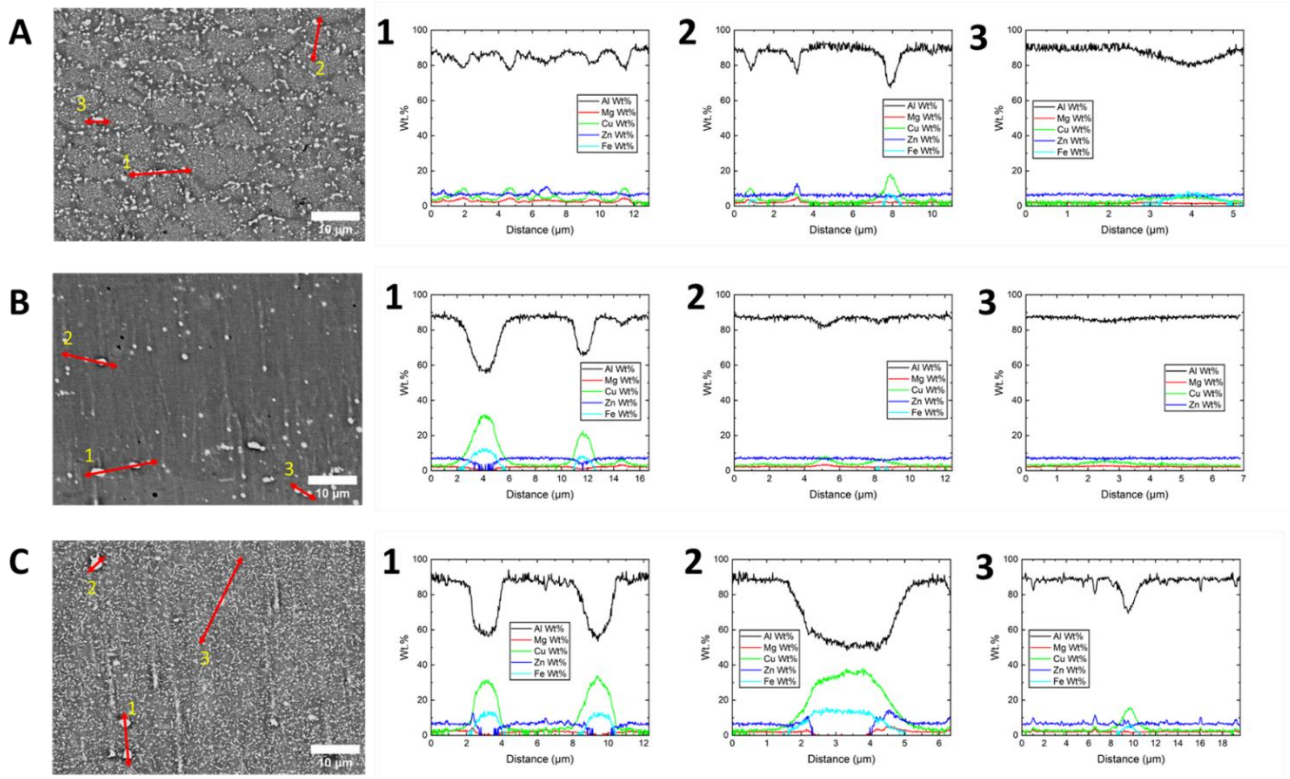

Manuscript 2. Figure 6: BSED images and EDS scans of Zr-free AA7050 printed with protrusion tool. (A) As-Printed. (B) Printed and T73-WQ. (C) Printed and T73-AC.

EBSD

Previous studies on post-deposition heat treatment of AA7050 pointed to the possibility of grain instability leading to abnormal grain growth in specific regions. To study the grain characteristics EBSD was conducted at the substrate-layer 1 interface, layer 4-layer 5 interface, and layer 9-layer 8 interface. EBSD was conducted on the as-printed material as well as material subjected to solutionizing and water quenching. If grain growth were to occur in the material, it is expected to be observed during the high temperature solutioning stage.

Manuscript 2. Figure 7 shows the inverse pole figure (IPF) maps, grain average misorientation (GAM) maps, as well as the corresponding pole figures (PF) of the featureless as-printed material. The column on the left (A-C) shows the conventional AA7050 while the column on the right shows AA7050 without Zr. The images are oriented with the direction of the build vertically, Manuscript 2. Figure 7A and D correspond to the layer 9-layer 8 interface, Manuscript 2. Figure 7B and E correspond to the layer 5-layer 4 interface, and Manuscript 2. Figure 7C and F correspond to the layer 1-substrate interface. This layout will be used in the following figures as well. The as-printed featureless prints are very similar between the as-received AA7050 and the dispersoid free AA7050. Area averaged grain sizes for the layer 8-layer 9 and layer 4-layer 5 interfaces for the as-received AA7050 are 8.7 and 8.0 µm respectively compared to 7.4 and 9.3 µm for the Zr-free AA7050. The grain size for the layer 1-substrate interface will not be reported due to rolled substrate grains skewing the distribution. In the as-printed state, both samples have

relatively low levels of misorientation within the grains except for the substrate of the Zr-free alloy having relatively larger levels of stored misorientation. The layer-to-layer interfaces can be distinguished in all images due to variations in preferred grain orientations as well as a band of fine grains at the interface region. The pole figure images show consistent behavior between the as-received and dispersoid free material. Comparing Manuscript 2. Figure 7A and B to Manuscript 2. Figure 7D and E, the preferred orientations are very similar in orientation and intensity. These profiles are found to be composites of simple shear textures, commonly observed in high strain processes and AFSD [34]–[36]. The different shear textures and orientations present across layer interfaces are discussed later in Section 4.

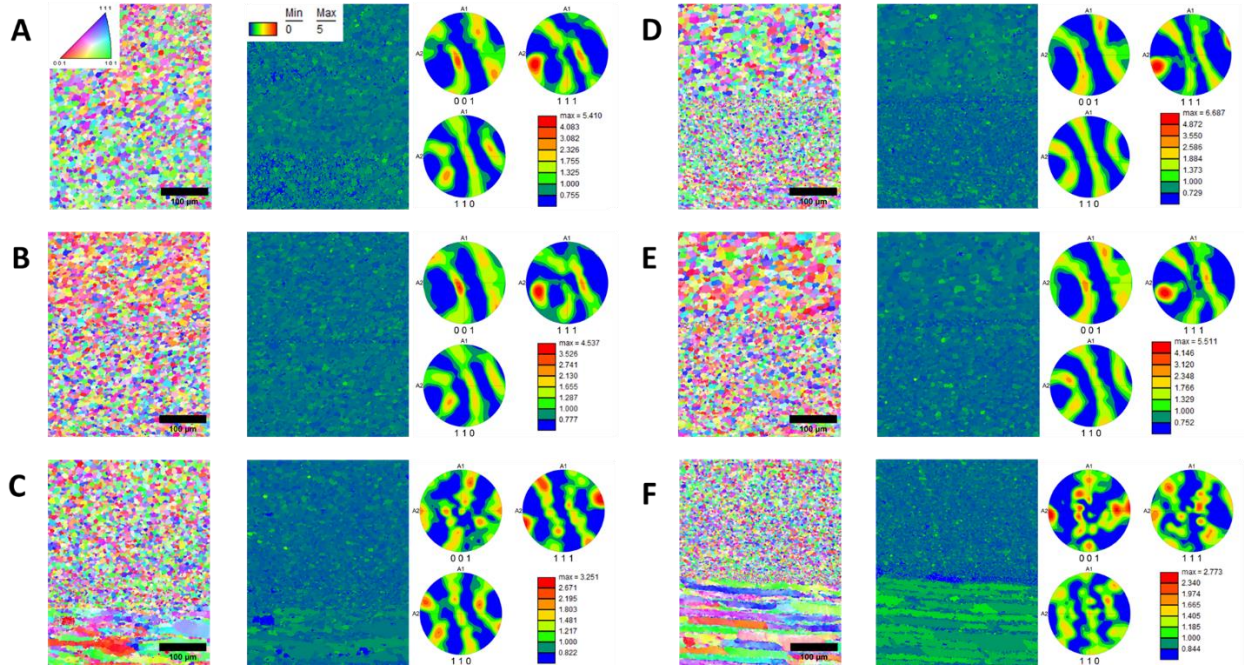

Manuscript 2. Figure 7: IPF, KAM, and PF of selected interfaces from as-printed featureless prints. (A)-(C) As-received AA7050 (A) Layer 9-layer 8. (B) Layer 5- layer 4. (C) Layer 1-substrate. (D)-(E) Zr-free AA7050 (D) Layer 9-layer 8. (E) Layer 5-layer 4. (F) Layer 1-substrate.

Manuscript 2. Figure 8 shows the material deposited with the featureless tool after solutionizing and water quenching. Like Manuscript 2. Figure 7, the left column is the as-received AA7050 and the right column is the Zr-free AA7050. There is a stark difference between Manuscript 2. Figure 8A-C and Manuscript 2. Figure 8D-F, the dispersoid free material has undergone significant grain growth during solutionizing. The area averaged grain size for Manuscript 2. Figure 8A and B are 7.8 µm and 7.7 µm respectively compared to 94 µm and 150 µm in Manuscript 2. Figure 8D and E respectively. The large grains don't allow for accurate measurement of the grain size because so few grains are represented within the image. The layer-to-layer interfaces are still present within the as-received material as a region of fine grains and there is a reduction in the grain average misorientation, most likely due to recovery during the high temperature treatment. In the Zr-free material, the layer 9-layer 8 interface and the substrate-layer 1 interface retain a region of fine grains while the layer 5-layer 4 interface is

presented with a continuous grain boundary. The highly misoriented substrate material in Manuscript 2. Figure 7F has undergone grain growth in the solutionizing treatment giving an abnormally grown grain in Manuscript 2. Figure 8F. Due to the retention of the fine grains at some interfaces, this grain growth event must be characterized as abnormal leading to a bimodal distribution of grain sizes as opposed to a more gaussian expression for normal grain growth.

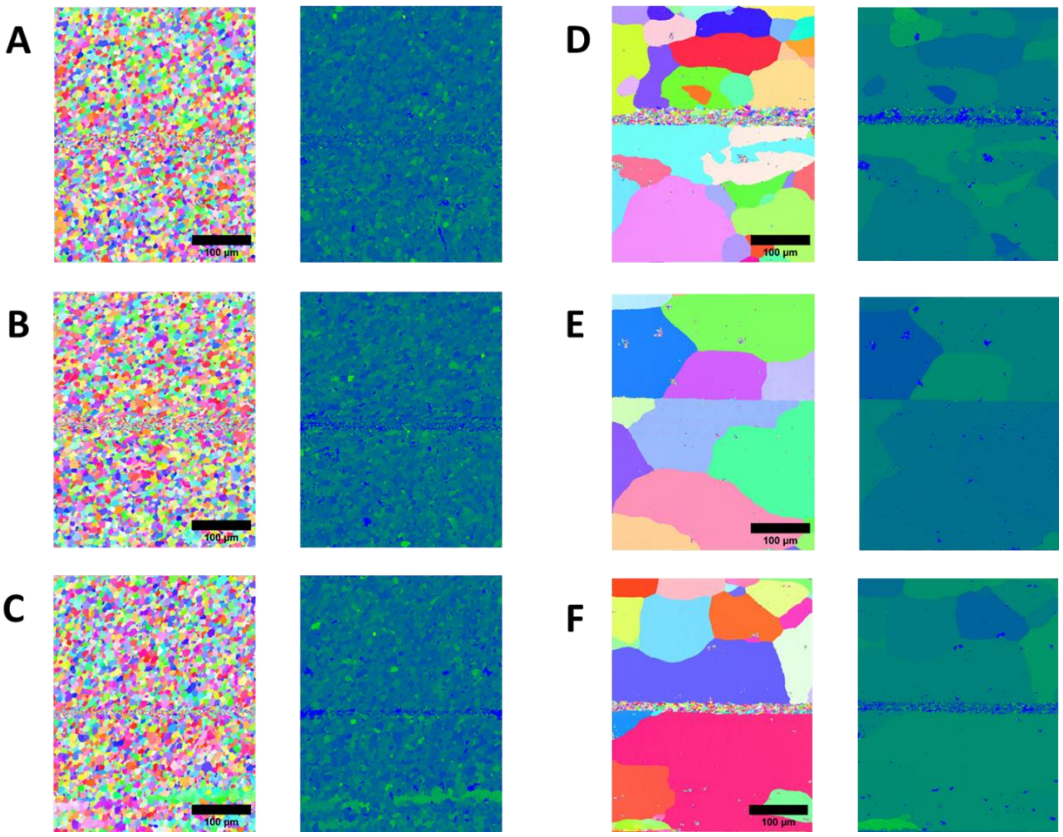

Manuscript 2. Figure 8: IPF and KAM of selected interfaces from as-solutionized featureless prints. (A)-(C) As-received AA7050 (A) Layer 9-layer 8. (B) Layer 5- layer 4. (C) Layer 1-substrate. (D)-(E) Zr-free AA7050 (D) Layer 9-layer 8. (E) Layer 5-layer 4. (F) Layer 1-substrate.

Manuscript 2. Figure 9 shows the as-printed material deposited with the protrusion tool. The left column is the as-received and printed AA7050, and the right column is the Zr-free AA7050. Comparing Manuscript 2. Figure 7 and Manuscript 2. Figure 9 shows a large difference in the misorientation within the GAM mapping. This is most pronounced when comparing Manuscript 2. Figure 7A and D to Manuscript 2. Figure 9A and D. The increased misorientation within the top layers of the print may be due to the more severe stirring action of the tool protrusions. The misorientation decreases progressing from the layer 9-layer 8 interface to the layer 5-layer 4 interface, this may be due to a more complete recrystallization and further thermal exposures. The top layer of the protrusion print would experience one more stirring event and numerous heating events if further layers were deposited. The area averaged grain size for Manuscript 2. Figure 9A-C are 5.0 µm, 10.7 µm, and 8.8 µm respectively. Comparing to the dispersoid free material (Manuscript 2. Figure 9D-F) the area averages are 8.7 µm, 6.4 µm, and 6.6 µm

respectively. The pole figures within Manuscript 2. Figure 8 reveal a number of features about the deformation with a protrusion tool. All textures assess later are found to be simple shear textures, similar to those in the featureless tool and other AFSD studies [26], [34]. Firstly, the preferred orientations vary from region to region and sample to sample, showing a more random mixing/deformation applied by the tool protrusions. Furthermore, the weakened intensity of the pole figures as compared to the featureless tool indicates weaker textures, potentially due to more random deformation or recrystallization effects that can reduce shear textures. Finally, the presence of different preferred orientations across layer-to-layer interfaces is not observed, indicating a breakdown of the interface due to feature induced deformation.

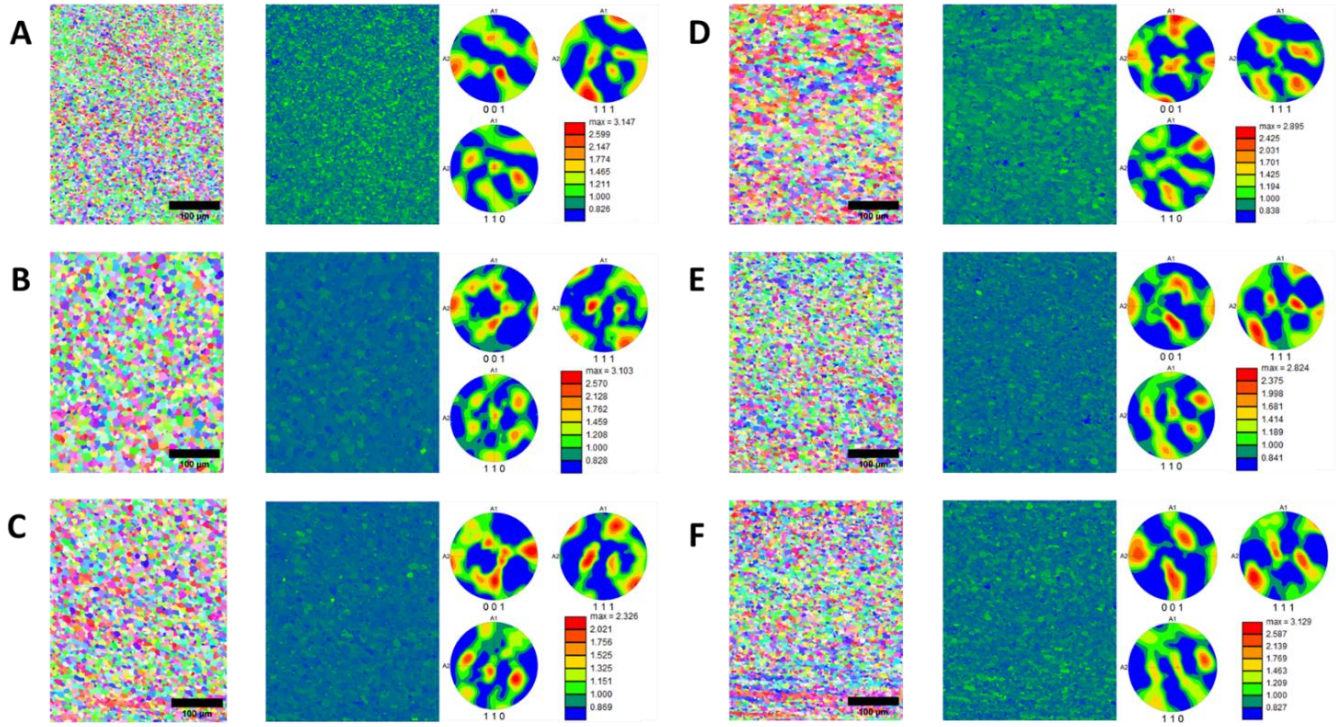

Manuscript 2. Figure 9: IPF, KAM, and PF of selected interfaces from as-printed protrusion prints. (A)-(C) As-received AA7050 (A) Layer 9-layer 8. (B) Layer 5- layer 4. (C) Layer 1-substrate. (D)-(E) Zr-free AA7050 (D) Layer 9-layer 8. (E) Layer 5-layer 4. (F) Layer 1-substrate.

The grain structure of the material printed with protrusions following solutionizing and water quench is shown in Manuscript 2. Figure 10. Like Manuscript 2. Figure 8, the material free of dispersoids has experienced significant grain growth. There is a lack of fine grains at potential interfaces, this is due to the severe breakup of layer-to-layer interfaces caused by the disruptive protrusion interactions. Interestingly, the conventional AA7050 shown in Manuscript 2. Figure 10A-C shows regions that have undergone significant grain growth as well. The layer 5-layer 4 interface shows an apparently stable microstructure, this is the region that had the largest grain size shown in Manuscript 2. Figure 9 B at 10.7 µm, the grain size shown in Manuscript 2. Figure 10B is 7.2 µm. The fine-grained region in Manuscript 2. Figure 9B still has a high grain average misorientation compared to the other regions shown.

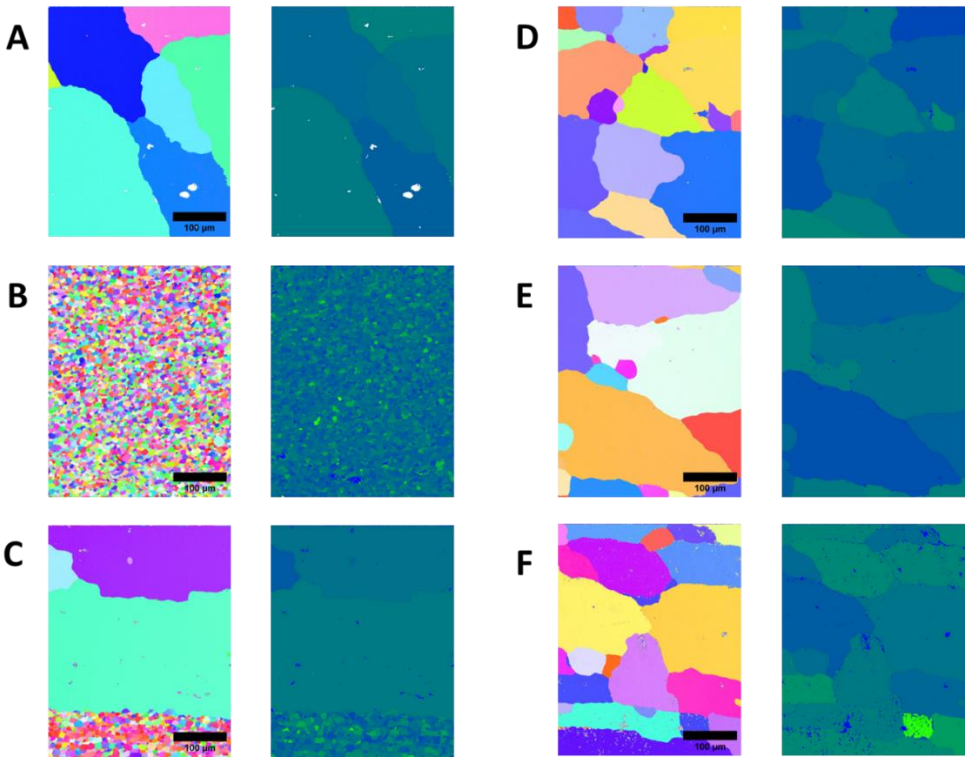

Manuscript 2. Figure 10: IPF and KAM of selected interfaces from as-solutionized protrusion prints. (A)-(C) As-received AA7050 (A) Layer 9-layer 8. (B) Layer 5- layer 4. (C) Layer 1-substrate. (D)-(E) Zr-free AA7050 (D) Layer 9-layer 8. (E) Layer 5-layer 4. (F) Layer 1-substrate.

TEM

Featureless Prints

Scanning-Transmission Electron Microscopy (STEM) was conducted with High Angle Annular Dark Field (HAADF) imaging to characterize the second phase particles of the as-printed, T73-AC, and T73-WQ material. Overview HAADF images of the featureless prints are shown in Manuscript 2. Figure 11. The left column (Manuscript 2. Figure 11A-C) corresponds to the as-received AA7050 subjected to deposition with the featureless tool. The right column corresponds to the dispersoid free AA7050. From top to bottom, the images show as-printed, printed and subjected to T73-AC, and printed and subjected to T73-WQ. The as-printed material shows very large precipitates, on the order of 100 nm and in the case of Manuscript 2. Figure 11D, evidence of dislocation walls within the grain. The variability of as-printed material due to numerous thermal exposures during printing has been documented, and it has been shown that full solutionizing and aging must be conducted to achieve full strength [23], [37]. The precipitates in the as-printed state will not be further investigated. After solutionizing, air cooling and aging (Manuscript 2. Figure 11B and E) the two samples show dramatically different results. In the conventional AA7050, there are a large number of overgrown precipitates visible within the matrix and precipitate free zones (PFZs) around the large particles. In the AA7050 without Zr there is a very large particle along the grain boundary, and a PFZ along the boundary,

but within the grain interior there is very little evidence of overgrown precipitates. In the water quenched material (Manuscript 2. Figure 11C and F), the grain interior shows homogenous and dense precipitates. In Manuscript 2. Figure 11F, heavy grain boundary precipitation can be seen along the triple junction.

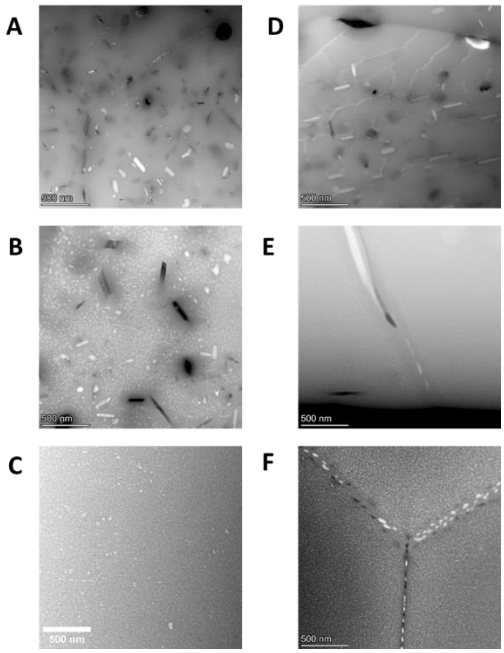

Manuscript 2. Figure 11: HAADF overview images of featureless prints. (A) As-received AA7050 in as-printed state. (B) As-received AA7050+AFSD-T73-AC. (C) As-Received AA7050-AFSD-T73-WQ. (D) As-printed zirconium free AA7050. (E) AA7050noZr-AFSD-T73-AC. (F) AA7050noZr-AFSD-T73-WQ.

Manuscript 2. Figure 12 shows further characterization of the as-received AA7050 after printing with the featureless tool and subjected to T73-AC heat treatment. Manuscript 2. Figure 12A shows a region with three particles larger than the surrounding matrix, utilizing EDX of the area, Zr rich regions can be identified. The regions directly surrounding the particles are rich in Zn-Mg-Cu and are denoted by η in the HAADF image. The Al_3Zr particle in the bottom of the image corresponds to a region rich in Mg and Cu, but devoid of Zn indicating the presence of Al_2CuMg S-phase. The presence of η on Al_3Zr particles points to the dispersoid's loss of coherency within the matrix. The heterogeneous precipitation on the dispersoid particles is not typical for this alloy system and can lead to decreased mechanical performance of components. The large PFZs around the overgrown precipitates, ~75 nm for these samples, can lead to regions that undergo strain localization and premature failure. Furthermore, large overgrown precipitates accumulate the solute that should be left in solution to provide strengthening precipitates, this is what causes the yield strength drop off shown in Manuscript 2. Figure 2B.

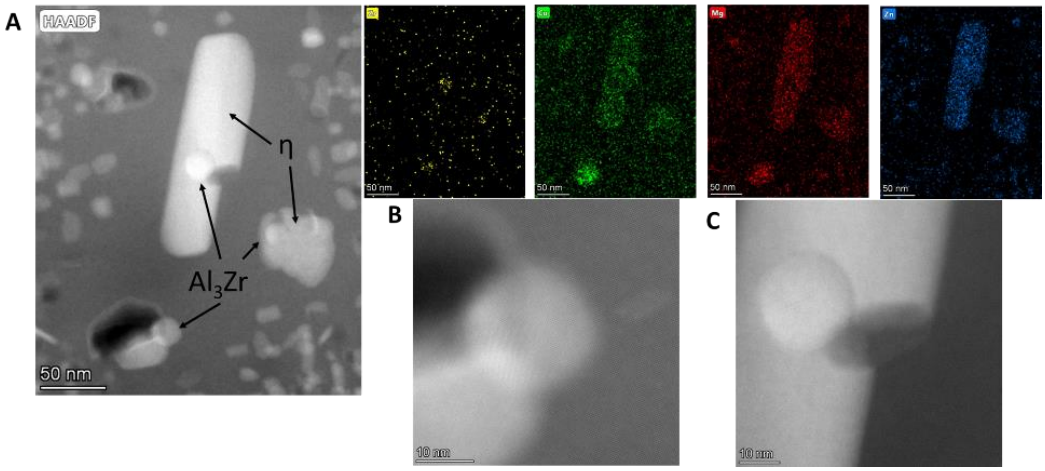

Manuscript 2. Figure 12: HAADF of as-received AA7050 after featureless AFSD and T73-AC thermal treatment. (A) Large precipitates with corresponding EDX spectra. (B) Al_3Zr dispersoid serving as S-phase nucleation site. (C) Al_3Zr dispersoid serving as η nucleation site.

Manuscript 2. Figure 13 shows a grain boundary region within the as-received AA7050 printed with the featureless tool and subjected to the T73-WQ aging treatment. Within the grain interiors, small densely precipitated η-phase is present. The EDX spectra of Manuscript 2. Figure 13A is shown for the zirconium and zinc spectra. There are three regions of zirconium of interest, the particle along the interface is shown in Manuscript 2. Figure 13B where the viewing axis is aligned along the (110) of the bottom grain. The Al_3Zr particle appears to maintain orientation with the bottom grain and possibly suggests the presence of a coherent boundary. This is possible if the recrystallization front interacting with the particle maintains the original orientation of the grain in which the L_12 type precipitate was formed in. In the case of Manuscript 2. Figure 13C, the Al_3Zr particle shown in the bottom of Manuscript 2. Figure 13A is shown with possible dislocation interactions and η-phase precipitated along its face. This suggests this dispersoid particle lost its orientation within the original grain.

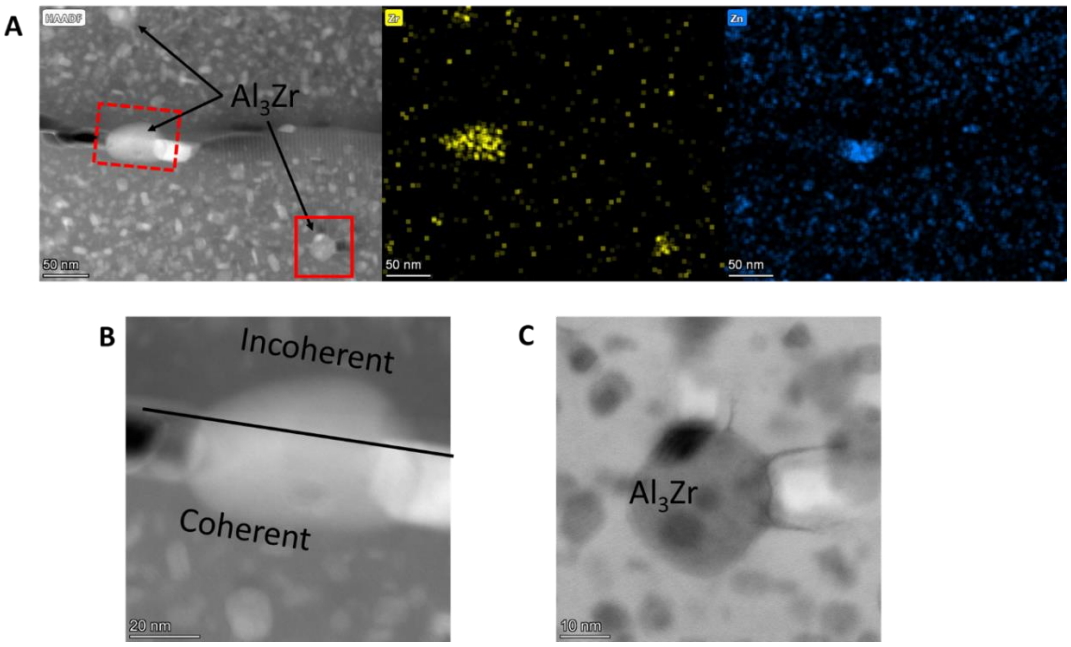

Manuscript 2. Figure 13: HAADF of as-received AA7050 subjected to featureless AFSD and T73-WQ. (A) Grain boundary showing particle-boundary interaction and corresponding EDX spectra. (B) High magnification micrograph of grain boundary Al_3Zr particle. (C) Al_3Zr particle with dislocation interactions serving as η-phase precipitate nucleation site.

In the AA7050 without the addition of Zr, there aren't dispersoid particles to serve as nucleation sites for η-phase. HAADF was utilized the characterize what sites were serving as the potential nucleation sites. Manuscript 2. Figure 14 shows a resulting HAADF image for the Zr-free AA7050 printed with the featureless tool and subjected to T73-AC heat treatment. At relatively low magnification there are large-scale η-phase precipitates present. EDX spectra show that the large-scale precipitates correspond to regions rich in iron and copper corresponding to the Al_7Cu_2Fe constituent particle. This is phase is known to act as a heterogenous nucleation site during slow cooling from solutionizing. The constituent particles have been marked by red arrows in Manuscript 2. Figure 14A. Interestingly, there is a region marked by an open arrow that shows evidence of high concentrations of copper but is devoid of other alloying elements. This most likely corresponds to the Al_2Cu θ-phase. This phase is not anticipated to dissolve during the 470 °C solutionizing sequence exposed to this alloy.

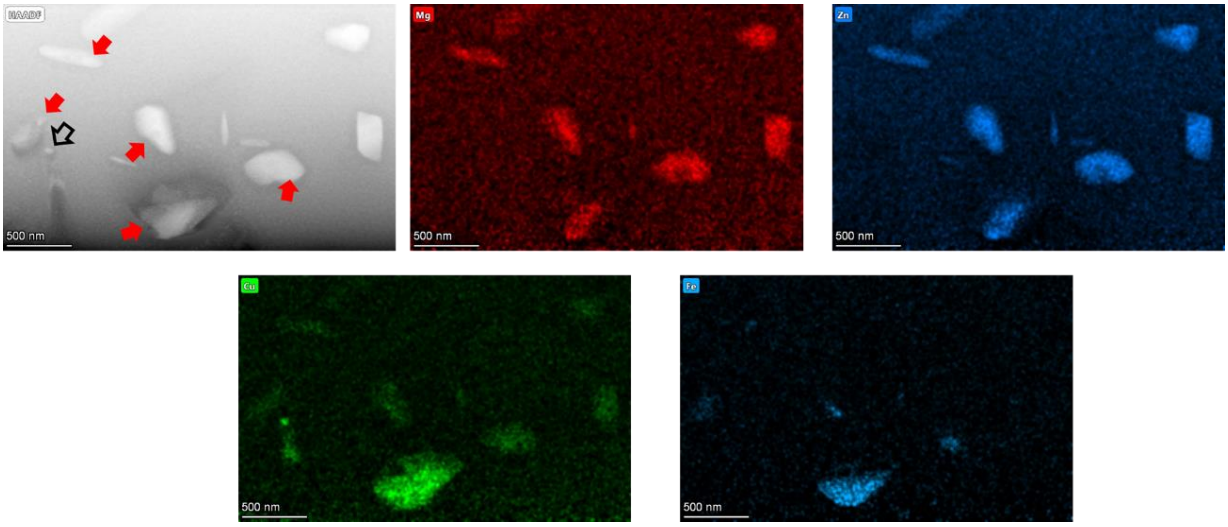

Manuscript 2. Figure 14: Large scale η-phase precipitates formed in Zr-free AA7050 subjected to featureless AFSD and T73-AC thermal treatment. Solid red Arrows correspond to Fe-Cu rich constituent particle providing nucleation site. Open arrow corresponds to likely θ-phase precipitate.

The Zr-free AA7050 after printing with the featureless tool and T73-WQ is shown in Manuscript 2. Figure 15. In the lower magnification image (Manuscript 2. Figure 15A) there are very few regions showing abnormally large precipitates, but there is a large linear section of the grain boundary. This is an uncommon feature of grain boundaries, and under further magnification (Manuscript 2. Figure 15B) it appears to be a continuous particle. EDX spectra show that the particle is rich in iron and copper, once again pointing to the Al_7Cu_2Fe constituent particle phase. The constituent particle is riddled with Mg-Zn rich η-phase precipitates that have formed along it. Following the gain boundary up, it appears that substantial Mg-Zn rich grain boundary precipitates are present. Grain boundary precipitation is common in AA7050, especially when utilizing a T7 temper, but the aspect ratio of the constituent particle is very uncommon.

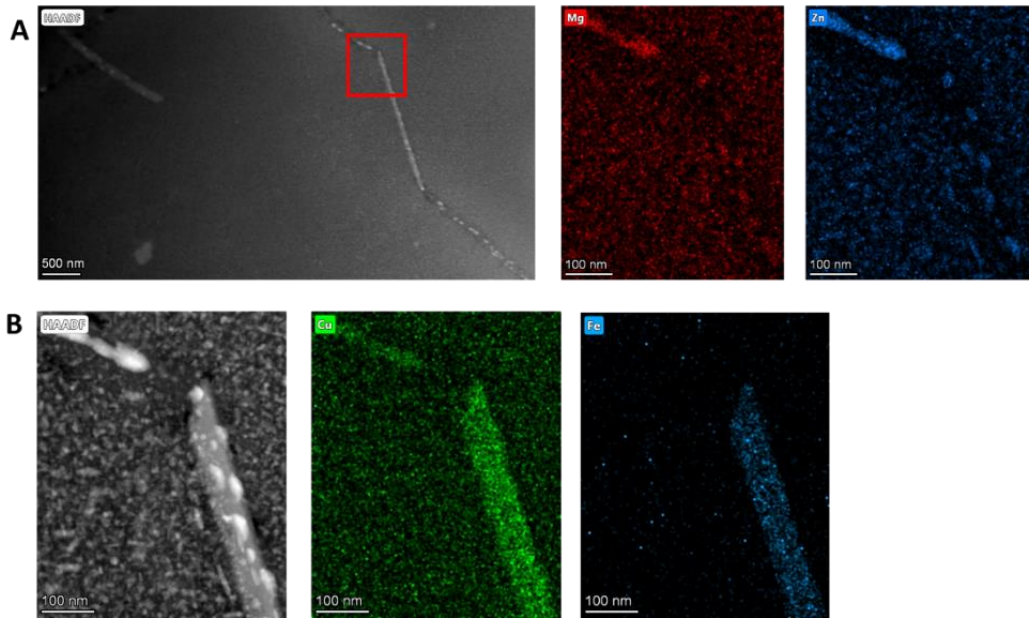

Manuscript 2. Figure 15: HAADF of Zr-free AA7050 after AFSD with featureless tool and T73-WQ thermal treatment. (A) Overview of grain boundary region showing large linear region. (B) high magnification micrograph of region with corresponding EDX

Figure 16 shows overview HAADF images of the deposits conducted with a protrusion tool. Like Manuscript 2. Figure 11, the left column represents the as-received material, and the right column shows the AA7050 without Zr. From top to bottom the figures represent 1. As-printed, 2. Printed then subjected to T73-AC treatment, 3. Printed then subjected to T73-WQ treatment. In the as-printed state both the as-received AA7050 and Zr-free AA7050 show signs of overgrown precipitates. In Manuscript 2. Figure 16A, there appears to be extensive subgrain boundaries with solute accumulating on these boundaries. Both as-printed microstructures show signs of poor mechanical performance and would necessitate post-deposition heat treatment. In the air-cooled samples, there are large precipitates with vast precipitate free zones in both samples. The grain boundary represented in Manuscript 2. Figure 16E has a PFZ of nearly 200 nm and precipitates on the scale of ~300-700 nm in length. This is highly contrasted to Manuscript 2. Figure 11E where there was very little evidence of overgrown precipitates. In the conventional AA7050, there is evidence of PFZs up to 100 nm surround the largest particles and there is evidence of particles being etched during the twinjet electrothinning process. With water quenching and subsequent aging, there is a fine precipitate structure within the matrix and substantial grain boundary precipitation. Manuscript 2. Figure 16C shows triple junctions in proximity with very small PFZs surrounding the grain boundaries despite heavy grain boundary precipitation. Manuscript 2. Figure 16F shows evidence of a subgrain structure with a multitude of overgrown precipitates along the structure, there appears to be relatively homogenous and dense precipitation within the grain interiors.

Protrusion Prints

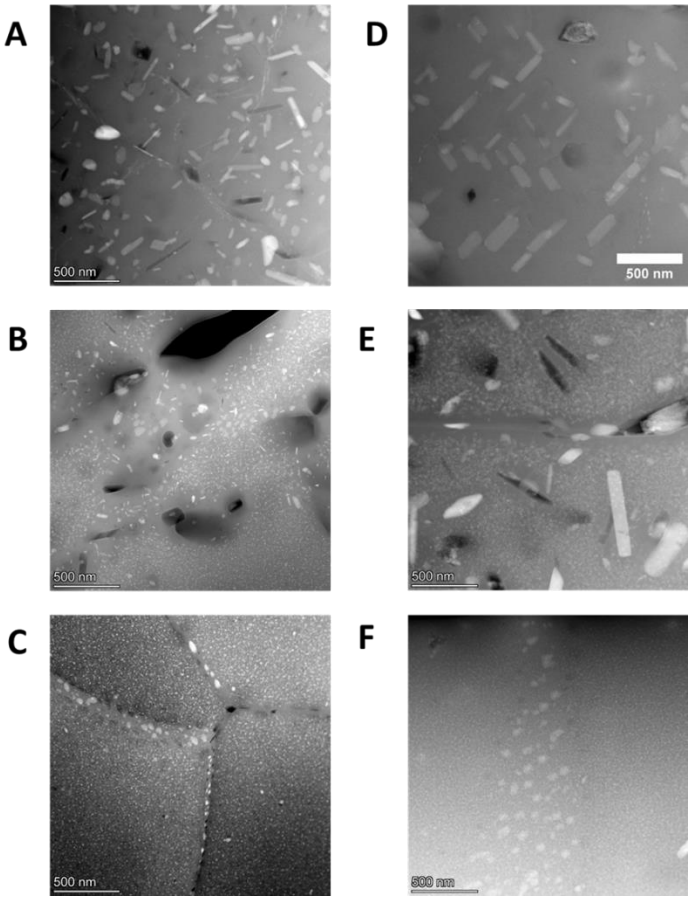

Manuscript 2. Figure 16: HAADF overview of protrusion prints. (A) As-received AA7050 in as-printed state. (B) As-received AA7050-AFSD-T73-AC. (C) As-received AA7050-AFSD-T73-WQ. (D) AA7050 without Zr in the as-printed state. (E) AA7050noZr-AFSD-T73-AC. (F) AA7050noZr-AFSD-T73-WQ

Manuscript 2. Figure 17 shows further HAADF characterization of material deposited with a protrusion tool and subjected to T73-AC thermal treatment. Manuscript 2. Figure 17A shows an overview of a grain boundary leading into a triple junction, the corresponding EDX spectra of zirconium and zinc are shown. The grain boundary shows extensive η-phase precipitates, the grain boundary is not edge on so PFZ lengths are difficult to measure. In the zirconium spectra, two main regions of interest can be observed both corresponding to particles on the grain boundary. The highlighted region is shown in higher magnification in Manuscript 2. Figure 17B where the left side of the Al_3Zr particle shares some orientation to the matrix. On the right side, a different grain is present sharing no orientation with the particle and a brighter η particle is beginning to grow on this region. Manuscript 2. Figure 17C shows a HAADF micrograph of the grain interior, a larger second phase particle is highlighted and shown in higher magnification in Manuscript 2. Figure 17D. An EDX line scan was taken through the two particles and is shown in Manuscript 2. Figure 17E. The larger particle is the Al_3Zr dispersoid particle and the brighter particle is η-phase precipitating on it.

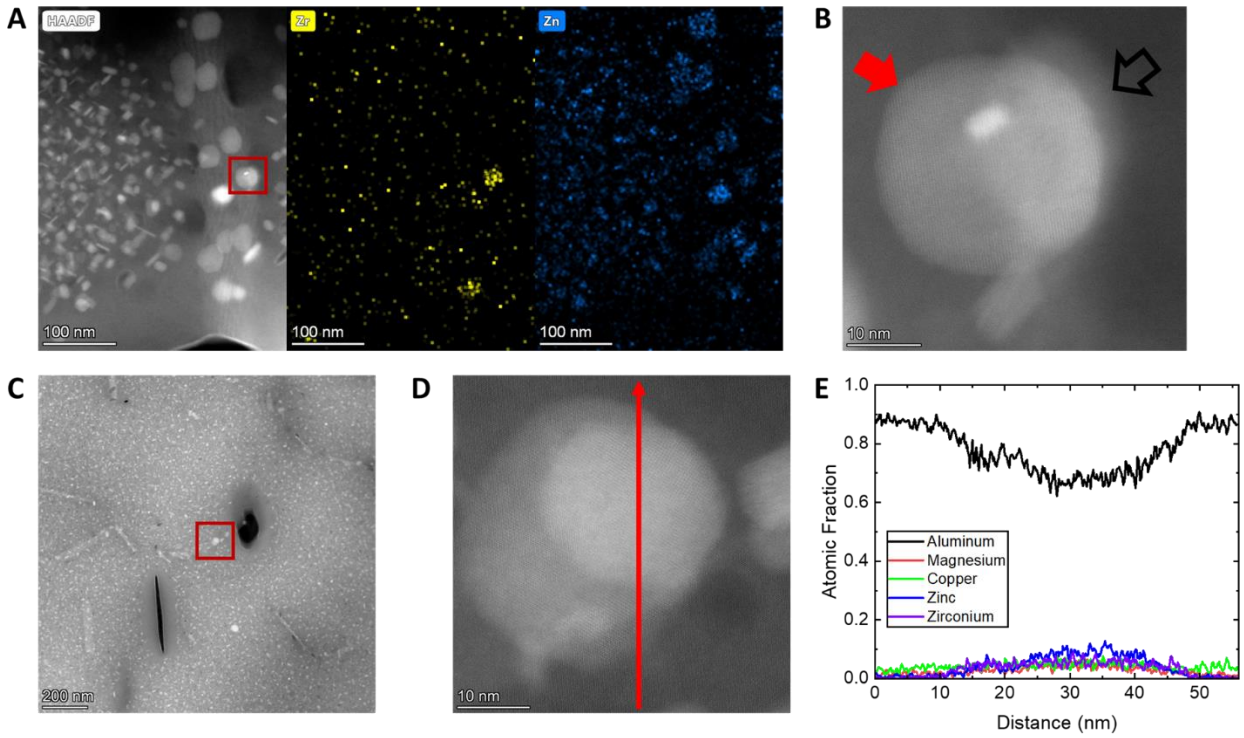

Manuscript 2. Figure 17: HAADF micrographs of as-received AA7050 after deposition with protrusion tool and T73-AC thermal treatment. (A) Grain boundary region with corresponding EDX spectra of zirconium and zinc. (B) High magnification micrograph of highlighted region in A (Closed red arrow denotes Al_3Zr, open black arrow denotes η growth). (C) Grain interior region with region of interest highlighted. (D) Heterogenous particle growth and corresponding EDX line scan. (E) EDX line scan results

Manuscript 2. Figure 18A shows a HAADF micrograph of the as-received AA7050 after deposition with a protrusion tool and T73-WQ thermal treatment. The grain interior shows dense precipitation, the only dramatic outliers correspond with the zirconium spectra shown in the EDX mapping. The three identified Al_3Zr dispersoid particles are denoted 1-3 in Manuscript 2. Figure 18A and correspond to Manuscript 2. Figure 18B-C respectively. The higher magnification images of the particles show similar trends. A round Al_3Zr dispersoid particle approximately 15-20 nm in diameter has a precipitate 1-2x its size directly adjacent to it. The larger precipitate is nearly an order of magnitude difference in size compared to the precipitates around it. This furthers the finding that the dispersoid particles are losing coherency with the matrix during the severe plastic deformation process.

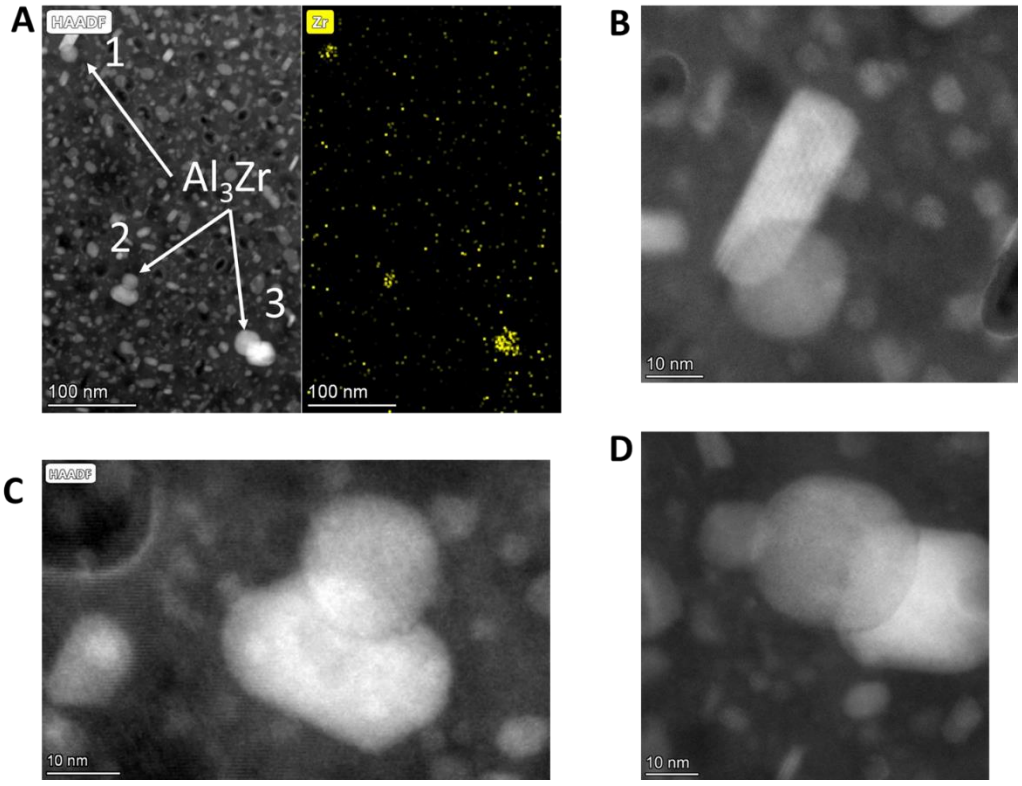

Manuscript 2. Figure 18: HAADF micrographs of as-received AA7050 after deposition with protrusion tool and T73-WQ thermal treatment. (A) Overview of grain interior with Zr EDX spectra overlay and Zr particles denoted. (B) Higher magnification micrograph of Zr particle 1. (C) Micrograph of Zr particle 2. (D) Micrograph of Zr particle 3.

In the Zr-free AA7050 processed with a protrusion tool and subjected to a T73-AC there are numerous overgrown precipitates throughout the microstructure. This is highlighted in Manuscript 2. Figure 19, where multiple precipitates reach nearly the mm scale. EDX area scans are shown for relevant elements, the large precipitates are rich in magnesium, zinc, and copper suggesting they are η-phase that has grown substantially. Investigation of the iron and silicon EDX show multiple peaks corresponding to regions within the overgrown η-phase. This suggests that the η is heterogeneously precipitating on the Fe-rich and Si-rich constituent particles (a known heterogeneous nucleation site). There also appears to be further evidence of a copper rich species present in the bottom of the image, the lack of other alloying elements present suggests a binary aluminum-copper intermetallic most likely being θ.

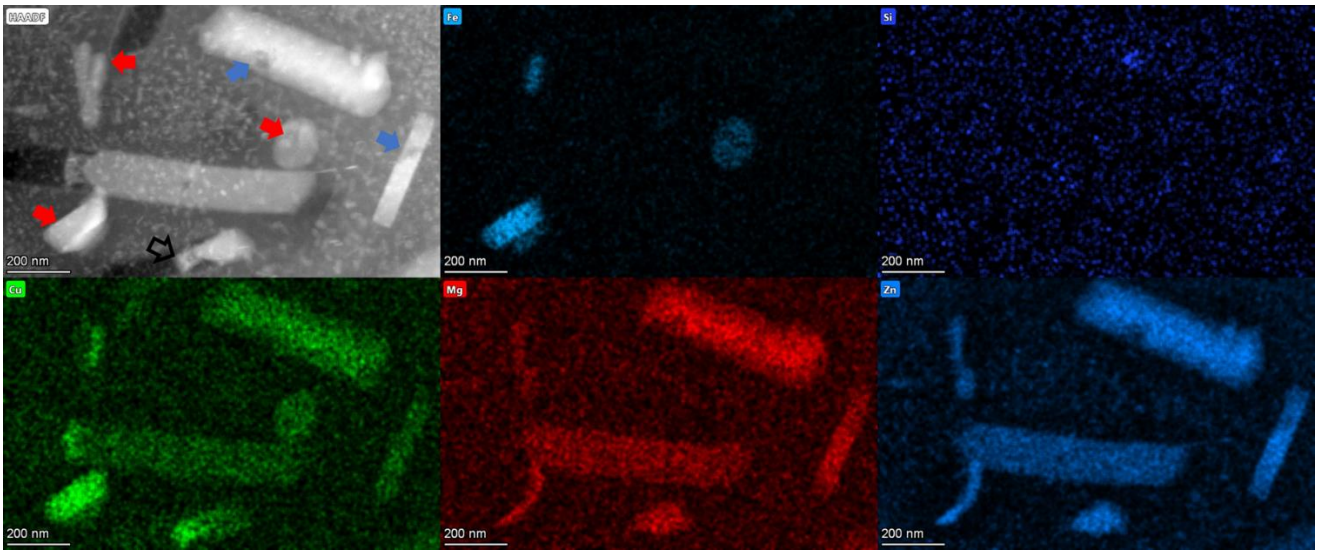

Manuscript 2. Figure 19: HAADF of dispersoid free AA7050 after deposition with a protrusion tool and T73-AC treatment. Fe-rich constituent particles are denoted with solid red arrows, Si-rich particles are shown with solid blue arrows, and open arrow shows possible θ-phase.

Manuscript 2. Figure 20 shows the zirconium free AA7050 after processing with the protrusion tool and subjected to a T73-WQ thermal treatment. In **Manuscript 2. Figure 20**A, there are regions of dense strengthening precipitates with very few abnormalities, but in the center of the image there are a series of large precipitates. These precipitates appear to be a few hundred nanometers in size. EDX scans were conducted of the region in the red boxed region and are shown to the right of **Manuscript 2. Figure 20**A. The large particles correspond to higher levels of iron and copper suggesting the Al_7Cu_2Fe constituent phase. The Fe-rich particles are denoted by the solid red arrows in the micrograph. Further investigation into the particle within the top right of **Manuscript 2. Figure 20**A (shown in the blue box) is shown in **Manuscript 2. Figure 20**B. The particle shows the iron and copper peaks as shown previously, but there is a Mg-Zn rich particle growing along the bottom of the particle. The Fe-rich constituent particles provide a potent heterogeneous nucleation site.

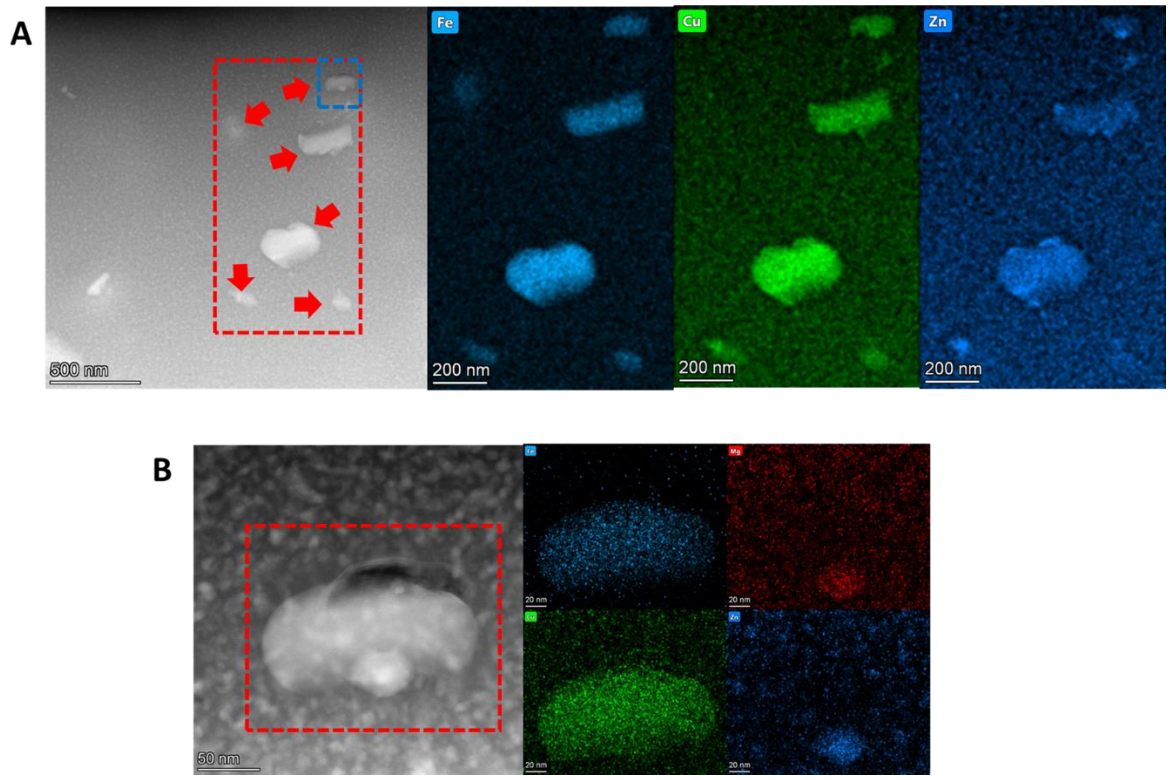

Manuscript 2. Figure 20: HAADF of dispersoid free AA7050 after deposition with a protrusion tool and T73-WQ. (A) Overview of precipitation within a grain interior showing region of EDX scan. (B) High magnification region shown in A with accompanying EDX spectra. (Note: Red solid arrows denote Fe-rich particles.)

Fractography

The fracture surfaces of all the failed tensile specimens were investigated via SEM, back-scatter imaging was used to identify any second phase particles present on the fracture surface. The as-received AA7050 processed by AFSD and heat-treated tensile specimen fracture surfaces are shown in Manuscript 2. Figure 21. The tensile specimens extracted from the featureless tool print are shown in Manuscript 2. Figure 21A and B with A showing the fracture surface of the T73-WQ sample and B showing the T73-AC treated sample. Manuscript 2. Figure 21A shows evidence of microvoid coalescence with many single micron particles present along the fracture surface. There are clearly two morphologies of particles present on the surface, one appearing spherical and several with larger aspect ratios. Manuscript 2. Figure 21B also shows microvoid coalescence as the main mode of fracture, but the exposed surface is littered with small second phase particles. The precipitates present are far too large to provide strengthening to the matrix and based on Manuscript 2. Figure 12, these may be the sites in which dispersoid particles have provided heterogeneous nucleation sites. Manuscript 2. Figure 21C and D correspond to the protrusion-T73-WQ and protrusion-T73-AC as-received samples respectively. Manuscript 2. Figure 21C shows a mixed mode fracture surface, there is evidence of microvoid coalescence as well as some smoother faceted surfaces that appear more intergranular in nature. Along the smooth fracture surface there are small particles present, this may be representing the grain

boundary precipitation observed in Manuscript 2. Figure 16C. Manuscript 2. Figure 21D shows a similar widely dispersed abundance of second phase particles seen in Manuscript 2. Figure 21B. The fracture surface has similar evidence of some intergranular nature and multiple length scales of particles present on the surface.

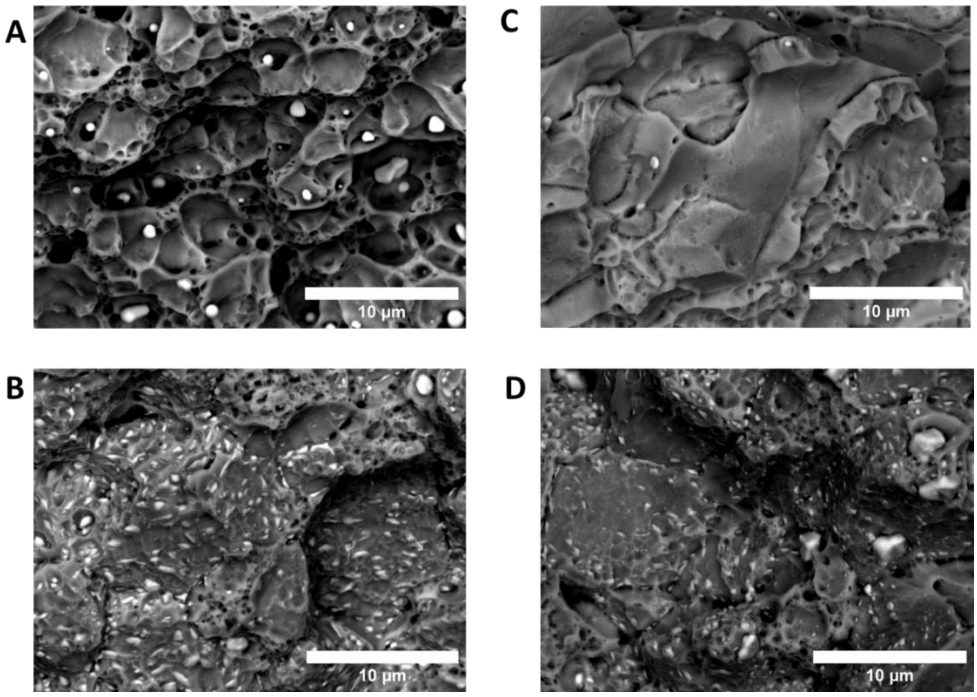

Manuscript 2. Figure 21: As-received AA7050 Post-Deposition and age fracture surfaces. (A) Featureless print +T73-WQ. (B) Featureless print + T73-AC. (C) Protrusion print + T73-WQ. (D) Protrusion print + T73-AC.

The fracture surfaces of the Zr-free AA7050 tensile coupons are shown in Manuscript 2. Figure 22. Manuscript 2. Figure 22A and B show the AA7050 after printing with a featureless tool and subjected to the T73-WQ and T73-AC respectively. The water quenched and aged sample shown in A shows evidence of typical microvoid coalescence. The origination of the microvoids appears to correlate well with the smaller second phase particles present on the fracture surface. These particles most likely caused the strain localization necessary to initiate fracture. Manuscript 2. Figure 22B shows evidence of intergranular fracture, almost the entirety of the image is consumed by a single facet of a grain. There appears to be some small second phase particles like those observed in A, but there also appears to be finer more needle like particles on the surface. These particles most likely correspond to the extensive grain boundary η-phase that was observed in Manuscript 2. Figure 11E. Manuscript 2. Figure 22C shows the AA7050 without Zr subjected to printing with a protrusion tool, then the T73-WQ thermal treatment. The fracture surface shows microvoid coalescence with finely dispersed second phase particles. Similar to Manuscript 2. Figure 22A, it appears that many of the particles are initiating the microvoids and correspond to some of the larger microvoids present on the fracture surface. Manuscript 2. Figure 22D shows the Zr-free AA7050 printed with a protrusion tool subjected to the T73-AC thermal treatment. This fracture surface shows a mixed mode crack mechanism,

there are regions of fine microvoid coalescence as well as clear signs of intergranular cracking. The surface is littered with very fine particles, these most likely correspond to the ~500 nm sized particles that were observed in Manuscript 2. Figure 19.

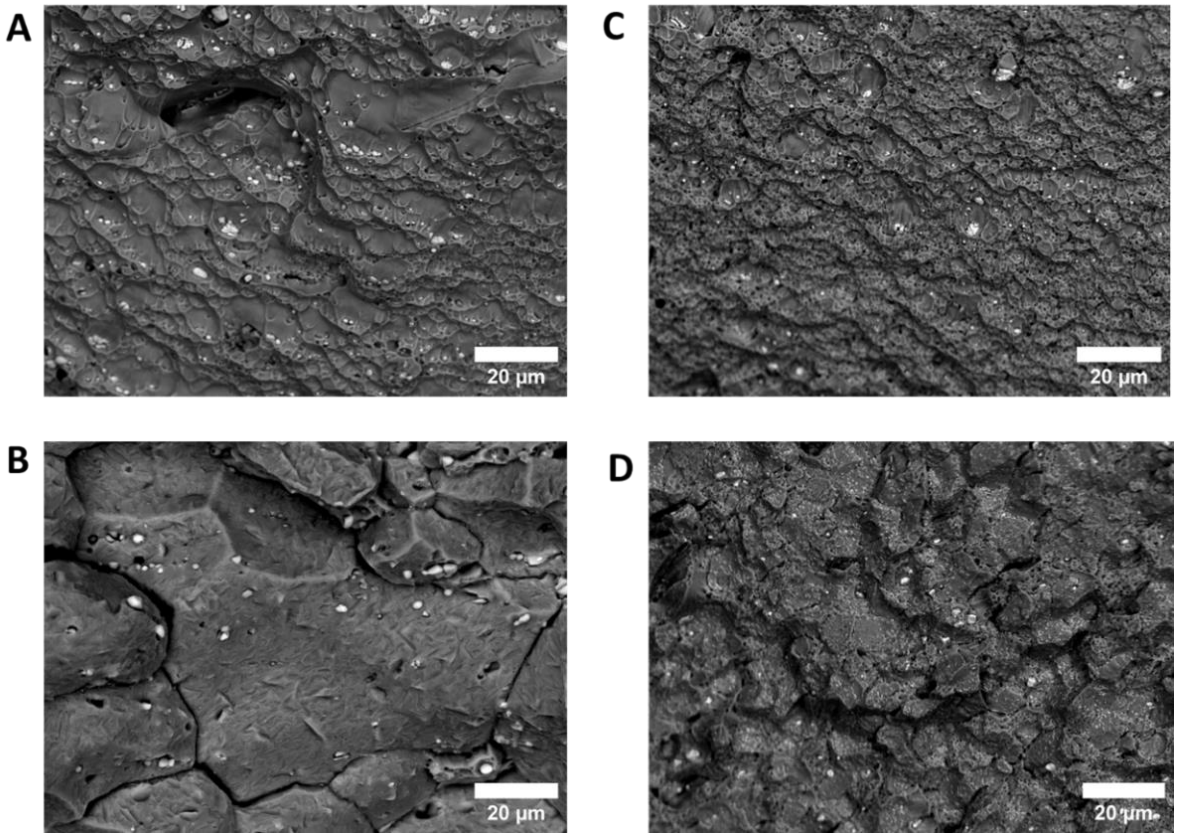

Manuscript 2. Figure 22: Dispersoid Free AA7050 Post-Deposition and age fracture surfaces. (A) Featureless print + T73-WQ. (B) Featureless print + T73-AC. (C) Protrusion print + T73-WQ. (D) Protrusion print + T73-AC.

Discussion

Texture Analysis

During characterization, it was found that the protrusion and featureless tools had significant differences in the orientation and magnitude of textures that formed in the as-printed material. To further understand this, pole figures and orientation density function maps were compared for the middle interface of the conventional AA7050 printed with the protrusion and featureless tools. In Manuscript 2. Figure 23, the viewing orientation of the EBSD scans has been rotated to align with the standard representation for shear textures, the shear plane normal and shear direction aligning vertically and horizontally respectively. In the protrusion tool, Manuscript 2. Figure 23A-C, the texture is identified as the C-type simple shear texture, which is consistent across the entire scan region. In the featureless tool, the initial EBSD scan is split into two regions as two separate textures are present at different orientations. The small interfacial region with fine grains is not included in the texture analysis. In the upper layer, which constitutes the lowest portion of Layer 5 within the build, there is a C-type simple shear texture, with the shear

plane normal and shear direction roughly 90 degrees out of phase with that observed in the protrusion tool. In the lower layer, which constitutes the top area of layer 4 within the build, the texture consists of the A-type simple shear, with a shear orientation like that shown in the protrusion tool. The difference in C and A shear components can often be attributed to different cumulative shear strain, or possibly strain rate sensitivity during shear texture formation. This variability across layers and potentially within the thickness of a deposited layer indicates a high degree of variability in flow path or flow intensity during deposition using a featureless tool. Contrary to this, the protrusion tool shows less localized variation in preferred orientations, as well as a weaker overall intensity of said textures. Though the protrusion tool did show location by location variation in orientation, Manuscript 2. Figure 9, the wider spread in these locations and reduced intensity indicates a much more homogeneous overall deformation across a build using a protrusion tool, whereas the featureless tool demonstrates potential heterogeneity within just a single layer.

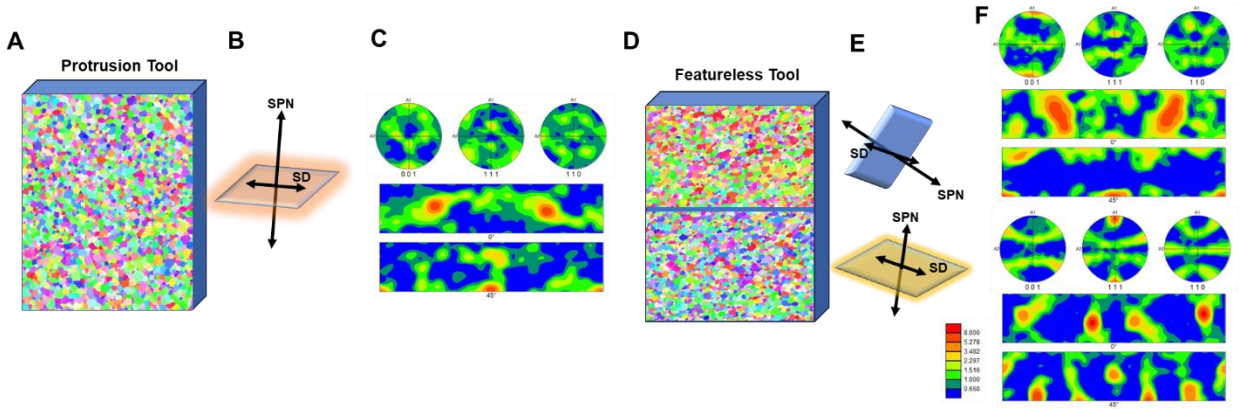

Manuscript 2. Figure 23: As-Printed texture of middle interface for conventional AA7050. (A)-(C) Protrusion tool. (D)-(E) Featureless tool.

Effect of Zirconium on Mechanical Performance

The addition of zirconium to the AA7050 system is primarily to stabilize the grain structure during thermomechanical forming and introduce anisotropy along loaded directions. Within traditional processing, great care is taken to process at adequately low enough flow stresses to prevent recrystallization during subsequent heat treatments [1]. The AFSD process is inherently different than traditional thermomechanical forming processes, the high shear and strain rate force that material to undergo dynamic recrystallization during the process. This study inspected the effect that this nonconventional processing method has on the ability for AA7050 to retain its renowned low quench sensitivity. Prior to AFSD, AA7050 has a very low quench sensitivity allowing it to be formed into thick product and still retain its mechanical performance, this is demonstrated in Manuscript 2. Figure 2A, where going from the water quenched the air cooled AA7050 materials experience a yield strength drop of 45 MPa. After printing with a featureless AFSD tool and subjected to the same thermal treatment, conventional AA7050 experiences a yield strength drop of 123 MPa, nearly 3x the conventionally processed material. Removing the zirconium from the AA7050 and subjecting it to identical processing and heat treatment coincides with only a 6 MPa drop between the air-cooled and water quenched samples. Using

STEM, the reason for this stark difference is clear; Manuscript 2. Figure 11 shows a vast difference between the air cooled traditional AA7050 and the Zr-free AA7050, within the grain interiors there is very little heterogeneous precipitation after the removal of Zr. This is further exemplified in comparing Manuscript 2. Figure 12 and Manuscript 2. Figure 14, in the conventional AA7050 the incoherent Al_3Zr dispersoids are serving as heterogeneous nucleation sites for the η-phase. Removing the dispersoids does not altogether stop heterogeneous precipitation in Manuscript 2. Figure 14, it instead pushes the nucleation to constituent particles, a known potent site for heterogeneous precipitation.

Processing conventional AA7050 with a 4-protrusion tool has a similar outcome to the featureless tool, there is a 107 MPa drop between the water quenched and air-cooled specimens. The Zr-free AA7050, contrary to the featureless tool, undergoes a similar drop in yield strength like the conventional AA7050 (101 MPa). Under STEM, the conventional AA7050 shows similar characteristics between the featureless and protrusion prints, there is evidence of Al_3Zr dispersoids losing coherency and providing sites for heterogeneous nucleation. The yield strength drop of the Zr-free AA7050 is attributed to the large number of overgrown precipitates present on Fe-rich and Si-rich constituent particles that were broken up and dispersed during the AFSD process. These particles range from 50-500 nm as opposed to the typical micron scale in conventionally processed material. In other words, going from a small number of large constituent particles to many small particles distributed across the material leads to a much higher number density of heterogenous nucleation sites. This may have a similar effect as the large number fraction of dispersoid particles.

The results of the mechanical performance of the deposited material in this study call into question the viability of processing conventional AA7050 via AFSD. After processing the detrimental effect on quench sensitivity of AA7050 cannot be dismissed. AA7050 is used in applications where large structures are required to have the full expected strength of the alloy, and increasing the quench sensitivity through processing is unavoidable for this process. This has wide reaching implications, most advanced 7xxx series aluminum alloys utilize the $Al_3(Zr,Sc)$ $L1_2$ dispersoid structure that forms coherent interfaces with the matrix. It is expected that the same loss of coherency via AFSD will plague all these alloys and significantly reduce the capability to restore the materials to full strength.

Effect of Zirconium on Grain Stability

The occurrence of abnormal grain growth in the post-deposition heat treatment of AA7050 has been previously reported and discussed. In this work, abnormal grain growth was found to occur in all samples that were devoid of Zr, as well as the conventional AA7050 samples that were processed with the protrusion tool. Using the grain growth model from Humphreys 1997 [38] to gain understanding of the fundamentals of grain stability, Equation 1 shows the growth rate of an assembly of grains with a low number of subgrains.

$$\frac{d\bar{R}}{dt} = \frac{\bar{M}\bar{\gamma}}{4\bar{R}} \quad (1)$$

Where $\bar{R}$ is the mean radius of equiaxed grains or subgrains, $\bar{M}$ is the mean grain boundary mobility, and $\bar{\gamma}$ is the mean grain boundary energy. The growth rate of a specific grain or subgrain is given by Equation 2.

$$\frac{dR}{dt} = M\left(\frac{\bar{\gamma}}{\bar{R}} - \frac{\gamma}{R}\right) \tag{2}$$

Where R is the radius of a given grain, M is the mobility of a given grain boundary, and γ grain boundary energy of a given grain. When the system is in the presence of spherical incoherent particles, a Zener pinning pressure P_z of the particles can be applied, given by Equation 3 [38], [39].

$$P_z = \frac{3F_v\gamma_i}{d} \tag{3}$$

In which F_v is the volume fraction of that particles, γ_i is the grain boundary energy of an individual grain, and d is the diameter of the particle. From this equation, a few basic conclusions can be drawn. First $P_z \propto F_v$, meaning that pinning pressure can be directly increased by increasing the volume fraction of the pinning particles. Secondly, $P_z \propto \gamma_i$, meaning pinning pressure increases as grain boundary energy increases. Lastly, $P_z \propto \frac{1}{d}$, so as particle diameter increases, pinning pressure decreases. To increase the effectiveness of the Zener pinning parameter, a high volume fraction of very small particles needs to be dispersed along grains with a high boundary energy. Finally, the effect of particle coherency must be considered. It has been derived that a coherent particle has twice the pinning pressure as an incoherent particle [39], [40].

The growth rate of an assembly of grains in the presence of spherical coherent particles is given as Equation 4 [38].

$$\frac{d\bar{R}}{dt} = \frac{\bar{M}\bar{\gamma}}{4\bar{R}} - \bar{M}\bar{P}_z = \bar{M}\bar{\gamma}\left(\frac{1}{4\bar{R}} - \frac{6F_v}{d}\right) \tag{4}$$

Following the derivation from Humphreys et al. [38], the growth rate of a given grain or subgrain is given by Equation 5.

$$\frac{dR}{dt} = \frac{M\bar{\gamma}}{\bar{R}} - \frac{M\gamma}{R} - MP_z = M\left(\frac{\bar{\gamma}}{\bar{R}} - \frac{\gamma}{R} - \frac{6F_v\gamma}{d}\right) \tag{5}$$

As mentioned previously, in both Equation 4 and Equation 5, the influence of pinning particle coherency is 2x on the P_z function. The function for determining if grain instability is present and abnormal grain growth can occur is given by Equation 6.

$$\bar{R}\frac{dR}{dt} - R\frac{d\bar{R}}{dt} > 0 \tag{6}$$

If it is held that $M = \bar{M}$, and $\gamma = \bar{\gamma}$, a limiting grain size for abnormal grain growth can be determined as shown in [38]. In the case of this system, with the textured nature of deposited material and broad size and misorientation distributions present that limiting grain size can not be utilized. Instead, understanding a few key metallurgical principles can help devolve the complex grain growth phenomena occurring. First, the dynamic recrystallization event occurring

during the printing process is causing a loss of coherency between the Al_3Zr dispersoids particles and the aluminum matrix. The loss of coherency is causing the Zener pinning pressure applied by the particles to be halved, this along with the reduced grain size is driving $\frac{d\bar{R}}{dt}$ and $\frac{dR}{dt}$ to increase. With such a small grain size and decreased pinning pressure, normal grain growth is to be expected but there is apparent abnormal growth occurring. It is believed that the abnormal grain growth may be driven via differences in grain boundary mobility; this reduced mobility is found at the layer-to-layer interfaces and may be caused by several factors; 1. graphite lubricant contamination, 2. Dispersed oxides, 3. Shear induced second phase particles. There is existing evidence that excess shear during AFSD can introduce shear induced segregation of alloying elements to grain boundaries, if localized shear occurs and causes solute segregation, high-temperature stable phases could form and stabilize grain structures. The reduced grain boundary mobility theory is supported by the lack of interlayer fine grains in the protrusion print, the protrusions are disrupting the interfacial region and dispersing any mobility impeding impurities. It appears that in the protrusion case grain boundary pinning is due to thermally stable second phase particles. The region of the as-received AA7050 printed with the protrusion tool that retained fine equiaxed grains after heat treatment is also supporting evidence of the dynamic recrystallization creating an unstably fine grain size. The larger grain size was sufficient to be stable during post-deposition heat treatment. These different theories beg the question of how can we utilize processing to stabilize a grain structure?

In the case of AA7050 devoid of Zr, it will be nearly impossible to stabilize the grain structure. The lack of dispersoid particles shows grain growth after printing for two different alloy systems [37]. Without a secondary pinning particle, the grain structure will be inherently unstable after processing via AFSD. With appropriate tooling and processing, it may be possible to avoid the localized interfacial grains that avoided grain growth and have the entire system undergo normal grain growth. The grain growth that may occur after depositing dispersoid free AA7050 may not be detrimental to the performance of the alloy. Aluminum has weak relationships with Hall-Petch strengthening, and grain boundaries are typical regions for precipitates to accumulate. The grain growth may be detrimental if the grain size grows to the scale of the component in which corrosion properties could be negatively affected [1], [41].

For the conventional AA7050 with Zr dispersoid particles, there exists the risk of undergoing abnormal grain growth due to an unstable grain size. The obvious answer to this dilemma would be to add more Zr to enable further grain stabilization, but as was previously shown this is deleterious to mechanical performance. Any second phase pinning particle added to a solutionized and aged aluminum system processed by AFSD would further manifest the quench sensitivity problems discussed above. A second solution would be leveraging process control. Flow stress can be related to mean subgrain diameter via the Derby relationship (Equation 7) [40].

$$\sigma = \frac{KGb}{D} \tag{7}$$

Where σ is the flow stress, K is a constant of ~10 for FCC crystals, b is the burgers vector, and D is the mean subgrain diameter. From this relationship, we can see that manipulating the flow

stress experienced by the material will change the subgrain diameter. Through process parameter manipulation (i.e., temperature control, RPM variation, traverse rate), the flow stress and temperature can be manipulated to achieve a larger subgrain size. This larger subgrain size will decrease the driving force for normal grain growth shown in Equation 4. While it is outside the scope of work for this study, there may be processing conditions that avoid abnormal grain growth for the conventional AA7050.

Secondary Phase Formation

Throughout this study there were a multitude of regions studied with both EDS and EDX that had chemical compositions outside the anticipated phases present in AA7050. Manuscript 2. Figure 4 shows the possible presence of θ after deposition and post-deposition heat treatment. Manuscript 2. Figure 14 and Manuscript 2. Figure 19 show possible evidence of θ observed in EDX scans. It was outside the scope of work of this experiment to understand the possibility of inducing secondary phases via AFSD, but the topic deserves further experimentation. Shear segregation of solute elements during the severe plastic deformation may create localized regions in which Cu and Al are able to react and form the binary θ-phase. This type of reaction would require extensive characterization to understand its mechanism, but the formation of a high temperature phase would be detrimental to the ability to undergo proper solutionizing and aging. Furthermore, the Cu within the Al matrix plays a critical role in precipitation kinetics and corrosion characteristics in the T7 temper this alloy is typically found in. The formation of binary Al-Cu phases that would use up available solute may change the way the alloy performs after deposition and heat treatment.

Conclusions and Future Work

Additive Friction Stir Deposition was utilized to deposit AA7050 with and without Zr dispersoid particles with featureless and protrusion tools. Mechanical performance and quench sensitivity were evaluated by intentionally causing heterogeneous precipitation and evaluating the loss of yield strength between water quenched and air-cooled specimens. Advanced characterization was conducted via SEM, EBSD, and HAADF to evaluate the resulting microstructure, texture, and precipitate structure in the as-printed, AFSD-T73-AC, and AFSD-T73-WQ conditions. The following points highlight the results.

- AFSD significantly increased the quench sensitivity of AA7050 in post-deposition thermal treatment. This was attributed to the loss of coherency of the Al_3Zr dispersoid particle contributing to heterogeneous precipitation.
- The removal of Zr from the alloy chemistry significantly reduced the quench sensitivity for the case of the featureless tool.
- The as-printed microstructure between conventional AA7050 and Zr-free AA7050 show similarities for both the featureless and protrusion tool.
- The featureless prints were more textured and more consistent throughout the build and showed more shear vertically through the layer height than the protrusion tool. The protrusion tool showed evidence of more lateral shear.

    - The featureless prints show evidence of shear heterogeneities at the layer-to-layer interfaces.

- After post-deposition heat treatment all Zr-free samples show signs of significant abnormal grain growth. In the as-received AA7050 processed with protrusions, abnormal grain growth occurs in regions with small grain sizes. Further process development may be able to stabilize the grain structure of the conventional AA7050 via managing the flow stress.

This work was successful in identifying a potential pitfall of utilizing AFSD for producing large-scale components out of AA7050. While it appears that AFSD of conventional AA7050 is not viable, switching the alloy chemistry to avoid the increased quench sensitivity may be useful in applications where the enlarged grain structure is acceptable. Future work must be conducted to further understand the mechanism for retaining small grains at the layer-to-layer interface in the featureless prints.

Manuscript 2 References

[1] E. A. Starke and J. T. Staley, "Application of modern aluminium alloys to aircraft," in *Fundamentals of Aluminium Metallurgy: Production, Processing and Applications*, Elsevier Ltd., 2010, pp. 747–783. doi: 10.1533/9780857090256.3.747.

[2] R. S. Mishra and M. Komarasamy, "Physical Metallurgy of 7XXX Alloys," in *Friction Stir Welding of High Strength 7XXX Aluminum Alloys*, Elsevier, 2016, pp. 5–14. doi: 10.1016/b978-0-12-809465-5.00002-7.

[3] K. K. Sankaran and R. S. Mishra, "Aluminum Alloys," in *Metallurgy and Design of Alloys with Hierarchical Microstructures*, Elsevier, 2017, pp. 57–176. doi: 10.1016/B978-0-12-812068-2.00004-7.

[4] Y. Zhang, "Quench Sensitivity of 7xxx Series Aluminium Alloys," 2014.

[5] B. L. Ou, J. G. Yang, and M. Y. Wei, "Effect of homogenization and aging treatment on mechanical properties and stress-corrosion cracking of 7050 alloys," *Metall Mater Trans A Phys Metall Mater Sci*, vol. 38, no. 8, pp. 1760–1773, Aug. 2007, doi: 10.1007/s11661-007-9200-z.

[6] M. Schöbel, P. Pongratz, and H. P. Degischer, "Coherency loss of Al 3(Sc,Zr) precipitates by deformation of an Al-Zn-Mg alloy," *Acta Mater*, vol. 60, no. 10, pp. 4247–4254, Jun. 2012, doi: 10.1016/j.actamat.2012.04.011.

[7] Y. Sun, X. Bai, D. Klenosky, K. Trumble, and D. Johnson, "A Study on Peripheral Grain Structure Evolution of an AA7050 Aluminum Alloy with a Laboratory-Scale Extrusion Setup," *J Mater Eng Perform*, vol. 28, no. 8, pp. 5156–5164, Aug. 2019, doi: 10.1007/s11665-019-04208-7.

[8] T. Ram Prabhu, "An overview of high-performance aircraft structural al alloy-AA7085," *Acta Metallurgica Sinica (English Letters)*, vol. 28, no. 7. Chinese Society of Metals, pp. 909–921, Jul. 01, 2015. doi: 10.1007/s40195-015-0275-z.

[9] M. Dixit, R. S. Mishra, and K. K. Sankaran, "Structure-property correlations in Al 7050 and Al 7055 high-strength aluminum alloys," *Materials Science and Engineering A*, vol. 478, no. 1–2, pp. 163–172, Apr. 2008, doi: 10.1016/j.msea.2007.05.116.

[10] X. Fang *et al.*, "Effects of Cu and Al on the crystal structure and composition of η (MgZn 2) phase in over-aged Al-Zn-Mg-Cu alloys," *J Mater Sci*, vol. 47, no. 14, pp. 5419–5427, Jul. 2012, doi: 10.1007/s10853-012-6428-9.

[11] A. Deschamps, Y. Bréchet, and F. Livet, "Influence of copper addition on precipitation kinetics and hardening in Al-Zn-Mg alloy," *Materials Science and Technology*, vol. 15, no. 9, pp. 993–1000, 1999, doi: 10.1179/026708399101506832.

[12] R. S. Mishra and H. Sidhar, "Physical Metallurgy of 2XXX Aluminum Alloys," in *Friction Stir Welding of 2XXX Aluminum Alloys Including Al-Li Alloys*, Elsevier, 2017, pp. 15–36. doi: 10.1016/b978-0-12-805368-3.00002-9.

[13] T. Qi, H. Zhu, H. Zhang, J. Yin, L. Ke, and X. Zeng, “Selective laser melting of Al7050 powder: Melting mode transition and comparison of the characteristics between the keyhole and conduction mode,” *Mater Des*, vol. 135, pp. 257–266, Dec. 2017, doi: 10.1016/j.matdes.2017.09.014.

[14] N. T. Aboulkhair, M. Simonelli, L. Parry, I. Ashcroft, C. Tuck, and R. Hague, “3D printing of Aluminium alloys: Additive Manufacturing of Aluminium alloys using selective laser melting,” *Progress in Materials Science*, vol. 106. Elsevier Ltd, Dec. 01, 2019. doi: 10.1016/j.pmatsci.2019.100578.

[15] S. C. Altıparmak, V. A. Yardley, Z. Shi, and J. Lin, “Challenges in additive manufacturing of high-strength aluminium alloys and current developments in hybrid additive manufacturing,” *International Journal of Lightweight Materials and Manufacture*, vol. 4, no. 2. KeAi Publishing Communications Ltd., pp. 246–261, Jun. 01, 2021. doi: 10.1016/j.ijlmm.2020.12.004.

[16] T. D. Ngo, A. Kashani, G. Imbalzano, K. T. Q. Nguyen, and D. Hui, “Additive manufacturing (3D printing): A review of materials, methods, applications and challenges,” *Composites Part B: Engineering*, vol. 143. Elsevier Ltd, pp. 172–196, Jun. 15, 2018. doi: 10.1016/j.compositesb.2018.02.012.

[17] J. H. Martin, B. D. Yahata, J. M. Hundley, J. A. Mayer, T. A. Schaedler, and T. M. Pollock, “3D printing of high-strength aluminium alloys,” *Nature*, vol. 549, no. 7672, pp. 365–369, Sep. 2017, doi: 10.1038/nature23894.

[18] M. Sokoluk, C. Cao, S. Pan, and X. Li, “Nanoparticle-enabled phase control for arc welding of unweldable aluminum alloy 7075,” *Nat Commun*, vol. 10, no. 1, Dec. 2019, doi: 10.1038/s41467-018-07989-y.

[19] Z. Lei, J. Bi, Y. Chen, X. Chen, X. Qin, and Z. Tian, “Effect of energy density on formability, microstructure and micro-hardness of selective laser melted Sc- and Zr-modified 7075 aluminum alloy,” *Powder Technol*, vol. 356, pp. 594–606, Nov. 2019, doi: 10.1016/j.powtec.2019.08.082.

[20] R. S. Mishra, R. S. Haridas, and P. Agrawal, “Friction stir-based additive manufacturing,” *Science and Technology of Welding and Joining*, vol. 27, no. 3. Taylor and Francis Ltd., pp. 141–165, 2022. doi: 10.1080/13621718.2022.2027663.

[21] H. Z. Yu and R. S. Mishra, “Additive friction stir deposition: a deformation processing route to metal additive manufacturing,” *Mater Res Lett*, vol. 9, no. 2, pp. 71–83, Feb. 2021, doi: 10.1080/21663831.2020.1847211.

[22] H. Z. Yu *et al.*, “Non-beam-based metal additive manufacturing enabled by additive friction stir deposition,” *Scr Mater*, vol. 153, pp. 122–130, Aug. 2018, doi: 10.1016/j.scriptamat.2018.03.025.

[23] D. Z. Avery *et al.*, “Influence of Grain Refinement and Microstructure on Fatigue Behavior for Solid-State Additively Manufactured Al-Zn-Mg-Cu Alloy,” *Metall Mater*

Trans A Phys Metall Mater Sci, vol. 51, no. 6, pp. 2778–2795, Jun. 2020, doi: 10.1007/s11661-020-05746-9.

[24] D. Z. Avery *et al.*, "Evaluation of Microstructure and Mechanical Properties of Al-Zn-Mg-Cu Alloy Repaired via Additive Friction Stir Deposition," *J Eng Mater Technol*, vol. 144, no. 3, Jul. 2022, doi: 10.1115/1.4052816.

[25] G. G. Stubblefield *et al.*, "Ballistic Evaluation of Aluminum Alloy (AA) 7075 Plate Repaired by Additive Friction Stir Deposition Using AA7075 Feedstock," *Journal of Dynamic Behavior of Materials*, vol. 9, no. 1, pp. 79–89, Mar. 2023, doi: 10.1007/s40870-022-00363-6.

[26] C. J. T. Mason *et al.*, "Process-structure-property relations for as-deposited solid-state additively manufactured high-strength aluminum alloy," *Addit Manuf*, vol. 40, Apr. 2021, doi: 10.1016/j.addma.2021.101879.

[27] J. K. Yoder, R. J. Griffiths, and H. Z. Yu, "Deformation-based additive manufacturing of 7075 aluminum with wrought-like mechanical properties," *Mater Des*, vol. 198, Jan. 2021, doi: 10.1016/j.matdes.2020.109288.

[28] M. C. Wells, "Mechanical and Physical Properties of Additive Friction Stir Deposited Aluminum," Virginia Tech, Blacksburg, 2022.

[29] N. Gotawala and H. Z. Yu, "Material flow path and extreme thermomechanical processing history during additive friction stir deposition," *J Manuf Process*, vol. 101, pp. 114–127, Sep. 2023, doi: 10.1016/J.JMAPRO.2023.05.095.

[30] M. E. J. Perry *et al.*, "Tracing plastic deformation path and concurrent grain refinement during additive friction stir deposition," *Materialia (Oxf)*, vol. 18, Aug. 2021, doi: 10.1016/j.mtla.2021.101159.

[31] M. E. J. Perry, R. J. Griffiths, D. Garcia, J. M. Sietins, Y. Zhu, and H. Z. Yu, "Morphological and microstructural investigation of the non-planar interface formed in solid-state metal additive manufacturing by additive friction stir deposition," *Addit Manuf*, vol. 35, Oct. 2020, doi: 10.1016/j.addma.2020.101293.

[32] "Designation: E8/E8M − 21 Standard Test Methods for Tension Testing of Metallic Materials 1", doi: 10.1520/E0008_E0008M-21.

[33] "International Alloy Designations and Chemical Composition Limits for Wrought Aluminum and Wrought Aluminum Alloys Use of the Information," Arlington, Aug. 2018. [Online]. Available: www.aluminum.org

[34] R. J. Griffiths *et al.*, "Solid-state additive manufacturing of aluminum and copper using additive friction stir deposition: Process-microstructure linkages," *Materialia (Oxf)*, vol. 15, Mar. 2021, doi: 10.1016/j.mtla.2020.100967.

[35] R. W. Fonda and K. E. Knipling, “Texture development in friction stir welds,” *Science and Technology of Welding and Joining*, vol. 16, no. 4, pp. 288–294, May 2011, doi: 10.1179/1362171811Y.0000000010.

[36] C. Zhang and L. S. Toth, “Polycrystal simulation of texture-induced grain coarsening during severe plastic deformation,” *Materials*, vol. 13, no. 24, pp. 1–16, Dec. 2020, doi: 10.3390/ma13245834.

[37] J. K. Yoder, “Origins of Embrittlement of an Al-Zn-Mg-Cu Alloy Post Additive Friction Stir Deposition,” Virginia Tech, Blacksburg, 2022.

[38] F. J. Humphreys, “A UNIFIED THEORY OF RECOVERY, RECRYSTALLIZATION AND GRAIN GROWTH, BASED ON THE STABILITY AND GROWTH OF CELLULAR MICROSTRUCTURES-II. THE EFFECT OF SECOND-PHASE PARTICLES,” Acta Metallurgica Inc, 1997.

[39] P. A. Manohar and F. Chandra, “Review Five Decades of the Zener Equation,” 1998.

[40] F. J. Humphreys and M. Hatherly, “RECRYSTALLIZATION AND RELATED ANNEALING PHENOMENA,” 2004. [Online]. Available: http://www.elsevier.com

[41] C. Vargel, *Corrosion of Aluminum*. Elsevier, 2004.

Chapter 4: Solid-State Repair

4.1. Manuscript 3: Solid-State Structural Repair of Corroded Fastener Holes in High Strength Aluminum Via Additive Friction Stir Deposition

Greg D. Hahn[1], Kendall P. Knight[1], R. Joey Griffiths[2], David Garcia[3], Anand Karuppiah[4], Nam D. Pham[5], Jim Lua[4], Hang Z. Yu[1*]

[1]Department of Materials Science and Engineering, Virginia Tech, Blacksburg, VA 24061, USA.

[2]Lawrence Livermore National Laboratory, Livermore, CA 94550, USA.

[3]Pacific Northwest National Laboratory, Richland, WA 99354, USA

[4]Global Engineering Materials, Inc., Princeton, NJ 08540, USA.

[5]Airframe Technology Branch, Structures Division Naval Air Warfare Center Aircraft Division, Paxtuxent, MD 20670, USA.

[*]Corresponding author: hangyu@vt.edu

Abstract

Additive Friction Stir Deposition was utilized to carry repairs of simulated corroded AA7050-T7451 through holes. Repaired coupons outperformed baseline material in fatigue for both R=0.1 and R=-1 loading conditions, with R=0.1 loading outperforming pristine material. Advanced characterization was conducted into the microstructure and crack initiation mechanisms, and it was found that the high shear nature of AFSD reduced the size of Fe-rich constituent particles that provided crack initiation sites in the base material. After AFSD, the smaller spherodized particles did not cause crack initiation, which was instead caused by overgrown $MgZn_2$ η-phase precipitates. Different regions of the repair were identified and characterized, and it was found that regions that experienced intense thermomechanical mixing had preferential η-phase precipitates form on Al_3Zr dispersoid particles. This leaves potential further room for fatigue performance improvement and opens the door for improving component lifetime via AFSD.

Keywords: Fatigue, Structural Repair, Constituent Particle, Coherency, Dispersoid Particle

Introduction

High strength aluminum alloys, primarily the 2xxx and 7xxx series alloys are the common materials used for structural components in modern aircraft. This work focuses on AA7050, renowned for its strength, fatigue life, and lower quench sensitivity compared to its predecessor Al7075 [1], [2]. The lower quench sensitivity of AA7050 allows for more complex and thicker wrought products to be produced with the anticipated strength observed in thinner sections. This improvement to the 7xxx series aluminum system is achieved by changing the dispersoid particle composition. Al7075 utilizes a chromium rich dispersoid particle that forms with incoherent interfaces with the Al matrix; AA7050 on the other hand utilizes a zirconium

rich dispersoid particle that forms in an $L1_2$ structure lending coherent interfaces [1], [2]. These coherent interfaces don't as readily serve as heterogeneous nucleation sites when quenching and allow for thicker sections to achieve full strength. The alloys utilize the same $MgZn_2$ η-phase precipitate structure to impede dislocations and provide strength to the matrix.

With the increased complexity of components used in the aerospace and defense industries, there is a growing need for repairing existing components as opposed to replacing them. The aerospace forging market is a $28B/year market plagued by long lead times [3], [4]. It has been reported that lead times for new forgings can be up to 39 weeks, and up to 15 weeks for replacement components [4]. This problem is exacerbated by the prolific corrosion that can plague forgings exposed to corrosive environments; in the case of the United States Navy, this can cost up to $6B/year [5]. This work will focus on a specific application in need of a repair, corroded aerostructure fastener holes. In the case of large airframes, corroded fastener holes can lead to a part failing inspection; in some cases, dramatically reducing the lifetime of the aircraft. Traditional repair of a corroded fastener hole involves drilling the hole out to a larger size and inserting a metallic bushing to bring the hole back to size. Bushing repairs are effective, but the lack of metallic bonding between the bushing and parent hole material reduces the strength of the component. In this work, we propose the use of a solid-state repair that allows for redrilling the original hole size.

Additive Friction Stir Deposition (AFSD) is an emerging solid-state additive manufacturing technique that leverages plastic flow and shear to deform and deposit metals [6], [7]. The solid-state nature of AFSD is paramount for the high strength 7xxx series Al alloys which are plagued by hot-cracking during melt based processes [8]–[11]. Previous work has shown that AFSD is capable of filling holes in Al7075 and separately has been shown to restore Al7075 to full strength after printing [12]–[14]. Further work has been conducted in understanding the viability of repairing Al7075 components via AFSD [15], [16]. It has also been shown that AFSD can repair corroded hole walls applying both a geometric and structural repair [Joey paper]. This work expands on these results, exploring the mechanism responsible for the improved fatigue life.

Materials and Methods

Materials and Manufacturing

The feed material and substrate were both aluminum 7050-T7451 plate that was obtained from Tri-Tech Metals (Rancho Cucamonga, CA, USA). The substrates were machined from 76.2 mm x 152.4 mm x 6.35 mm rolled plate with the long direction corresponding to the rolling direction. The center of the substrate was machined to a thickness of 4.0 mm and a 7.9375 mm hole was drilled in the center. A technical drawing for the substrate configuration is shown in Manuscript 3. Appendix A. Feed rods were 152.4 mm x 9.525 mm x 9.525 square rods cut parallel to the rolling direction of 9.525 mm thick plate.

Additive Friction Stir Deposition was carried out on a MELD R2 system (MELD Manufacturing, Christiansburg VA, USA). The substrates were clamped onto a fixture plate with a 1.27mm x 25.4mm x 76.2 mm shim underneath the gauge region centered on the hole with the long direction of the shim perpendicular to the long direction of the coupon. The sides of the

feed rods were sprayed with a graphite lubricant before being inserted into the hollow tool of the MELD system. For all prints, a tool with four 2.29mm high teardrop features in the face was used. A CAD rendering of the teardrop featured tool is shown in **Manuscript 3. Figure 24**A. **Manuscript 3. Figure 24**B shows the scale of an AFSD tool compared to the 6.35 and 7.9375 holes in the substrate and test coupon. To conduct the repairs a proprietary repair process was utilized which promotes material mixing between the hole and the material being deposited.

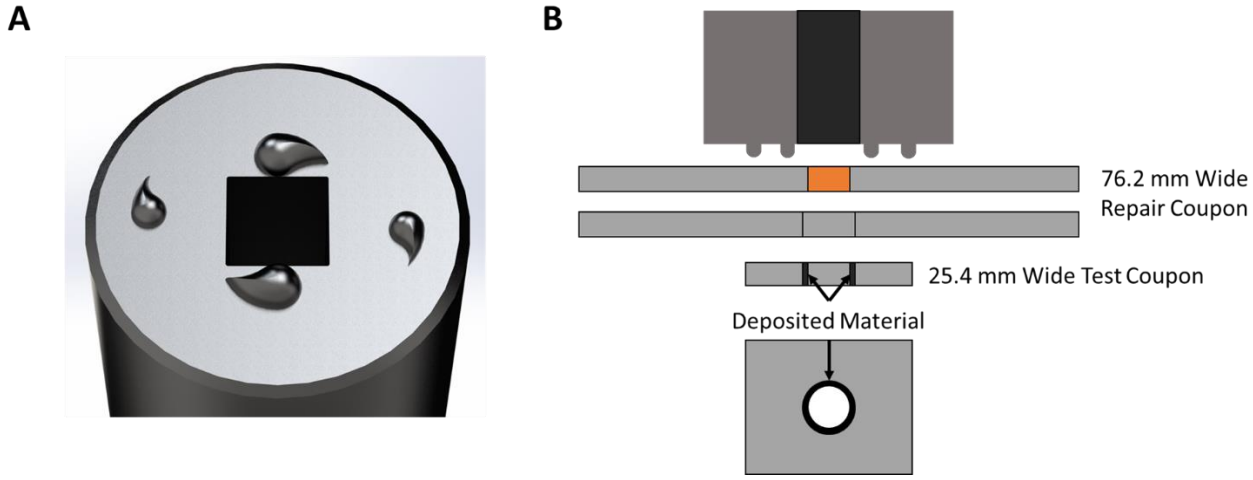

Manuscript 3. Figure 24: (A) Rendering of teardrop protrusion tool face (B) To-scale schematic of tool and coupon configurations.

After deposition, samples were machined into their final configuration with a 6.35 mm hole drilled in the center. A technical drawing of the final testing configuration for the 6.35mm hole is shown in Manuscript 3. Appendix B. Three different mechanical testing coupons were studied; a 5/16” (7.9375 mm) hole baseline from pristine AA7050-T7451 plate, a 1/4" (6.35 mm) hole baseline from pristine AA7050-T7451 plate, and finally an AFSD repaired 5/16” hole that has been drilled back to a 1/4" hole. All holes produced and tested in fatigue were reamed to their final geometry with a nominal reamer. These samples will be referred to as 5/16” Baseline, 1/4" Baseline, and 1/4” Repair respectively.

Characterization Methods

Microstructural Characterization

A microstructural cross section was cut perpendicular to the loading direction from a repaired and machined coupon before the hole drilling operation. The cross section was mechanically polished with 1000 grit sandpaper then electropolished. The electropolishing was performed with a liquid nitrogen cooled electrolyte (70% methanol and 30% nitric acid) at 30V in ten second intervals. Optical microscopy was carried out on a Keyence VHX-7000 (Osaka, Japan) digital microscope. Electron backscatter diffraction was carried using a Zeiss LEO 1550 (Wetzlar, Germany) field-emission scanning electron microscope (SEM) with an Oxford Nordlys (Abingdon, England) detector. Regions of interest were then determined, and transmission electron microscopy (TEM) foils were prepared via focused ion beam using a Helios UC G4 Dual Beam FIB-SEM (Sarasota FL, USA). TEM characterization was carried out via a Themis

60-300kV Transmission Electron Microscope (Thermo Fisher, Waltham MA, USA). Fracture surfaces were inspected using a JEOL IT-500HR (Tokyo, Japan) SEM.

Mechanical Testing

Fatigue specimens were polished parallel to the loading direction with SiC polishing stones and a 4:1 mixture of WD-40® and Marvel Mystery Oil®. All surfaces were first polished with a 220-grit stone, then the gauge section was polished with a 400-grit stone. Care was given not to disturb the edge of the hole in the gauge section.

Force controlled fatigue testing was conducted on an MTS 810 with a 50kN load cell (Eden Prairie, MN, USA) at two different loading conditions. A full tension-compression loading condition was studied at an R=-1 loading condition, while a tension-tension condition was studied at R=0.1. Loading conditions were established by testing 5/16" Baseline coupons with the goal of failing at approximately 10,000 cycles. To maintain consistency with the applied stress level, the coupons were measured in thickness and width and load was varied to maintain the same nominal cross-sectional stress on the gauge area. After an appropriate load was determined, 1/4" Baseline and 1/4" Repair samples were tested to the same loading condition. All fatigue tests were conducted at 5 Hz and force and crosshead displacement data were collected at 101 Hz.

Finite Element Analysis

Four finite element analyses were carried out using geometries with both 5/16" and 1/4" holes loaded in R=-1 and R=0.1 to understand the stress state on the hole wall. These simulations were loaded in tension with the same force as applied by the fatigue frame for both the R=-1 and R=0.1 loading conditions. This resulted in a 12.99kN load for the two R=-1 coupons and a 20.14kN load for the R=0.1 coupons. These analyses were meant to emulate the first fatigue stroke of the baseline condition samples rather than repairs, so an elastic-plastic material model was used with data coming from a tensile test of the plate the coupons were cut from. These simulations were carried out in Abaqus (Dassault Systemes, France) using ~120k C3D8R brick elements. Both the von-mises stress and plastic equivalent strain are reported.

Results

Fatigue Results

To consistently fail the 5/16" Baseline coupon at approximately 10,000 cycles, the peak load had to be determined for both loading conditions. The peak load established for the R=-1 loading case was 12.99 kN, while the R=0.1 loading case was 20.14 kN. Fatigue testing of the 1/4" Baseline and 1/4" Repair were conducted at the same loading conditions. The results were plotted in a Weibull distribution by assigning a statistical lifetime. The lifetimes of each geometry were sorted from lowest to highest and assigned a position(i), the total number of tests conducted for the geometry was assigned n. The statistical lifetime (L_i) was assigned by solving $L_i = \frac{i}{n+1}$ The cycles to failure versus statistical lifetime is plotted in Manuscript 3. **Figure 25**. Using this approach, the (std or variance) is equivalent to the slope of the data and deviations from linear indicate a non-gaussian distribution. Using a linear least-squares fit, the 60% lifetime for each geometry at each loading condition can be determined. For the R=-1 loading condition the 1/4" Repair samples fall between the 5/16" Baseline and 1/4" Baseline. This

demonstrates that the 1/4” Repair is improving the fatigue performance as compared to the 5/16” Baseline but is not outperforming the pristine coupon geometry. For the R=0.1 loading condition, the 1/4” Repair outperforms both the 5/16” and 1/4” Baseline geometries. The slope of the 1/4” Repair linear fit is also more positive than that of the 5/16” and 1/4” Baseline respectively, indicating the 1/4” Repair has more variance in the fatigue life. The maximum and minimum loading as well as the 60% lifetimes both the loading conditions and all the geometries are shown in **Manuscript 3. Table 3**.

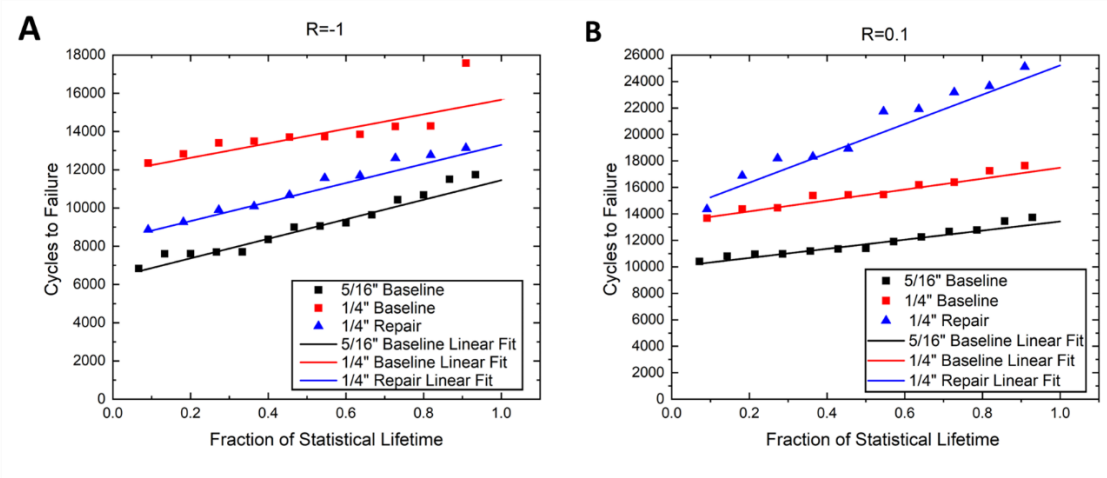

Manuscript 3. Figure 25: Fatigue Test Results for 1/4" Baseline, 5/16” Baseline, and 1/4" Repair. (A) For R=-1 loading condition. (B) For R=0.1 loading condition.

Manuscript 3. Table 3: Fatigue Testing Results

R Ratio	Max Load (kN)	Min Load (kN)	5/16” Baseline 60% Lifetime	1/4” Baseline 60% Lifetime	1/4” Repair 60% Lifetime
R=-1	12.99	-12.99	9,409	14,141	11,307
R=0.1	20.14	2.01	12,049	15,836	20,786

FEA Analysis

To understand the stress state surrounding the hole in the baseline geometries finite element analysis was performed. The Von Mises stress for the 5/16” Baseline geometry is shown for the R=-1 max loading condition (12.99 kN) in Manuscript 3. **Figure 26**A. The R=0.1 max loading condition of 20.1 kN is shown in Manuscript 3. **Figure 26**B. The maximum stress for R=-1 is 403 MPa, while in the R=0.1 case the stress reaches 480 MPa. This induces localized yielding on the inside of the 5/16” hole and is shown with equivalent strain in Manuscript 3. **Figure 26**C. The maximum equivalent strain is 0.0007 for the 5/16” Baseline at the 20.1 kN load.

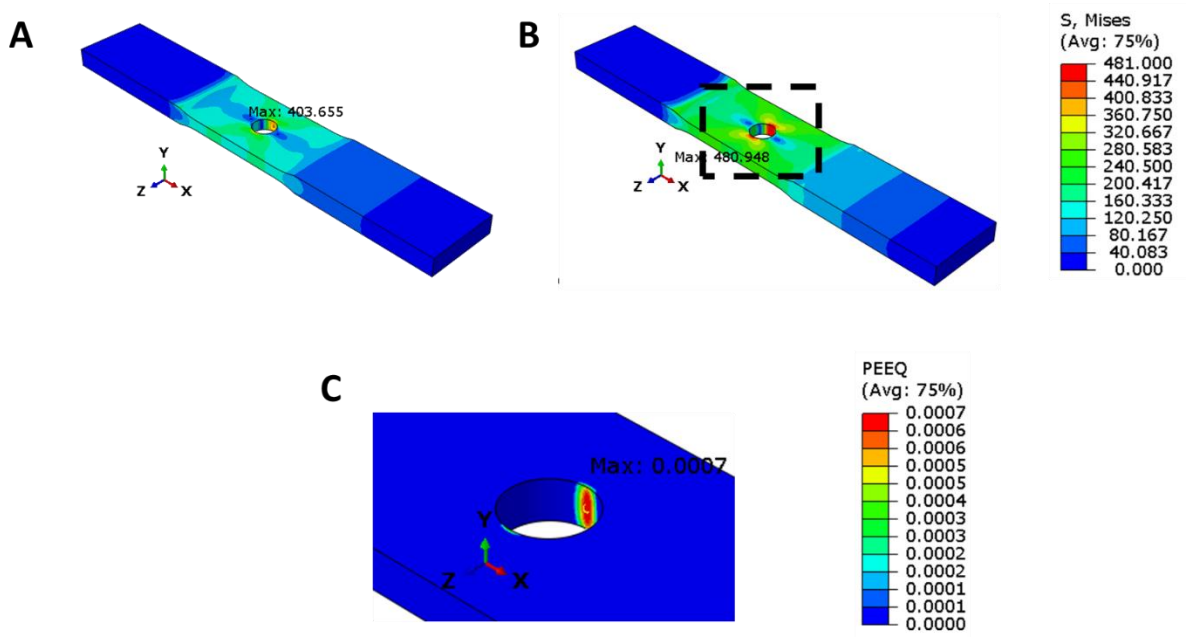

Manuscript 3. Figure 26: FEA analysis of 5/16" Baseline coupon. (A) With maximum tensile load of R=-1 loading. (B) With maximum tensile load of R=0.1 loading. (C) Showing equivalent plastic strain in the R=0.1 loading condition.

A similar FEA study was conducted for the 1/4" Baseline coupon. The resulting Von Misses stress distributions are shown in Manuscript 3. **Figure 27**. The R=-1 loading condition has a maximum stress of 391 MPa while the R=0.1 condition has a stress of 478 MPa. The higher stress in the R=0.1 loading condition again induces plasticity in the inside of the 1/4" hole wall. The plasticity is highly localized to the inside of the hole wall and is shown in Manuscript 3. **Figure 27**C, with a maximum equivalent strain of 0.005.

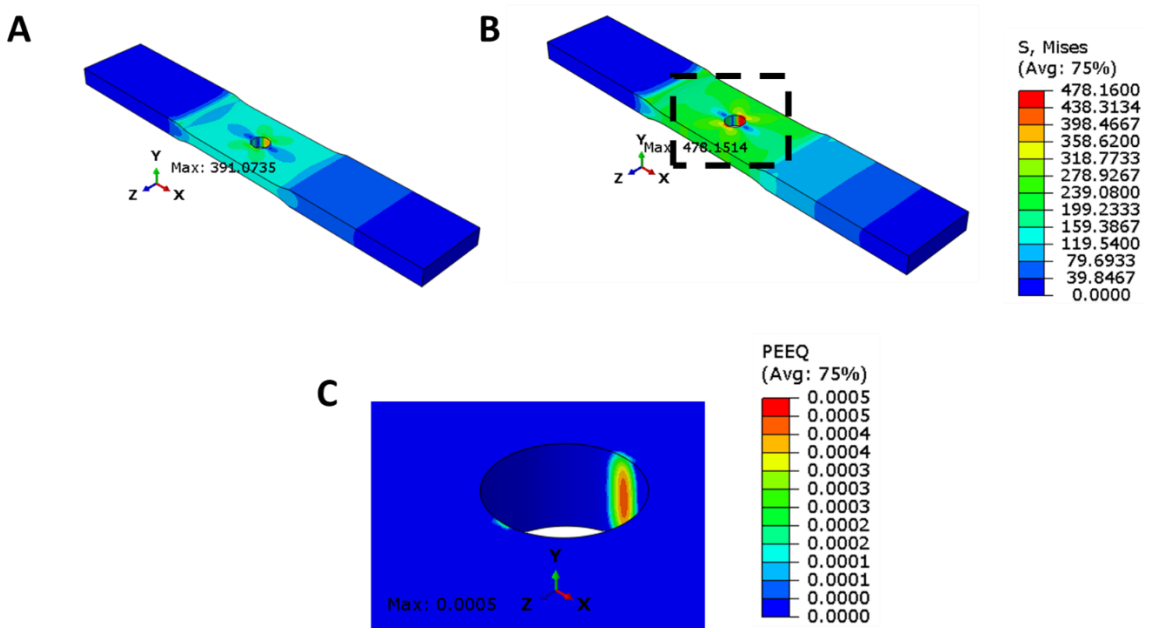

Manuscript 3. Figure 27: FEA analysis of 1/4" Baseline coupon. (A) With maximum tensile load of R=-1 loading. With maximum tensile load of R=0.1 loading. (C) Showing equivalent plastic strain in the R=0.1 loading condition.

Microstructural Characterization

To understand the microstructural effects of the thermomechanical process, a cross section from a repaired coupon was taken perpendicular to the intended loading direction. An optical stitched image of the cross section can be seen in Manuscript 3. Figure 28. The prior 5/16" hole wall and intended 1/4" hole wall are overlaid. The cross section shows some distinct features, firstly is the wide, shallow bowl shape. This style of bowl corresponds to the recrystallized region and has been documented in FSW literature [17]–[20]. The recrystallized bowl fully penetrates through the thickness of the coupon indicating proper mixing through thickness. There are also regions of mixture between the recrystallized region and the thermo-mechanically affected zone (TMAZ). In this repair scenario these regions will become the new hole wall region, so proper bonding between deposited and substrate material is paramount. In the top right corner of the cross section there is another recrystallized zone, corresponding to the region that undergoes a pin interaction during the repair process.

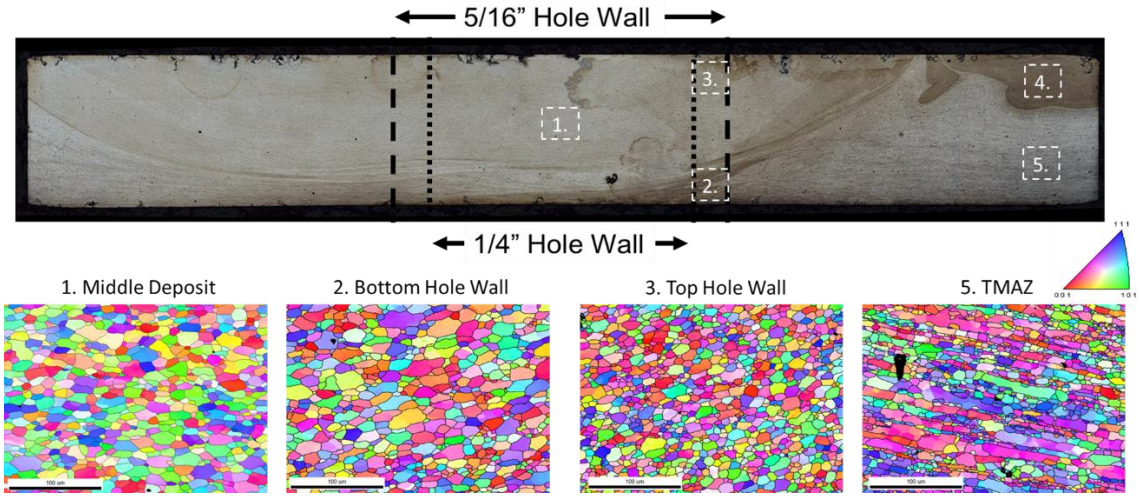

Manuscript 3. Figure 28: Stitched optical image of repaired cross section with overlaid hole wall locations and denoted regions of interest with corresponding IPF maps.

There are five main regions of focus for the microscopy to understand the different microstructures throughout the cross section. The first region is the “Deposit Zone”, this region exited the feed channel of the tool and plastically flowed into the middle of the hole. This material may or may not have experienced a pin interaction, depending on the time it exited the tool. The second region is the “Bottom Hole Wall”, this region lies between the previous 5/16” hole and where the new 1/4” hole will be drilled. From the stitched image, it appears that this region is a mixture of substrate and deposited material that has undergone dynamic recrystallization. The third region is the “Top Hole Wall”, this region lies between the 5/16” and 1/4” hole, but exists at the top of the sample, meaning it experienced multiple high strain rate events from the protrusions on the face of the tool. The fourth region is the “Pin Affected Zone”, this region is distinctly different from the stirred region within the repair bowl. This material experienced dynamic recrystallization from a severe high shear protrusion interaction. Lastly, is the “TMAZ”, this material has undergone a thermomechanical event, but is not fully recrystallized.

Deposit Zone

The Deposit Zone is characterized by sitting centrally within the repair bowl, within the region that will be removed in post-repair machining. This region will not be involved in the fatigue characteristics of a repair, but its microstructure lends insight into the thermomechanical history it experienced. An Inverse Pole Figure (IPF) image of the deposit region is shown in Manuscript 3. Figure 29A. It shows a recrystallized, equiaxed microstructure with an average grain size of 13 µm. Manuscript 3. Figure 29B shows a Kernel Average Misorientation (KAM) plot, showing evidence of subgrain structures within the recrystallized microstructure. This subgrain structure skews the misorientation distribution away from a Mackenzian distribution, indicating incomplete dynamic recrystallization.

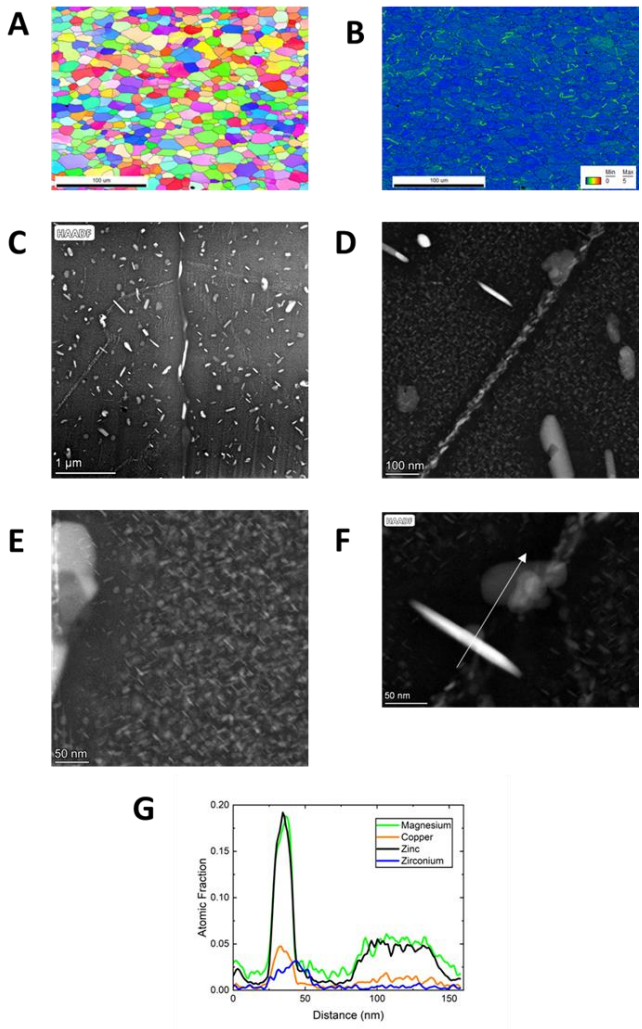

Manuscript 3. Figure 29: Deposit Zone microstructural characterization. (A) IPF. (B) KAM. (C) Low-magnification HAADF. (D) HAADF micrograph of grain boundary precipitation. (E) HAADF micrograph of precipitate free zones around large precipitates. (F) HAADF of subgrain boundary with overgrown precipitate and EDX line scan denoted. (G) Corresponding line scan shown in F.

Manuscript 3. Figure 29C shows a low magnification High Angle Annular Dark Field (HAADF) TEM image of the deposit region. It shows evidence of grain boundary precipitation as well as overgrown precipitates within the grain interior. The extent of the grain boundary precipitation is shown in Manuscript 3. Figure 29D, where a near continuous region of grain boundary precipitation is shown. This microstructure and large Precipitate Free Zones (PFZs) around the grain boundary correspond to lower overall strength due to inadequate solute within the matrix. There are also large precipitates evident within the grain interior in Manuscript 3. Figure 29D, these precipitates are possible sites of heterogeneous nucleation during cooling from printing. The large precipitates are shown in further detail in Manuscript 3. Figure 29F, where an Energy Dispersive X-Ray Spectroscopy (EDX) line scan was taken across the particle. The results of the line scan are shown in Manuscript 3. Figure 29G, the large second phase particle is

rich in magnesium and zinc, with an increased amount of copper compared to the matrix. There is also an increase in the amount of zirconium towards the end of the substantial peak. The large particle most likely corresponds to the $MgZn_2$ η-phase with dissolved copper. The zirconium is most likely the Al_3Zr dispersoid particle, it appears that the dispersoid particle is providing a heterogeneous nucleation site during cooling. Manuscript 3. Figure 29E shows the length scale of the PFZs around a heterogeneous nucleation site ~50 nm, and the precipitation within the bulk of the matrix. Within the matrix there appears to be a fine dispersion of small $MgZn_2$ strengthening precipitates.

Bottom Hole Wall

The Bottom Hole Wall is characterized by sitting in the region that will become the 1/4" hole wall after post deposition machining. This region is near the "repair bowl" and shows signs of mixing between deposited material and substrate material. Due to the vertical depth of this region, it does not experience a pin interaction during printing. Manuscript 3. Figure 30A shows an IPF map of the Bottom Hole Wall region, it shows an equiaxed microstructure with an average grain size of 14 μm. The KAM in Manuscript 3. Figure 30B shows grains mostly clear of subgrains, however large grains show signs of subgrain structures. This suggests dynamic recrystallization as the main recrystallization mechanism. The larger grains contain most of the dislocation substructures while the smaller grains correspond to lower strain energy.

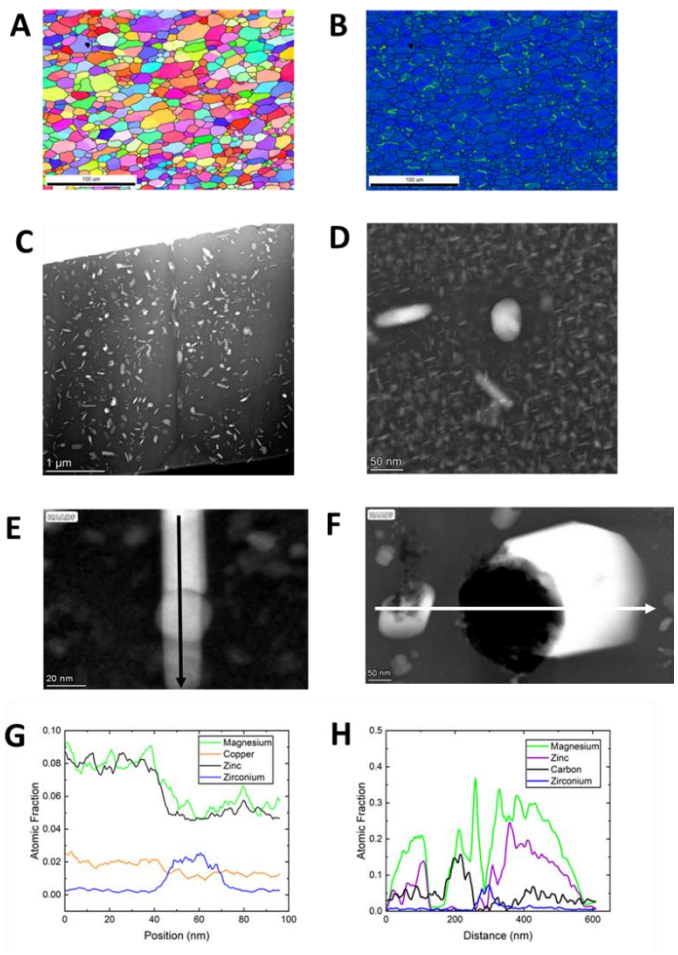

Manuscript 3. Figure 30: Bottom Hole Wall microstructural characterization. (A) IPF. (B) KAM. (C) Low-magnification HAADF. (D) Overgrown precipitates with matrix precipitates. (E) Overgrown precipitate on Zr dispersoid with EDX line scan. (F) Evidence of carbon contamination with EDX line scan. (G) Results of line scan shown in E. (H) Results of line scan shown in F.

Manuscript 3. Figure 30C shows a lower magnification HAADF image of the Bottom Hole Wall region, there is clear evidence of heterogeneous nucleation and grain boundary precipitation within this region. Compared to Manuscript 3. Figure 29C, this region has more instances of large second phase particles throughout the grain interior. Manuscript 3. Figure 30D shows regions of heterogeneous nucleation within the grain interior. These large second phase particles have PFZs directly adjacent to them, indicating a solute depleted region. Manuscript 3. Figure 30E shows an image of an overgrown $MgZn_2$ precipitate on a second phase particle with the line scan shown in Manuscript 3. Figure 30G. Like the Deposit Zone, there is evidence that the Al_3Zr dispersoid particles are providing a heterogeneous nucleation site for the η phase precipitates. Manuscript 3. Figure 30F shows evidence of carbon contamination within the Bottom Hole Wall Region. A line scan of this area is shown in Manuscript 3. Figure 30H, showing that the large black particle in Manuscript 3. Figure 30F is carbon, and it is providing a site for heterogeneous nucleation. This carbon most likely came from the graphite lubricant on

the feed material, and its presence in the Bottom Hole Wall corresponds to the high degree of mixing between the feed material and substrate in this region.

Top Hole Wall

The Top Hole Wall is located directly above the Bottom Hole Wall but sits near the top surface of the print. This region will become the corner of the hole wall after machining into the final test geometry. This region is clearly within the "repair bowl" of recrystallized material, and due to its proximity to the surface most likely saw a pin interaction during the printing process. An IPF map of this region is shown in Manuscript 3. Figure 31A, it shows a recrystallized microstructure with an average grain size of 10 µm. From the KAM plot in Manuscript 3. Figure 31B, there is still evidence of subgrain structures within the region.

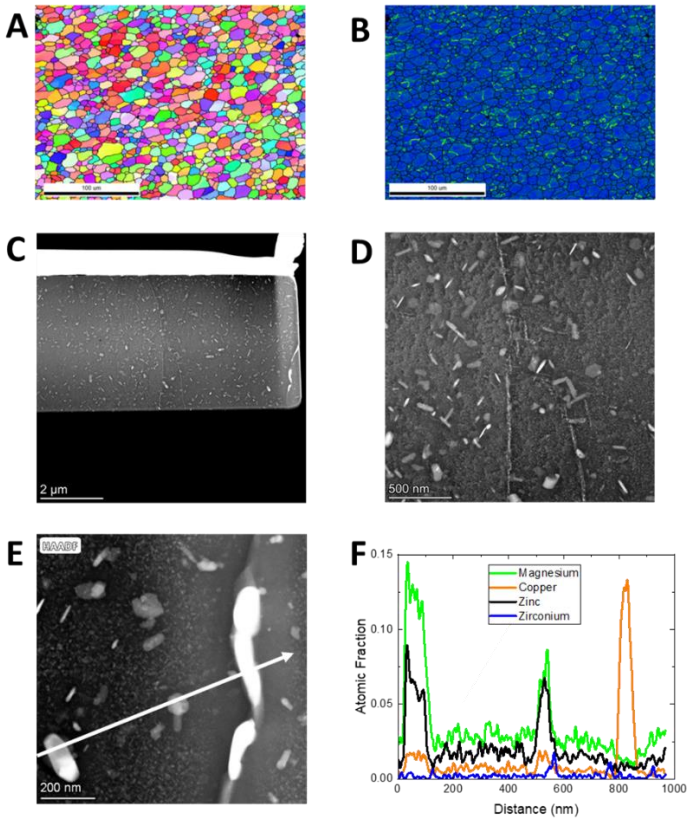

Manuscript 3. Figure 31: Top Hole Wall microstructural characterization. (A) IPF. (B) KAM. (C) Low-magnification HAADF. (D) HAADF micrograph with extensive overgrown precipitates. (E) Line scan region with grain boundary precipitation and large second phase particles in matrix. (F) Results of line scan shown in E.

The low magnification TEM image in Manuscript 3. Figure 31C shows a similar dispersion of large second phase particles. There is clear evidence of grain boundary precipitation shown in Manuscript 3. Figure 31D, with further evidence of heterogeneous nucleation within the grain interior. The grain boundaries within this region show nearly continuous precipitation. A grain boundary with a large second phase particle is shown in

Manuscript 3. Figure 31E, a line scan is overlaid capturing heterogeneous nucleation regions within the grain interior. The resulting line scan is shown in Manuscript 3. Figure 31F. The brighter regions of the HAADF image in Manuscript 3. Figure 31E correspond to copper segregation. This is observed in the large second phase particle in the bottom left of the image and the large second phase particle on the grain boundary. This is captured in the line scan data, with the large copper peak corresponding to the grain boundary area. The presence of copper on the grain boundary without a corresponding increase in magnesium suggests the presence of the high temperature θ-phase (Al_2Cu) as opposed to S-phase (Al_2CuMg). There is also a smaller second phase particle captured in the middle of the scan, corresponding to a zirconium peak. This again provides evidence that the Al_3Zr dispersoid particles are providing heterogeneous nucleation sites.

Pin Affected Zone

The Pin Affected Zone describes the region of material that experiences the intense thermomechanical pin event during printing. This region is distinguishable from optical microscopy in the top right corner of Manuscript 3. Figure 28. The two distinct zones present in Manuscript 3. Figure 28 correspond to the two radii of the two sets of pins. The region investigated during EBSD is the innermost of the two regions. An inverse pole figure map on the PAZ is shown in Manuscript 3. Figure 32A, it shows a fine equiaxed microstructure with an area averaged grain size of 7.6 µm. A kernel average misorientation plot is shown in Manuscript 3. Figure 32B showing some regions of subgrain networks within the region.

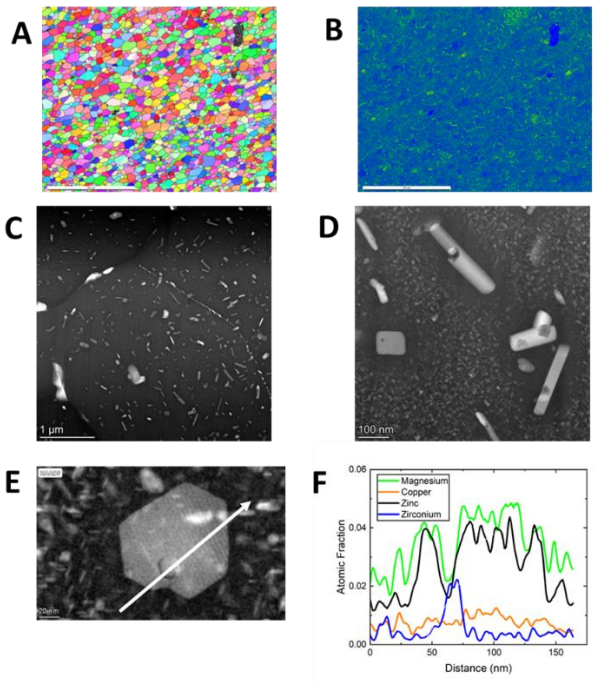

Manuscript 3. Figure 32: Pin Affected Zone microstructural characterization. (A) IPF (note scale bar is 100 µm). (B) KAM. (C) Low-magnification HAADF micrograph. (D) Large heterogeneous precipitates. (E) η-precipitate growing on Zr rich dispersoid particle. (F) Line scan results shown in E.

Manuscript 3. Figure 32C shows a low magnification TEM image of the Pin Affected Zone. There is evidence of grain boundary precipitation and copper segregation to the grain boundary in this region. The grain interior is scattered with overgrown precipitates. Manuscript 3. Figure 32D shows the extent of the heterogeneous nucleation more clearly, there is clear evidence that the overgrown precipitates are forming on a second phase particle. The PFZs around the precipitates are large in this region, on the order of 50 nm. A higher resolution HAADF of a precipitate is shown in Manuscript 3. Figure 32E. The precipitate is ~100 nm in width, and there is a second phase particle present within the precipitate. A line scan was conducted to determine the composition of the precipitate and the particle. This line scan is shown in Manuscript 3. Figure 32F, the precipitate is rich in zinc and magnesium, most likely $MgZn_2$. The smaller particle is rich in zirconium, most likely the Al_3Zr dispersoid particle.

Thermo-Mechanical Affected Zone

The TMAZ is distinctly different from the other regions characterized thus far. The TMAZ is not a fully recrystallized microstructure, it has not experienced the high strain events that caused full dynamic recrystallization in the other regions. This is exemplified in Manuscript 3. Figure 33A, the original rolled grains of the substrate material are still present. There are many smaller grains, possibly due to some degree of recrystallization from the thermo-mechanical process. The rolled grains show signs of subgrain structures in Manuscript 3. Figure 33B, pointing towards some degree of mechanical work during the AFSD repair. The smaller grains are free of subgrains, suggesting that the subgrains rotated into high angle grain boundaries. The misorientation angle distribution in this region is bimodal due to the incomplete recrystallization.

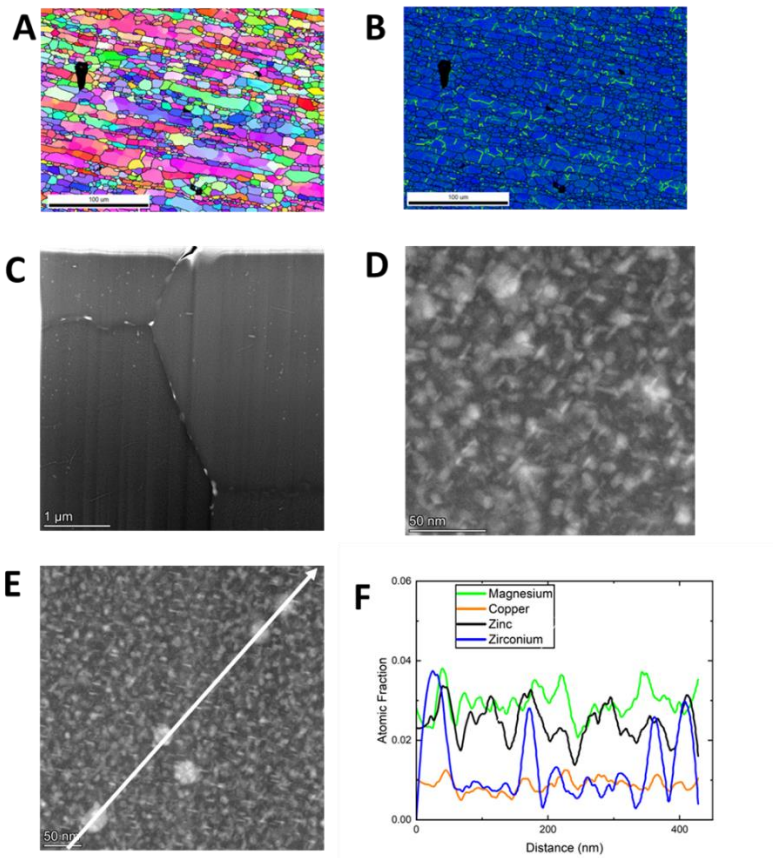

Manuscript 3. Figure 33: Thermomechanical Affected Zone microstructural characterization. (A) IPF. (B) KAM. (C) Low-magnification HAADF micrograph. (D) HAADF showing dense precipitation within the matrix. (E) Dispersoid particles showing no sign of heterogeneous precipitation. (F) Results of line scan shown in E.

Low magnification TEM images of the TMAZ region are distinctly different from the other regions. Comparing Manuscript 3. Figure 33C to Manuscript 3. Figure 29C, 7C, 8C, and 9C; it is evident that the degree of heterogeneous nucleation within grain interiors is drastically less in the TMAZ. There is some degree of grain boundary precipitation, but it is nowhere near the continuous distribution in the other regions. A representative image of the grain interiors in this region is shown in Manuscript 3. Figure 33D. There is a very fine, evenly dispersed precipitate structure. This lack of oversized second phase particles is related to the degree of recrystallization in this region. The grains that haven't undergone recrystallization haven't lost the coherency of the Al_3Zr dispersoid particles. Manuscript 3. Figure 33E shows an image with 5 Al_3Zr dispersoid particles visible, all of which have no evidence of heterogeneous nucleation. A line scan of the region is shown in Manuscript 3. Figure 33F capturing 4 of the dispersoid particles, showing the change in zirconium concentration has little effect on the other alloying elements.

Fracture Surface Characterization

Fracture surfaces of failed coupons were examined to understand the crack initiation mechanisms for the different samples. For ease of examination, R=0.1 samples were heavily investigated. The tension-compression nature of the R=-1 loading case disrupted the fracture surfaces making them harder to examine. A low magnification back-scatter micrograph of a 1/4" Baseline sample tested in the R=0.1 loading condition is shown in Manuscript 3. Figure 34A. The white box outlined in Manuscript 3. Figure 34A shows a region of interest shown in Figure 11b. It shows multiple crack initiation sites along the inside of the hole wall. The crack initiation sites correspond to bright clusters of particles, the outlined region in Manuscript 3. Figure 34B is shown in Manuscript 3. Figure 34C. At higher magnifications, the crack initiations are well correlated to the existence of these second phase particles. A cluster of second phase particles was analyzed via Electron Dispersive Spectroscopy (EDS), this is shown in Manuscript 3. Figure 34E-G. The second phase particles are rich in iron and copper, most likely corresponding to the Al_7Cu_2Fe constituent particle. The constituent clusters present on the fracture surface range in size from approximately 5 µm to 30 µm. Manuscript 3. Figure 34D shows a region of crack growth outline in black in Manuscript 3. Figure 34A. There are clear crack growth striations and constituent particles present on the fracture surface.

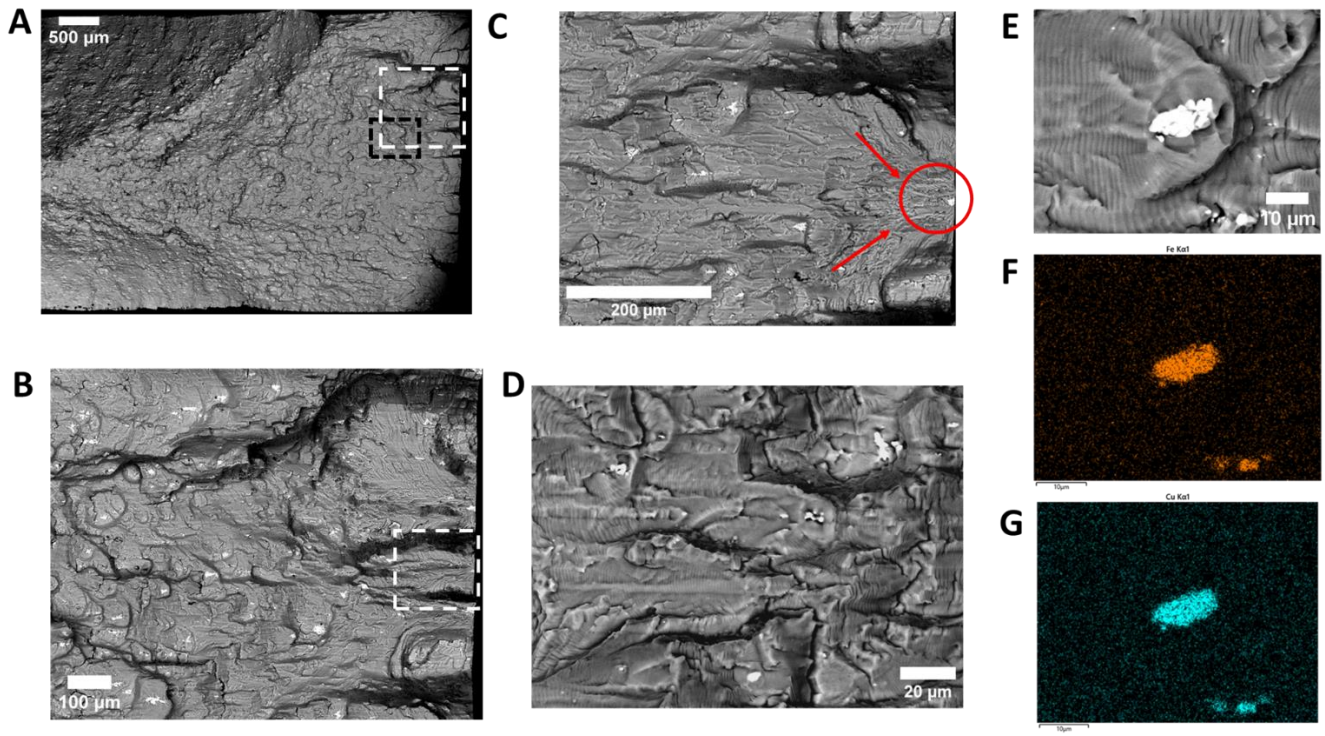

Manuscript 3. Figure 34: Fracture surface of baseline sample. (A) Backscatter overview micrograph showing regions of interest. (B) BSED micrograph of hole wall showing multiple crack initiation sites. (C) Highlighted region from B showing particles present at crack initiation sites. (D) BSED micrograph of drack growth region showing fatigue crack growth marks. (E) Intermetallic particle within crack growth region. (F) Iron Kα1 spectra of E. (G) Copper Kα1 spectra of E.

A backscatter micrograph of a repaired fracture surface is shown in Manuscript 3. Figure 35A. 2 regions of interest were identified, a crack initiation site is outlined in white, and a region of crack growth is outlined in black. The crack initiation site is shown in Manuscript 3. Figure 35B and is further magnified in Manuscript 3. Figure 35C. The crack initiation site of the repaired sample appears to have an intergranular nature with few large constituent particles. The size of the constituent particles on the repaired fracture face appears to be greatly reduced in size compared to baseline samples. This is further exemplified in Manuscript 3. Figure 35D where the constituent particles are approximately 5-10 µm in diameter. There is an apparent difference in the fracture surface between Manuscript 3. Figure 34D and Manuscript 3. Figure 35D, in the crack growth region on the repaired surface the fracture type is mostly intergranular.

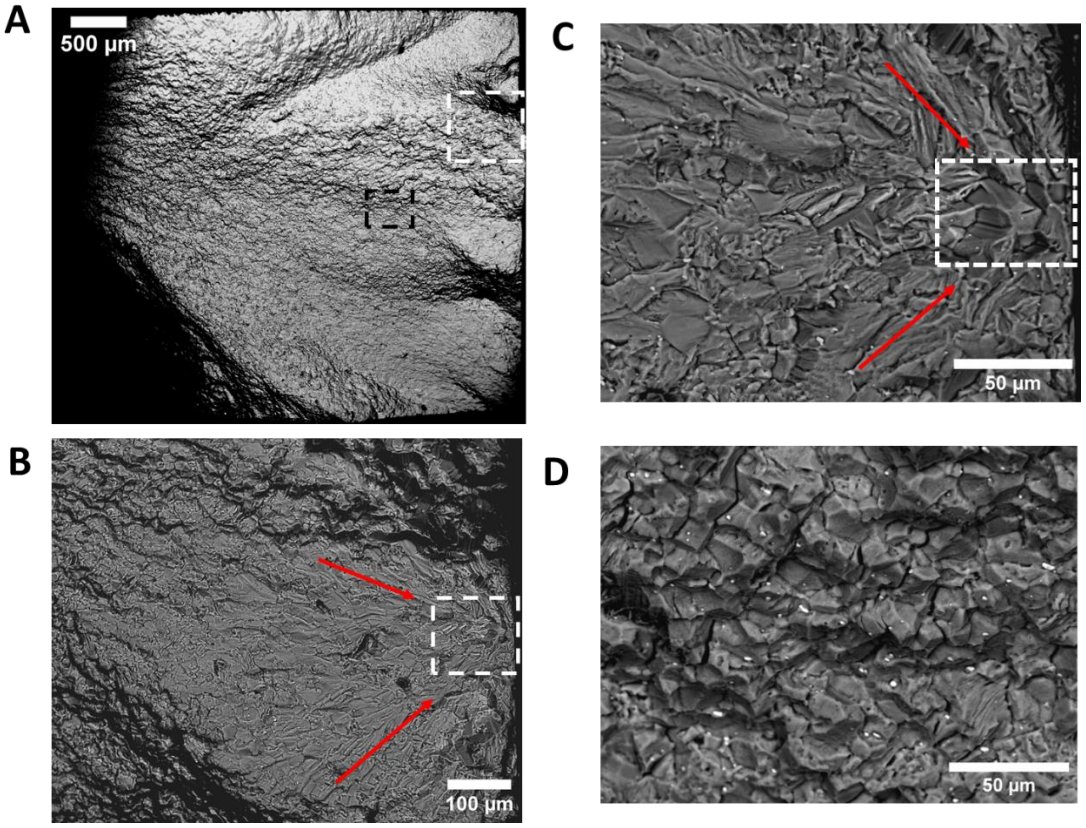

Manuscript 3. Figure 35: Fracture surface of repaired specimen. (A) BSED micrograph overview with regions of interest highlighted. (B) Higher magnification BSED micrograph of crack initiation site of A showing crack growth direction and region of interest. (C) BSED micrograph of crack initiation site showing evidence of intergranular region. (D) BSED micrograph of crack growth region highlighted in A.

Fatigue Frame Analysis

To analyze the fatigue displacement data, it was first fit with a cubic spline. After fitting the spline was used to interpolate additional data points to better resolve the peaks of the sinusoid using the Python library Scipy [21]. The peaks of the smoothed displacement data were found using the wavelet transform algorithms described in Zhang et. al. [22] and then vertically shifted

to make the minimum value equal to zero to allow for comparison between all datasets. The shifted displacement peak data were then fit with a RANSAC linear fit from the Scikit-learn library, which allows for fitting the linear region of the fatigue data robustly without the data from after crack growth affecting the fit [23], [24]. The start of exponential crack growth was designated as the abscissa where the RANSAC fit and the displacement data deviated by 0.002 mm in the ordinate; this deviation value was arbitrarily chosen but was held constant between all fatigue datasets.

The displacement vs. cycle values discussed above were plotted to understand the different regions of the load-controlled fatigue tests. The resulting plots are shown in Manuscript 3. Figure 36, in each plot the best, worst, and 50% fatigue life are plotted. Manuscript 3. Figure 36A-C show the R=-1 loading condition for the 1/4" Hole Repair, 5/16" Baseline, and 1/4" Baseline respectively. Similarly, Manuscript 3. Figure 36D-F shows the R=0.1 loading condition for the 1/4" Hole Repair, 5/16" Baseline, and 1/4" Baseline. Most of the displacement curves show a similar series of trends; first a cyclic softening region that peaks into a cyclic hardening regime, this is followed by a steady state regime, then exponential crack growth and final failure. For the R=-1 loading case, the worst performing 1/4" Hole Repair and 5/16" Baseline both show a lack of cyclic softening behavior and enter directly into the steady state region. While both samples failed earlier than their counterparts, the reason behind the lack of cyclic softening is not understood. Outside of these anomalies, the overall behavior of all the fatigue samples appears to be quite similar.

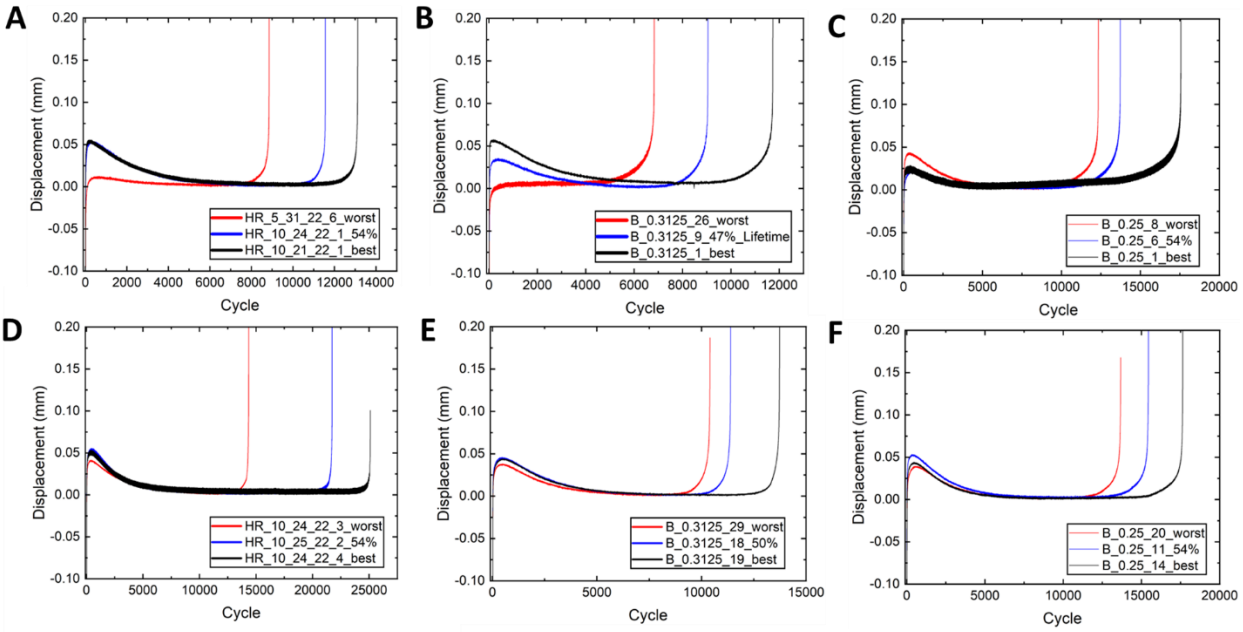

Manuscript 3. Figure 36: Cycle-Displacement curves for best, middle, and worst performing fatigue specimen. (A) 1/4" Repair in R=-1 loading. (B) 5/16" Baseline in R=-1 loading. (C) 1/4" Baseline in R=-1 loading. (D) 1/4" Repair in R=0.1 loading. (E) 5/16" Baseline in R=0.1 loading. (F) 1/4" Baseline in R=0.1 loading.

Utilizing the start of the exponential crack growth discussed previously, further trends can be understood about the effect of the repair on fatigue life. Manuscript 3. Table 4 shows the

average pre-crack lifetime for the different coupon configurations and loading conditions. The R=-1 loading condition has a lower pre-crack lifetime compared to the R=0.1 loading condition, meaning the higher stress in the R=0.1 loading increased the crack growth rate. The largest difference within a single loading condition is between the baseline material and the repaired material. For the R=-1 loading case the baseline material spent approximately 84% of the total fatigue life before the 0.002 mm displacement threshold was met. The repaired samples spent 90.6% of their life in this state. This trend holds in the R=0.1 loading condition where the baseline material spent 91.5% and 90.5% for the 5/16" and 1/4" Baselines respectively, but the 1/4" Repair spends 96.4% of its lifetime in the pre-crack state. This data points to the repaired material delaying the onset of exponential crack growth.

Manuscript 3. Table 4: Average pre-crack lifetime

	R=-1 Average Pre-Crack Lifetime	R=0.1 Average Pre-Crack Lifetime
5/16" Baseline	84%	91.5%
1/4" Baseline	84.6%	90.5%
1/4" Repair	90.6%	96.4%

By counting the number of cycles after the crack initiation threshold, some trends can be inferred about the fatigue crack growth rate of the different configurations. As expected, the R=0.1 loading condition had fewer cycles to failure after crack initiation; this is due to the higher loading stress and increased crack growth rate before gross overload failure. For both loading conditions, the 1/4" Repair had fewer cycles to failure after crack initiation than the 5/16" and 1/4" Baseline configurations. This further exemplifies that the repair process is prolonging the crack initiation phase of the fatigue life, but it appears that the repair is detrimental to the crack growth rate phase.

Manuscript 3. Table 5: Average cycles to failure after crack initiation

	R=-1 Average Cycles to Failure after Crack	Standard Deviation	R=0.1 Average Cycles to Failure after Crack	Standard Deviation
5/16" Baseline	1,452	182	983	103
1/4" Baseline	2,126	175	1,475	181
1/4" Repair	1,031	410	687	192

Discussion

Viability of Repair

It should be noted some of the short comings of this work. This work is not wide reaching in its viability for repairs of different geometries. The repair strategy used to produce these results is not all inclusive and there is room for further improvement. In the technology's current capacity, it has been proven that AFSD is a viable means for repairing legacy components of AA7050 back to geometrical tolerances while simultaneously increasing the fatigue life of a simplified component. Changing the geometry of the repaired feature via changing hole diameter or hole depth without changing repair strategy may not provide the same simultaneous geometrical and structural repair. The depth of hole that may be successfully repaired by this process may be limited by the depth of mixing that can be generated, it is paramount to produce

mixing between the existing hole wall and the deposited material. The diameter of the hole that may be repaired will most likely be determined by the feed material cross section; if the hole diameter is larger than the cross section of the feed material there may not be adequate force to promote shear.

The general nature of fatigue must be understood as well, great care must be taken in specimen preparation and consistency. Despite these efforts, fatigue has inherent variability in its results. To conduct a study and attempt to relay results to true fatigue performance multiple specimens must be created and tested.

Effect of Microstructure

The microstructure of the repaired material provides a unique insight into the different thermo-mechanical regimes experienced during an AFSD print. In a typical deposition scenario, the deposited material has a more homogeneous microstructure as it has experienced similar shear events. The different regions of a repaired geometry are vastly different, there are key differences between regions that are fully recrystallized as opposed to partially recrystallized; furthermore, there are differences between regions that have experienced the high shear event of a pin interaction as well.

Of the different regions of the repair discussed, the thermo-mechanical affected zone is distinctly different, it shows the least recrystallized microstructure and consequentially shows the lowest amount of heterogeneous precipitation on the Al_3Zr dispersoid particles. It has been widely reported that a recrystallization event in the AA7050 microstructure creates an incoherent interface and provides a heterogeneous nucleation site [1], [2], [25], [26]. This phenomenon is creating a region within the TMAZ where the η precipitates of the AA7050-T7451 starting microstructure are dissolving then naturally aging out in the matrix after printing. This is creating a dense microstructure of small coherent particles which are providing strength to the material.

All other regions of the repair are fully recrystallized, leading to a large degree of heterogeneous precipitation during the relatively slow cooling period after printing. This slow cooling is giving adequate time for solute to segregate to the incoherent interfaces of the Al_3Zr particles. This heterogeneity is creating large PFZs throughout the matrix, both around the dispersoid particles and around the grain boundaries. These PFZs allow for regions of strain localization and may provide a site for crack initiation and growth.

The high shear strain nature of AFSD that caused recrystallization of the AA7050 matrix also played a large role in modifying the constituent particles. Comparing the constituent particle size in Manuscript 3. Figure 34 and 12 shows a stark difference. Manuscript 3. Figure 34 shows clusters of constituent particles around 15-20 µm, whereas Manuscript 3. Figure 35 shows particles that are more spherical on the order of 5 µm. This particle breakup is attributed to the high shear nature of the process and has been shown to occur in other material systems [27].

The thermal effects of the AFSD process are pronounced on the microstructure, the high heat experienced during printing fully dissolves the starting precipitates. After cooling from

printing the precipitates are naturally aged out before testing. This leads to a logical step forward to advance this process, the ability to actively cool the substrate material after printing to reduce the amount of heterogeneous nucleation and reduce the width of PFZs. In a synergistic effect, this increased cooling will also leave more solute in solution for precipitating into η that can further improve strength.

Mechanisms of Fatigue

Crack Initiation

The influence of the deposition process is readily apparent when investigating the fracture surfaces of the broken fatigue coupons. In the baseline material, the crack initiation is clearly the Fe and Cu rich constituent particles. These large particles are bonded weakly with the matrix and provide a region for strain localization and eventual crack initiation. The dispersion and size of these constituent particles will directly influence the time to crack initiation, a specimen with a larger distribution along the hole wall will undergo crack initiation in fewer cycles.

The deposited material is distinctly different, the constituent particles are still clear on the fracture surface; but they are not the site of crack initiation. Investigating crack initiation such as Figure 12c, the initiation appears to coincide with a region of intergranular fracture. This is most likely a region of heavy grain boundary precipitation that occurred during the slow cooling. The AFSD repair process has changed the mechanism of crack initiation from constituent particles to regions of heterogeneous precipitation and corresponding PFZs. This result agrees with the trends observed during fatigue testing and displayed in Manuscript 3. Table 4, the average pre-crack lifetime is greater for the repaired material compared to the baseline. The AFSD repair process is pushing off crack initiation.

Crack Growth

There are significant differences in the mechanism of crack growth between the baseline material and the repaired samples. In the baseline material, there is clear evidence of typical fatigue striations on the fracture surface with regions of advanced propagation around the constituent particles. This fatigue striation is typical of a ductile material undergoing fatigue crack growth. In the repaired material, the fracture surface has more intergranular features. This is typically a sign of embrittlement; in this case the fatigue crack is preferentially travelling along the grain boundaries due to the near continuous grain boundary precipitates and corresponding large PFZs. The transition from a more typical fracture mode to the intergranular fracture is shown in Figure 12b, the small region around crack initiation fractures similarly to baseline material, but as the crack grows the fracture mode changes. This change in crack growth mechanism is detrimental to the fatigue crack growth rate of the repaired coupon, as shown in Manuscript 3. Table 5. The number of cycles from crack observation to final gross overload failure is reduced for the repaired material. In a real-world repair scenario, this would affect the service and inspection timeline for a component after a repair; in order to catch a crack before it becomes a catastrophic flaw the time period between inspections would be shortened.

Gross Overload failure

The lack of recrystallization in the TMAZ is allowing for a similar effect in the final gross overload failure of the sample during testing between all test configurations. In the baseline material, the overgrown η precipitates of the overaged AA7050-T7451 condition are providing significant strength in the region undergoing gross overload failure. In the repaired material, the TMAZ is playing a similar role, the retention of the rolled microstructure and coherency of the dispersoid particles is allowing for significant precipitation after the repair process in the form of natural aging. These small precipitates shown in Figure 10d and e are providing significant strength to the matrix.

Wide Reaching Implications

This work is wide reaching in its implications, to this point the authors are not aware of a technique that can both geometrically and structurally repair a vertical hole wall above its damaged configuration. This work was conducted on AA7050, the alloy comprising a vast majority of structural components on aircraft. This work also addresses a rampant issue in the aerospace industry i.e., corroded holes on legacy components in service. With the decline of manufacturing and inability to source components, the lead times and exorbitant costs of components can impede fleet readiness. For large components in service this repair process may provide a cost-effective method for keeping incredibly costly components in service and increasing the parts effective lifetime.

Conclusions and Future Work

Additive Friction Stir Deposition was successful in geometrically and structurally repairing simulated corroded fastener holes in AA7050. The microstructure and mechanical performance of the repaired material is distinctly different from the base material. The following points highlight the results.

- The repaired 1/4” hole geometry outperformed the 5/16” Baseline configuration for both R=-1 and R=0.1 loading conditions.
- The repaired 1/4” hole geometry outperformed the 1/4” Baseline configuration for the R=0.1 loading condition.
- The repair applied sufficient heat to fully solutionize the precipitates of the deposited and substrate material in the region directly surrounding the hole. Reprecipitation during cooling from high temperatures as well as natural aging after printing created a bimodal size distribution of η-phase precipitates.
- Regions that underwent recrystallization during the printing had significant heterogeneous precipitation on the Al_3Zr dispersoid particles; this is believed to be due to the loss of coherency between the particle and the matrix after a recrystallization event.
- The high shear of AFSD broke apart the Fe-rich constituent particles that were the causes of crack initiation in the baseline material; effectively pushing off crack initiation for the repaired samples.
- The heterogeneous precipitation in the recrystallized region created large PFZs that accelerated crack propagation in the repaired material.
- This result highlights the viability of AFSD for repairing legacy aircraft components.

While this work was successful in improving the fatigue life on the component level there may be unforeseen challenges when implementing on large scale components. The most prominent issue will be thermal degradation of the surrounding material; future work should focus on improving the capability to actively cool the repaired material and adjacent regions.

Manuscript 3 References

[1] E. A. Starke and J. T. Staley, "Application of modern aluminium alloys to aircraft," in *Fundamentals of Aluminium Metallurgy: Production, Processing and Applications*, Elsevier Ltd., 2010, pp. 747–783. doi: 10.1533/9780857090256.3.747.

[2] B. L. Ou, J. G. Yang, and M. Y. Wei, "Effect of homogenization and aging treatment on mechanical properties and stress-corrosion cracking of 7050 alloys," *Metall Mater Trans A Phys Metall Mater Sci*, vol. 38, no. 8, pp. 1760–1773, Aug. 2007, doi: 10.1007/s11661-007-9200-z.

[3] Grand View Research, "Aerospace Forging Market Size, Share & Trends Analysis Report By Material (Aluminum, Titanium, Steel), By Aircraft (Commercial, Military), By Region, and Segment Forecasts, 2020-2027." Accessed: Oct. 24, 2023. [Online]. Available: https://www.grandviewresearch.com/industry-analysis/aerospace-forging-market

[4] U.S. Department of Commerce, "National Security Assessment of the U.S. Forging Industry," 1992.

[5] "Naval Aviation Enterprise Corrosion Prevention Team Army Corrosion Summit," 2009.

[6] H. Z. Yu, "Process fundamentals," in *Additive Friction Stir Deposition*, Elsevier, 2022, pp. 21–75. doi: 10.1016/B978-0-12-824374-9.00002-2.

[7] H. Z. Yu *et al.*, "Non-beam-based metal additive manufacturing enabled by additive friction stir deposition," *Scr Mater*, vol. 153, pp. 122–130, Aug. 2018, doi: 10.1016/j.scriptamat.2018.03.025.

[8] T. Qi, H. Zhu, H. Zhang, J. Yin, L. Ke, and X. Zeng, "Selective laser melting of Al7050 powder: Melting mode transition and comparison of the characteristics between the keyhole and conduction mode," *Mater Des*, vol. 135, pp. 257–266, Dec. 2017, doi: 10.1016/j.matdes.2017.09.014.

[9] N. T. Aboulkhair, M. Simonelli, L. Parry, I. Ashcroft, C. Tuck, and R. Hague, "3D printing of Aluminium alloys: Additive Manufacturing of Aluminium alloys using selective laser melting," *Progress in Materials Science*, vol. 106. Elsevier Ltd, Dec. 01, 2019. doi: 10.1016/j.pmatsci.2019.100578.

[10] J. H. Martin, B. D. Yahata, J. M. Hundley, J. A. Mayer, T. A. Schaedler, and T. M. Pollock, "3D printing of high-strength aluminium alloys," *Nature*, vol. 549, no. 7672, pp. 365–369, Sep. 2017, doi: 10.1038/nature23894.

[11] R. S. Mishra and M. Komarasamy, *Physical Metallurgy of 7XXX Alloys*. Elsevier, 2016. doi: 10.1016/b978-0-12-809465-5.00002-7.

[12] R. Joey Griffiths, D. T. Petersen, D. Garcia, and H. Z. Yu, “Additive friction stir-enabled solid-state additive manufacturing for the repair of 7075 aluminum alloy,” *Applied Sciences (Switzerland)*, vol. 9, no. 17, Sep. 2019, doi: 10.3390/app9173486.

[13] J. K. Yoder, “Origins of Embrittlement of an Al-Zn-Mg-Cu Alloy Post Additive Friction Stir Deposition,” Virginia Tech, Blacksburg, 2022.

[14] J. K. Yoder, R. J. Griffiths, and H. Z. Yu, “Deformation-based additive manufacturing of 7075 aluminum with wrought-like mechanical properties,” *Mater Des*, vol. 198, Jan. 2021, doi: 10.1016/j.matdes.2020.109288.

[15] G. G. Stubblefield *et al.*, “Ballistic Evaluation of Aluminum Alloy (AA) 7075 Plate Repaired by Additive Friction Stir Deposition Using AA7075 Feedstock,” *Journal of Dynamic Behavior of Materials*, vol. 9, no. 1, pp. 79–89, Mar. 2023, doi: 10.1007/s40870-022-00363-6.

[16] D. Z. Avery *et al.*, “Evaluation of Microstructure and Mechanical Properties of Al-Zn-Mg-Cu Alloy Repaired via Additive Friction Stir Deposition,” *J Eng Mater Technol*, vol. 144, no. 3, Jul. 2022, doi: 10.1115/1.4052816.

[17] J. Q. Su, T. W. Nelson, R. Mishra, and M. Mahoney, “Microstructural investigation of friction stir welded 7050-T651 aluminium,” *Acta Mater*, vol. 51, no. 3, pp. 713–729, Feb. 2003, doi: 10.1016/S1359-6454(02)00449-4.

[18] K. A. A. Hassan, A. F. Norman, D. A. Price, and P. B. Prangnell, “Stability of nugget zone grain structures in high strength Al-alloy friction stir welds during solution treatment,” *Acta Mater*, vol. 51, no. 7, pp. 1923–1936, Apr. 2003, doi: 10.1016/S1359-6454(02)00598-0.

[19] M. B. Lezaack and A. Simar, “Avoiding abnormal grain growth in thick 7XXX aluminium alloy friction stir welds during T6 post heat treatments,” *Materials Science and Engineering A*, vol. 807, Mar. 2021, doi: 10.1016/j.msea.2021.140901.

[20] I. Charit and R. S. Mishra, “Abnormal grain growth in friction stir processed alloys,” *Scr Mater*, vol. 58, no. 5, pp. 367–371, Mar. 2008, doi: 10.1016/j.scriptamat.2007.09.052.

[21] P. Virtanen *et al.*, “SciPy 1.0: fundamental algorithms for scientific computing in Python,” *Nat Methods*, vol. 17, no. 3, pp. 261–272, 2020, doi: 10.1038/s41592-019-0686-2.

[22] Z.-M. Zhang *et al.*, “Multiscale peak detection in wavelet space,” *Analyst*, vol. 140, no. 23, pp. 7955–7964, 2015, doi: 10.1039/C5AN01816A.

[23] M. A. Fischler and R. C. Bolles, “Random Sample Consensus: A Paradigm for Model Fitting with Applications to Image Analysis and Automated Cartography,” *Commun. ACM*, vol. 24, no. 6, pp. 381–395, Jun. 1981, doi: 10.1145/358669.358692.

[24] F. Pedregosa *et al.*, “Scikit-learn: Machine Learning in Python,” *Journal of Machine Learning Research*, vol. 12, no. 85, pp. 2825–2830, 2011, [Online]. Available: http://jmlr.org/papers/v12/pedregosa11a.html

[25] Y. Sun, X. Bai, D. Klenosky, K. Trumble, and D. Johnson, “A Study on Peripheral Grain Structure Evolution of an AA7050 Aluminum Alloy with a Laboratory-Scale Extrusion Setup,” *J Mater Eng Perform*, vol. 28, no. 8, pp. 5156–5164, Aug. 2019, doi: 10.1007/s11665-019-04208-7.

[26] M. Schöbel, P. Pongratz, and H. P. Degischer, “Coherency loss of Al 3(Sc,Zr) precipitates by deformation of an Al-Zn-Mg alloy,” *Acta Mater*, vol. 60, no. 10, pp. 4247–4254, Jun. 2012, doi: 10.1016/j.actamat.2012.04.011.

[27] J. K. Yoder, G. D. Hahn, N. Zhao, R. E. Brennan, K. Cho, and H. Z. Yu, “Additive friction stir deposition-enabled upcycling of automotive cast aluminum chips,” *Additive Manufacturing Letters*, vol. 4, p. 100108, Feb. 2023, doi: 10.1016/j.addlet.2022.100108.

Manuscript 3. Appendix A
Substrate Technical Drawing

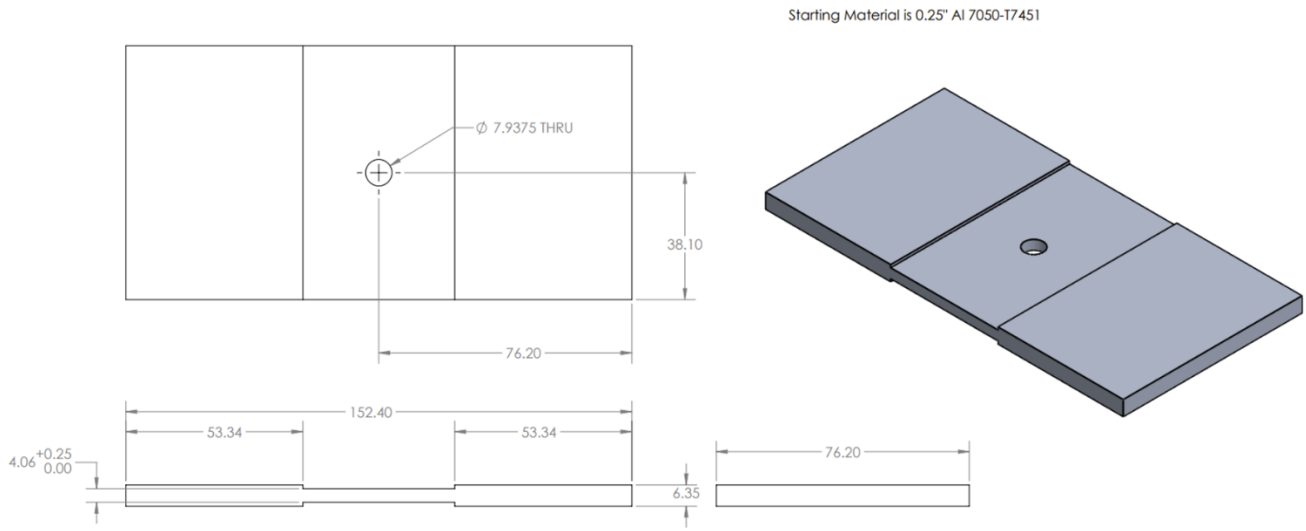

Manuscript 3. Appendix B
Test Coupon Technical Drawing

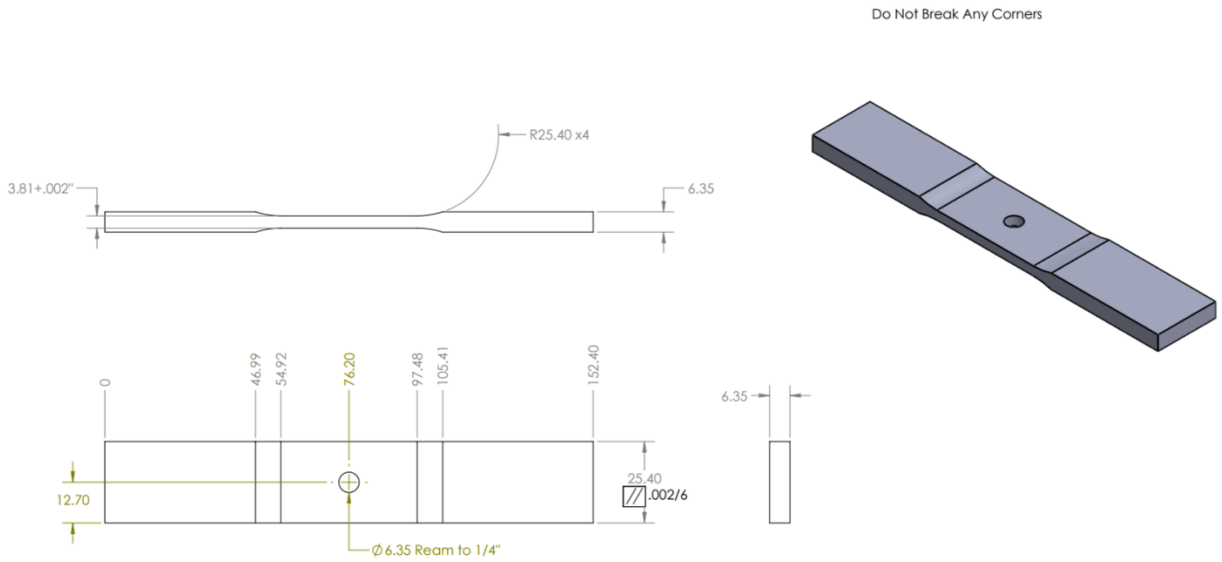

Chapter 5: Conclusions and Future Work

5.1 Post-Deposition Heat Treatment of AA7050

Chapter two presents a manuscript demonstrating the viability of heat-treating AA7050 back to full forging strength after deposition via AFSD. Within the scope of additive manufacturing and specifically AFSD, this was the first reported result showing the capability for any 3D printing process. More encouraging, AFSD was able to achieve these results without altering the alloy chemistry. For many conventional AM processes, the ability to deposit fully dense AA7050 is a challenge. This manuscript shows that to process alloys that require wrought processing, a solid-state deformation additive manufacturing technique must be utilized.

It was previously shown that precipitation hardened aluminums deposited via AFSD necessitate post-deposition heat treatment to have considerable strength and that was again demonstrated in this work. The as-deposited material has insufficient yield and ultimate tensile strength for use in a component; furthermore, the hardness trends show variability along the height of the build meaning that the thermal exposures of subsequent layers are modifying the precipitate structure. This variability through the height further exemplifies the need to conduct post deposition solutionizing and aging. During the initial experimentation discussed in Manuscript 1, it was discovered that the deposited material underwent abnormal grain growth in the post deposition solutionizing treatment. AA7050 is an alloy that is known to undergo a secondary recrystallization event after high strain processes, typically this is attributed to the high strain rate causing an unstable grain structure.

Comparing the deposited AA7050 that was subjected to T74 treatment and AA7050 from rolled plate subjected to the same heat treatment the tensile responses were nearly identical. This was due to adequate water quenching of the coupons and their limited thickness (2 mm). In industrial cases, AA7050 is not used in such thin component sections, instead AA7075 is used. The real use case of AA7050 is thicker sections where quenching in cold water can induce quench cracking. AA7050 can be quenched more slowly because it utilizes the $L1_2$-structure Al_3Zr dispersoid particle. This particle forms in a solid-solid reaction with minimal lattice mismatch to the aluminum matrix, lending fully coherent interfaces. Typical processing of AA7050 is centered around maintaining the integrity of the coherent interfaces to reduce sites for heterogeneous precipitation in quenching. Manuscript 2, within Chapter 3, focuses on the quench sensitivity of AA7050 after processing with AFSD. AFSD is a severe plastic deformation process, it relies on the ability for the material to create and annihilate dislocations rapidly to undergo plastic flow. One of the most accessible regions for dislocation annihilation is grain boundaries, and in the case of aluminum undergoing AFSD leads to a phenomenon referred to as continuous dynamic recrystallization. During this recrystallization event, the prior grains of the feed material are continuously rotated until they reach a small enough size to accommodate all the dislocations necessary to facilitate plastic flow. This style of processing is not conventional for the AA7050 alloy system, and a fundamental study was conducted to understand the effect of severe plastic flow.

5.2 Quench Sensitivity

Manuscript 3 shows the effects of zirconium on the quench sensitivity of AA7050 after AFSD. This was demonstrated by casting an AA7050 alloy without Zr, processing with AFSD and exaggerating the slow cooling rates experienced in thick components. This modified AA7050 alloy was printed with identical processing parameters to conventional AA7050, using both a featureless and protrusion tool. Tensile coupons were retrieved from the deposits and subjected to identical thermal treatments except for a distinction after solutionizing AC, referring to air cool; and WQ, referring to a water quench. The exaggerated slow cooling rate in the air cool sample allows for heterogeneous precipitation to take place. This metric was quantified by using the yield strength of resulting tensile tests, the water quench was used as a control of adequate cooling and the air cool showed the specimens quench sensitivity. It was found that for as-received rolled plate AA7050, a modest drop in yield strength was experienced between the water quenched and air cooled. In the case of conventional AA7050 processed with a featureless tool, the yield strength drops off between the water quenched and air-cooled specimens were drastic. Comparing identically processed AA7050 without Zr, there was a minimal yield strength drop between the water quenched and air-cooled samples empirically pointing to the Al_3Zr dispersoid particles as the culprit for the increased quench sensitivity. This was later observed in STEM to be true, the dynamic recrystallization process causes the dispersoid particles to act as heterogeneous nucleation sites. The same style of experiments was conducted using a tool with tear drop shaped protrusions on the face, in other work these protrusions have been shown to dramatically increase total strain. Using the protrusion tool, the conventional AA7050 and Zr-free AA7050 show similar responses in yield strength drop. The conventional AA7050 processed with the protrusion tool had the same quench sensitivity experienced by the featureless tool due to the loss of coherency of the Al_3Zr dispersoid, while the Zr-free AA7050 showed signs

of extensive heterogenous precipitation occurring on Fe-rich and Si-rich constituent particles. The high shear process of AFSD broke the constituent particles up considerably between the featureless and protrusion tools essentially increasing the number fraction of heterogeneous precipitation sites between the two processing conditions.

5.3 Particle Coherency

The loss of coherency of the $L1_2$ dispersoid particle is a well-documented phenomenon in the high-strength aluminum alloys. Conventional processing of thick components has been optimized to lower flow stress and reduce the amount of recrystallization that occurs. The solid-solid reaction that lends itself to providing coherent interfaces, as opposed to liquid-solid formations that typically create incoherent interfaces, also means that it is difficult if not impossible to regain coherency of the interface. The Al_3Zr particles do not reorient themselves within a matrix, instead the matrix would have to reorient itself to accommodate the particle coherently. The loss of the particle coherency would provide the detrimental effects discussed throughout the entirety of this work. The incoherent interfaces provide heterogeneous nucleation sites for the strengthening η-phase precipitates, lowering the strength of the alloy especially in thicker sections. The loss of interface coherency is also detrimental to the intended role of the dispersoid particles, stabilizing the grain structure. The loss of coherency lowers the Zener pinning pressure exerted by the dispersoid by a factor of two. This may lead to unstable microstructures more likely to undergo a secondary recrystallization event. The severe plastic deformation nature of AFSD does not allow for deposition without a dynamic recrystallization event, there is no way to avoid dispersoid particles becoming incoherent during processing via AFSD.

5.4 Solutions to Quench Sensitivity

In this work, a solution to the increased quench sensitivity is proposed and discussed. By removing the minor alloying element of Zr, the formation of the dispersoid particle can be avoided altogether. This was shown to be highly effective when utilizing a featureless tool. The yield strength drop between the air cooled and water quenched samples was nearly negligible. This is exciting for the viability of AFSD, alloys may need to be modified to undergo processing with acceptable performance. The removal of Zr was not without pitfalls. The removal of the primary grain stabilizing agent allows for significant grain growth during post deposition thermal treatments. While this may be unacceptable for some applications where excessively large grains may provide preferential sites for intergranular corrosion, there may be applications where corrosion inhibiting surface coatings can be sufficient for use. Most of the grain growth is expected to occur during the solutionizing treatment, grain boundary mobility follows and Arrhenius equation with temperature, and typical service temperatures for 7xxx series alloys fall below 100 °C.

5.5 Viability of AFSD for Creating AA7050 Components

This work shows that AFSD is viable for creating components in AA7050 that are sufficiently thin. Creating thin components can avoid the detrimental effects of the increased quench sensitivity introduced by AFSD by increasing the effective quench rate. As mentioned in Manuscript 2, the typical use case of AA7050 is not thin components, this alloy is used for thick

structural components. For this application AFSD will not be viable. To overcome the thicker component section, faster quench rates would need to be introduced which would cause severe quench cracking from the imparted thermal stress. This limitation has wide reaching implications, most modern high strength aluminum alloys leverage the use of Zr or Sc dispersoid particles. It is expected that the Al_3Sc dispersoid particle (which shares the same $L1_2$ structure) will experience the same loss of coherency. The intended application of AFSD (replacing complex aerostructure forgings) may not be feasible. Removing the dispersoid particles would change the alloy chemistry which would be unacceptable for some designs and require significant testing and material qualification.

5.6 Structural Repair

Chapter 3 demonstrates the success of an application driven repair in AA7050 for corroded fastener holes. It was demonstrated that the significant shear event of AFSD broke up and dispersed fatigue crack initiating Fe-rich constituent particles and drove off fatigue crack initiation. This performance enhancing mechanism counteracted the loss of dispersoid coherency and overgrown precipitates that created a weaker matrix. As shown in Chapter 1 and 2, the ability to repair a full-scale component and successfully heat treat it would not be feasible, but with thermal solutions, an in-situ repair without further thermal treatment may be viable. The complex thermal fields surrounding the repair region are not well understood, but based purely upon the metric of fatigue life it appears that an AFSD enabled repair may be viable in certain applications.

5.7 Future Work

Further experiments and advancements need to be undertaken to understand the further effects of removing Zr from the high-strength aluminum alloys. Certain component level designs may allow for the larger grain size of the Zr-free material and possible impact on properties. Further studies need to be conducted to understand the extent of the increased quench sensitivity, if alloy modifications are not feasible, a maximum thickness for AFSD components must be determined based on the quench rate that would induce heterogeneous precipitation. There is a large demand for the ability to create large scale forging replacement parts via AFSD, further alloy design may allow this to be feasible.

Future alloy design for AFSD should be focused on temperature stable precipitates. The pitfalls of AFSD and AA7050 are due to having both thermally stable and soluble precipitates present in the same alloy. The thermally stable precipitates meant to stabilize the grain structure will always provide a site for heterogeneous nucleation during the quenching process that is necessitated by the thermally soluble precipitates. If an alloy is developed that leverages the ability of AFSD to break down thermally stable precipitates and introduce a large enough volume fraction with a small enough radius, there may be large strengths that can be achieved. A representative alloy system of interest is the Al-Ce system, the cerium has almost zero solubility in the solid aluminum, meaning that it forms intermetallics almost immediately during cooling. After AFSD, these particles may be broken into small enough sizes to provide adequate strength for the aluminum in the as-printed condition. The repeated thermal exposures of subsequent layers may not alter the precipitates.